

**FEDERAL UNIVERSITY OF SANTA MARIA
TECHNOLOGY CENTER
GRADUATE PROGRAM
IN ELECTRICAL ENGINEERING**

Filipe Pinarello Scalcon

**PERFORMANCE IMPROVEMENT OF SWITCHED
RELUCTANCE MOTORS THROUGH ADVANCED
CONTROL STRATEGIES**

**Santa Maria, RS, Brazil
2021**

Filipe Pinarello Scalcon

**PERFORMANCE IMPROVEMENT OF SWITCHED RELUCTANCE
MOTORS THROUGH ADVANCED CONTROL STRATEGIES**

Thesis presented to the Doctorate Course of the Graduate Program in Electrical Engineering, in the Electrical Energy Processing research area, of the Federal University of Santa Maria (UFSM-RS), as a partial requirement to obtain the degree of **Doctor in Electrical Engineering**.

Supervisor: Prof. D.Sc. Hilton Abílio Gründling
Co-supervisor: Prof. Dr. Rodrigo Padilha Vieira

Santa Maria, RS, Brazil
2021

This study was financed in part by the Coordenação de Aperfeiçoamento de Pessoal de Nível Superior - Brasil (CAPES) - Finance Code 001

Ficha catalográfica elaborada através do Programa de Geração Automática da Biblioteca Central da UFSM, com os dados fornecidos pelo(a) autor(a).

Scalcon, Filipe Pinarello

Performance Improvement of Switched Reluctance Motors
Through Advanced Control Strategies / Filipe Pinarello Scalcon
- 2021

164 p.; 30 cm

Orientador: Hilton Abílio Gründling

Coorientador: Rodrigo Padilha Vieira

Tese (doutorado) – Universidade Federal de Santa Maria,
Technology Center, Programa de Pós-Graduação em
Electrical Engineering, RS, 2021

1. Electrical engineering 2. Switched reluctance motor 3.
Firing angle optimization 4. Super-twisting sliding mode control
5. Robust Control I. Gründling, Hilton Abílio. II. Vieira,
Rodrigo Padilha.

© 2021

All copyrights reserved to Filipe Pinarello Scalcon. The reproduction of parts or all of this work can only be done with a written permission of the author.

Address: 1000 Roraima Ave, Camobi, Santa Maria, RS, Brasil, Zip Code: 97105-900;

Cell phone number: +55 (55) 9-9920-3033;

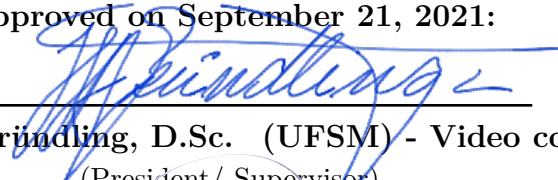
E-mail: filipescalcon1@gmail.com

Filipe Pinarello Scalcon

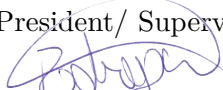
**PERFORMANCE IMPROVEMENT OF SWITCHED RELUCTANCE
MOTORS THROUGH ADVANCED CONTROL STRATEGIES**

Thesis presented to the Doctorate Course of the Graduate Program in Electrical Engineering, in the Electrical Energy Processing research area, of the Federal University of Santa Maria (UFSM-RS), as a partial requirement to obtain the degree of **Doctor in Electrical Engineering**.


Approved on September 21, 2021:



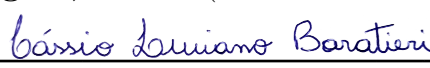
Hilton Abílio Gründling, D.Sc. (UFSM) - Video conference
(President/ Supervisor)



Rodrigo Padilha Vieira, Dr. (UFSM) - Video conference
(Co-supervisor)




Alan Dorneles Callegaro, Ph.D. (McMaster University) - Video conference



Cássio Luciano Baratieri, Dr. (URI) - Video conference



Humberto Pinheiro, Ph.D. (UFSM) - Video conference



Tércio André dos Santos Barros, Dr. (UNICAMP) - Video conference

Santa Maria, RS, Brazil

2021

To those who were close to me throughout the development of this thesis and
who make my achievements their happiness.

ACKNOWLEDGEMENTS

Initially, I would like to thank Professor Hilton Abílio Gründling for his supervision throughout my journey at the Federal University of Santa Maria, from the start of my graduation to the end of my doctorate. Prof. Hilton is an incredible person and an exemplary professional, having always given me the freedom and incentive to research. It has been an amazing opportunity working with you, and I learned a lot from it. Thank you for being such an important part of my personal and professional development.

To Professor Rodrigo Padilha Vieira for his co-supervision, friendship and daily contact. You have also contributed in essential ways to my personal and professional development. Moreover, Professor Rodrigo has been a friend for many of the challenges and events that took place during my doctorate period.

To Professor Vinicius Montagner for linking his studies to the control of electrical machines and collaborating with my scientific development. I also would like to thank the remaining professors of the Power Electronics and Control Research Group, for the knowledge shared throughout my doctorate course.

To Professor Ali Emadi for giving us the opportunity to collaborate with his world-wide respected research group. Prof. Emadi is an amazing and inspiring individual, and it has been a pleasure working with your team. I would also like to thank Gaoliang Fang for his friendship and collaboration. Your help and effort were essential to improve the results presented in this thesis.

To my mother, Vera Lucia Pinarello Scalcon, and my father, Claudio Roberto Scalcon, for their love, encouragement and unconditional support. Thank you also for giving up so many things, always seeking to provide me with a quality education. You have certainly done a good job, and I hope one day I can repay your sacrifices.

To my family, for their love, encouragement and understanding.

To my girlfriend Daniela Maia Bueno, for the love, care and support. Thanks for being such an amazing partner and making the doctorate period a very enjoyable ride. I look forward to sharing the next chapter of life with you.

To all my friends, essential throughout this period, for all the conversations, laughs, parties and barbecues. I'm also grateful for all the shared moments, which in the future will be memories of one of the best phases of my life.

To my colleagues and friends Caio Osório, Gustavo Koch and Thieli Gabbi for the various conversations and discussions, which certainly contributed directly to this thesis. I am also grateful for the collaboration throughout this period, which resulted in important publications. To my other colleagues at Power Electronics and Control Research Group for providing a great work environment.

To my great friends Douglas Pedroso, Leonardo Medeiros and Thiago Lazzari for sharing so many moments inside and outside the university. Thanks for all the daily conversations, advice and moments we shared throughout the years.

To the Federal University of Santa Maria, the Graduate Program in Electrical Engineering, professors and administrative technicians, for the opportunity to access a graduate course of such high quality. To the Power Electronics and Control Research Group for providing a work environment and resources essential to the development of this thesis. To CAPES for the financial support.

To all those who were a part of my life over these past few years, contributing to this work and the completion of this stage of my life, thank you!

“For long you live and high you fly
And smiles you’ll give and tears you’ll cry
And all your touch and all you see
Is all your life will ever be.

Pink Floyd - Breathe”

ABSTRACT

**PERFORMANCE IMPROVEMENT OF
SWITCHED RELUCTANCE MOTORS
THROUGH ADVANCED CONTROL
STRATEGIES**

AUTHOR: FILIPE PINARELLO SCALCON
SUPERVISOR: HILTON ABÍLIO GRÜNDLING
CO-SUPERVISOR: RODRIGO PADILHA VIEIRA

This thesis presents contributions in the field of advanced control strategies for SRMs. These techniques seek to improve the performance of SRMs, specially regarding torque ripple minimization, aiming to mitigate a known drawback of the machine. Firstly, a SRM firing angle optimization procedure based on the particle swarm optimization algorithm is proposed. The procedure is intended for SRMs operating in the current controlled region, below base speed, and seeks a balance between energy efficiency and reduced torque ripple. As a second contribution, a discrete-time super-twisting sliding mode current control scheme for switched reluctance motors is proposed. The proposed method presents enhanced current tracking capabilities, enabling lower torque ripple in SRM drives operating with TSF strategies. The strategy ensures a fixed switching frequency due to PWM implementation and presents a novel gain design procedure, using a cost function. This enables a systematic and straightforward way to determine the controller gains. The procedure is repeated for different speed values, allowing for a variable gain structure, where the controller gains are adjusted online based on the rotor speed. Simulation and experimental results are provided in order to demonstrate the effectiveness of the proposed control schemes.

Keywords: Electrical engineering, switched reluctance motor, firing angle optimization, super-twisting sliding mode control, robust control.

LIST OF FIGURES

Figure 1.1	– Electrical energy consumption in Brazil between the years 2010 and 2019.	27
Figure 1.2	– Electrical energy consumption by type of consumer in Brazil in 2019.	28
Figure 1.3	– Data from PMSM manufacturing. (a) Distribution of weight. (b) Distribution of cost.	29
Figure 1.4	– World mine production of rare-earth-oxide material in 2019.	30
Figure 1.5	– Cross section of a 12/8 switched reluctance machine.	31
Figure 1.6	– Sources of torque ripple in switched reluctance motors.	33
Figure 1.7	– Advanced control strategies for switched reluctance motors.	34
Figure 1.8	– Example block diagram of a TSF strategy.	36
Figure 1.9	– Example phase torque references produced by a cubic TSF.	37
Figure 1.10	– General block diagram for SRM current control.	40
Figure 1.11	– Example block diagram for SRM hysteresis current control.	41
Figure 1.12	– Example block diagram for SRM iterative learning current control. ..	42
Figure 1.13	– Example block diagram for SRM linear current controllers.	43
Figure 1.14	– Example block diagram for SRM dead-beat current controllers.	44
Figure 1.15	– Example block diagram for SRM model predictive current controllers.	46
Figure 1.16	– Example block diagram for SRM adaptive current controllers.	47
Figure 1.17	– Example block diagram for SRM sliding mode current controllers. ..	48
Figure 2.1	– Cross section of a 12/8 SRM, with the coils, rotor and stator high-lighted.	54
Figure 2.2	– Rotor positions of the SRM in relation to phase a. (a) Aligned position. (b) Unaligned position.	55
Figure 2.3	– Theoretical inductance profile for a 12/8 SRM.	56
Figure 2.4	– SRM aligned positions in relation to each phase. (a) Phase a. (b) Phase c. (c) Phase b.	56
Figure 2.5	– Inductance profile of a 12/8 machine with operating regions high-lighted (generator and motor).	57
Figure 2.6	– Sequential phase excitation for motor operation. (a) Phase a. (b) Phase c. (c) Phase b.	58
Figure 2.7	– Three-phase AHB converter.	59
Figure 2.8	– Operational stages of the AHB converter. (a) Magnetization. (b) De-magnetization. (c) Freewheeling.	60
Figure 2.9	– Block diagram for hysteresis current control.	61
Figure 2.10	– Inductance, current and voltage waveforms for hysteresis current control.	62
Figure 2.11	– Block diagram for single pulse control.	63
Figure 2.12	– Inductance, current and voltage waveforms for single pulse control. ..	63
Figure 2.13	– Variation of co-energy with position for a given current value.	66
Figure 2.14	– Characteristics of the 12/8 studied SRM.	69
Figure 2.15	– Characteristics of the 8/6 studied SRM.	69
Figure 2.16	– Block diagram of the Simulink simulation model.	70
Figure 3.1	– Fine grid optimization example.	74
Figure 3.2	– Particle swarm optimization example.	76
Figure 3.3	– Block diagram of the control structure used for the simulations.	77
Figure 3.4	– Flowchart of the fine grid optimization procedure.	78
Figure 3.5	– Simulation results for different values of θ_{on} with $\theta_{off} = 40^\circ$, at a speed of 60 rad/s. (a) Electromagnetic torque. (b) Phase “a” current.	79

LIST OF FIGURES

Figure 3.6	– Simulation results for different values of θ_{off} with $\theta_{on} = 25^\circ$, at a speed of 60 rad/s. (a) Electromagnetic torque. (b) Phase “a” current.	80
Figure 3.7	– Simulation results for a speed of 60 rad/s. (a) Normalized torque ripple. (b) Normalized squared RMS current. (c) Cost function.	80
Figure 3.8	– Simulation results for a speed of 60 rad/s. (a) Electromagnetic torque. (b) Phase “a” current.	81
Figure 3.9	– Flowchart of the particle swarm optimization procedure.	82
Figure 3.10	– Simulation results for a speed of 60 rad/s. (a) Epoch 1. (b) Epoch 10. (c) Epoch 18. (d) Epoch 25.	83
Figure 3.11	– Evolution of cost function value over the epochs.	84
Figure 3.12	– Optimal firing angles as a function of the load torque at a speed of 60 rad/s.	86
Figure 3.13	– Experimental results of electromagnetic torque for different speeds. (a) 20 rad/s. (b) 60 rad/s. (c) 100 rad/s.	87
Figure 3.14	– Experimental results of phase “a” current. Speed of 20 rad/s: (a) Case 1; (b) Case 2; (c) Optimal. Speed of 60 rad/s: (d) Case 1; (e) Case 2; (f) Optimal. Speed of 100 rad/s: (g) Case 1; (h) Case 2; (i) Optimal. CH1: Phase “a” current (1 A/div).	88
Figure 3.15	– Experimental result for variable speed operation. (a) Measured and reference speed. (b) θ_{on} . (c) θ_{off}	89
Figure 3.16	– Experimental result for load step disturbance. (a) Measured and reference speed. (b) θ_{on} . (c) θ_{off} . (d) Phase “a” current before load step. (e) Phase “a” current after load step.	90
Figure 4.1	– Block diagram of the DTSTSM controller.	95
Figure 4.2	– Digital implementation delay in discrete-time control systems using symmetric PWM.	96
Figure 4.3	– Flowchart of the proposed gain design procedure.	102
Figure 4.4	– Simulation results for different gain combinations at 1000 r/min with a 6 Nm load.	103
Figure 4.5	– Cost function values at a speed of 1000 r/min, highlighting the region of the search space containing the optimal gain combination.	104
Figure 4.6	– Simulation results for the optimal gains at a speed of 1000 r/min. (a) Phase current. (b) Cost function.	104
Figure 4.7	– Optimal gains for the proposed DTSTSM controller as a function of speed. (a) k_1 . (b) k_2T_s	105
Figure 4.8	– Block diagram of the current control strategies. (a) DTSTSM controller. (b) Hysteresis controller.	106
Figure 4.9	– PWM characteristics. (a) Current reference example with chopping regions highlighted. (b) Soft chopping waveforms. (c) Hard chopping waveforms.	107
Figure 4.10	– Experimental results for a speed of 500 r/min and a 3 Nm load. (a) DTSTSM controller ($f_s = 30$ kHz). (b) Hysteresis controller ($f_s = 57$ kHz).	108
Figure 4.11	– Experimental results for a speed of 500 r/min and a 6 Nm load. (a) DTSTSM controller ($f_s = 30$ kHz). (b) Hysteresis controller ($f_s = 57$ kHz).	109
Figure 4.12	– Experimental results for a speed of 1000 r/min and a 6 Nm load. (a) DTSTSM controller ($f_s = 30$ kHz). (b) Hysteresis controller ($f_s = 57$ kHz).	109
Figure 4.13	– Experimental results for a speed of 2000 r/min and a 6 Nm load. (a) DTSTSM controller ($f_s = 30$ kHz). (b) Hysteresis controller ($f_s = 57$ kHz).	110

Figure 4.14 – Experimental results for a speed of 3000 r/min and a 6 Nm load. (a) DTSTSM controller ($f_s = 30$ kHz). (b) Hysteresis controller ($f_s = 57$ kHz).	110
Figure 4.15 – Experimental results for a dynamic load condition, at a speed of 500 r/min. (a) DTSTSM controller ($f_s = 30$ kHz). (b) Hysteresis controller ($f_s = 57$ kHz).	112
Figure 4.16 – Experimental results for the DTSTSM controller ($f_s = 30$ kHz) in a variable speed condition, under a 3 Nm load. (a) Rotor speed. (b) Torque. (c) Phase current highlight 1. (d) Phase current highlight 2.	113
Figure 4.17 – Experimental results for the Hysteresis controller ($f_s = 57$ kHz) in a variable speed condition, under a 3 Nm load. (a) Rotor speed. (b) Torque. (c) Phase current highlight 1. (d) Phase current highlight 2.	114
Figure A.1 – Block diagram of an SRM drive, highlighting the mechanical system.	143
Figure A.2 – Flowchart of the proposed estimation procedure.	144
Figure A.3 – Block diagram of the current control strategy used for data acquisition.	144
Figure A.4 – Simulation of the SRM with experimental data as inputs.	145
Figure A.5 – Experimental data for a 2.25 A reference. (a) Phase currents. (b) Rotor speed. (c) Phase positions.	146
Figure A.6 – Particle positions through the epochs. (a) Epoch 1. (b) Epoch 5. (c) Epoch 25. (d) Epoch 75.	147
Figure A.7 – Evolution of the best cost function value for each epoch.	148
Figure A.8 – Block diagram of the control strategy used in the experimental results.	149
Figure A.9 – Experimental results for reference speed step variations. (a) Simulation and experimental data comparison. (b) Error between simulation and experimental data.	150
Figure A.10 – Experimental results for reference speed ramp variations. (a) Simulation and experimental data comparison. (b) Error between simulation and experimental data.	150
Figure A.11 – Experimental results for load step variations. (a) Simulation and experimental data comparison. (b) Error between simulation and experimental data.	151
Figure B.1 – Block diagram of the SRM control structure.	154
Figure B.2 – (a) Circular region for pole location, inside the unit circle; (b) Relationship between parameter r and settling time, for the choice $d = 0$	155
Figure B.3 – Analyses for the speed control loop with gains given in (B.8): (a) Closed-loop poles for a sweep in the parameters B and J ; (b) Bode diagrams of the closed-loop system (B.3), from the disturbance input ψ to the output ω_r	158
Figure B.4 – Experimental results to step reference variations with the proposed controller.	158
Figure B.5 – Comparison between simulation responses at the vertices and experimental result for the proposed controller.	159
Figure B.6 – Experimental results to ramp reference variations with the proposed controller.	159
Figure C.1 – SRM drive setup. (a) Block diagram. (b) Picture.	161
Figure C.2 – Mechanical assembly of the switched reluctance and induction machines.	162

LIST OF FIGURES

Figure C.3 – Control cabinet with DSP, measurement hardware and AHB converter. (a) Front side. (b) Back side.	163
Figure C.4 – (a) Diagram of the system used to apply the load disturbance. (b) DC power supply.	163
Figure C.5 – Experimental test bench encompassing the drive, the SRM and an IM, used to provide a mechanical load.	164

LIST OF TABLES

Table 1.1	– Summary and comparison of the SRM TSF strategies.	39
Table 1.2	– Summary and comparison of the SRM current control strategies. ...	49
Table 2.1	– Parameters of the 12/8 studied SRM.	69
Table 2.2	– Parameters of the 8/6 studied SRM.	70
Table 3.1	– Fine grid optimization startup parameters.	79
Table 3.2	– Particle swarm optimization startup parameters.	82
Table 3.3	– Optimization results for the fine grid and particle swarm procedures.	84
Table 3.4	– Experimental results comparison.	87
Table 4.1	– Comparison of the DTSTSM and hysteresis current controllers for a 3 Nm load.	111
Table 4.2	– Comparison of the DTSTSM and hysteresis current controllers for a 6 Nm load.	111
Table 4.3	– Efficiency comparison of the DTSTSM and hysteresis current con- trollers.	115
Table 4.4	– RMS current comparison of the DTSTSM and hysteresis current controllers.	115
Table 4.5	– Comparison of the execution time of the control algorithms.	116
Table A.1	– Particle swarm optimization algorithm parameters.	146
Table A.2	– Results for the three particle swarm optimization executions.	148
Table B.1	– SRM mechanical parameters.	157
Table C.1	– Main components of the experimental setup.	162
Table C.2	– Individual components of the mechanical load.	164
Table C.3	– Main components of the experimental setup.	164

LIST OF ABBREVIATIONS AND ACRONYMS

AHB	Asymmetric half-bridge
ANN	Artificial neural network
CCS	Continuous control set
DTSTSM	Discrete-time super twisting sliding mode
EMF	Electromotive force
FCS	Finite control set
FEA	Finite element analysis
GA	Genetic algorithm
IGBT	Insulated-gate bipolar transistor
ILC	Iterative learning control
IM	Induction motor
LMI	Linear matrix inequality
LUT	Lookup table
MPC	Model predictive control
MPCC	Model predictive current controller
PI	Proportional-integral controller
PMSM	Permanent magnet synchronous motor
PSO	Particle swarm optimization
PWM	Pulse-width modulation
RMS	Root mean square
RMSE	Root mean square error
SOSM	Second order sliding mode
SRG	Switched reluctance generator
SRM	Switched reluctance motor
TSF	Torque sharing function

LIST OF APPENDICES AND ANNEXES

Appendix A– Fast Estimation of Mechanical Parameters for Switched Reluctance Motors Drives Based on PSO Algorithm	141
Appendix B– Robust speed control by means of linear matrix inequalities	153
Appendix C– Experimental setup	161

CONTENTS

1 INTRODUCTION	27
1.1 MOTIVATION	27
1.2 SWITCHED RELUCTANCE MACHINES	31
1.3 THESIS PROPOSAL OUTLINE	32
1.4 ADVANCED CONTROL OF SRMs	33
1.5 REVIEW OF SRM FIRING ANGLE OPTIMIZATION	34
1.6 REVIEW OF SRM TORQUE SHARING FUNCTIONS	36
1.6.1 Analytical torque sharing functions	36
1.6.2 Dynamically allocated torque sharing functions	37
1.6.3 Numerically optimized torque sharing functions	38
1.6.4 Comparison of the TSF strategies	39
1.7 REVIEW OF SRM CURRENT CONTROL	40
1.7.1 Model-independent methods	41
<i>1.7.1.1 Conventional current chopping control</i>	41
<i>1.7.1.2 Intelligent controllers</i>	41
1.7.2 Model-based methods	42
<i>1.7.2.1 Linear controllers</i>	42
<i>1.7.2.2 Dead-beat current controller</i>	44
<i>1.7.2.3 Model predictive current controller</i>	45
<i>1.7.2.4 Adaptive current controller</i>	46
<i>1.7.2.5 Sliding mode current controller</i>	47
1.7.3 Comparison of the current control strategies	49
1.8 THESIS CONTRIBUTIONS	50
1.9 THESIS STRUCTURE	51
2 SWITCHED RELUCTANCE MACHINE FUNDAMEN- TALS	53
2.1 INTRODUCTION	53
2.2 SWITCHED RELUCTANCE MACHINE CHARACTERISTICS	53
2.3 INDUCTANCE PROFILE	54
2.4 SWITCHED RELUCTANCE MACHINE OPERATION	57
2.4.1 Phase excitation	58
2.4.2 Asymmetric half-bridge converter	58
2.5 SWITCHED RELUCTANCE MOTOR CONTROL	60
2.5.1 Current control	61
2.5.2 Single pulse control	63
2.6 MODELING	64

2.6.1 Electrical model	64
2.6.2 Torque	65
<i>2.6.2.1 Non-linear analysis</i>	66
<i>2.6.2.2 Linear analysis</i>	67
2.6.3 Mechanical model	68
2.7 SIMULINK MODEL	68
2.8 CONCLUSIONS	71
3 PARTICLE SWARM BASED FIRING ANGLE OPTI- MIZATION	73
3.1 INTRODUCTION	73
3.2 FIRING ANGLES	73
3.3 FINE GRID OPTIMIZATION	74
3.4 PARTICLE SWARM OPTIMIZATION	75
3.5 SRM FIRING ANGLE OPTIMIZATION ALGORITHMS	76
3.5.1 Fine grid optimization procedure	78
3.5.2 Particle swarm optimization procedure	82
3.5.3 Optimization procedures comparison	84
3.5.4 Load sensitivity	85
3.6 EXPERIMENTAL RESULTS	86
3.7 CONCLUSION	91
4 DISCRETE-TIME SUPER-TWISTING SLIDING MODE CURRENT CONTROLLER WITH FIXED SWITCHING FREQUENCY	93
4.1 INTRODUCTION	93
4.2 DISCRETE-TIME SUPER-TWISTING SLIDING MODE CURRENT CONTROLLER ..	94
4.2.1 Controller structure	95
4.2.2 Stability analysis	96
4.3 GAIN DESIGN PROCEDURE	101
4.3.1 Design procedure	101
4.3.2 Design example	102
4.4 EXPERIMENTAL RESULTS	105
4.4.1 Steady state performance	108
4.4.2 Dynamic performance	111
4.4.3 Efficiency comparison	115
4.4.4 Computational burden comparison	116
4.5 CONCLUSION	116
5 CONCLUSIONS AND PERSPECTIVES	119
5.1 FINAL CONSIDERATIONS	119
5.2 FUTURE WORK	120

CONTENTS

5.3 PUBLICATIONS	121
REFERENCES	125
APPENDICES	139

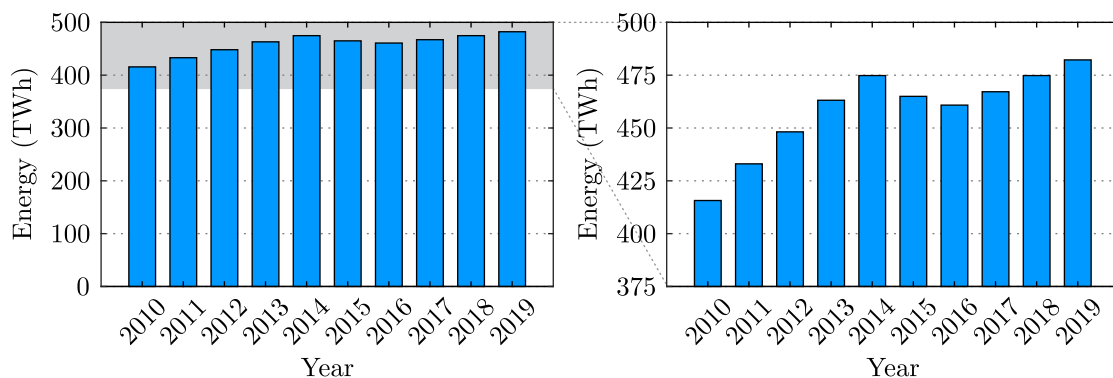
1 INTRODUCTION

1.1 MOTIVATION

Energy consumption has become a topic of great interest in recent decades, being the focus of debates, government programs and research worldwide. This concern is based on the growing demand for energy, combined with the search for a reduction in the emission of greenhouse gases, harmful to the environment and to the world's population. Consequently, several researches related to energy efficiency, optimization of processes and replacement of fossil fuels by renewable sources have been carried out in recent years.

In the national scenario, there has been a significant increase in the consumption of energy over the past 10 years. This phenomenon can be seen in Figure 1.1, where data on electrical energy consumption from Brazil between the years 2010 and 2019 are presented. The data are taken from the Statistical Yearbook of Electric Energy by the Brazilian Company of Energy Research (2020). It shows that between the years 2009 and 2014, the country's energy consumption grew by 23.55%, while the population, in the same period, grew only 8.04% (WORLD BANK, 2020). In the 2014-2016 period, there was a drop in consumption, justified by the economic recession in Brazil. In 2017, however, electrical energy consumption started growing once again.

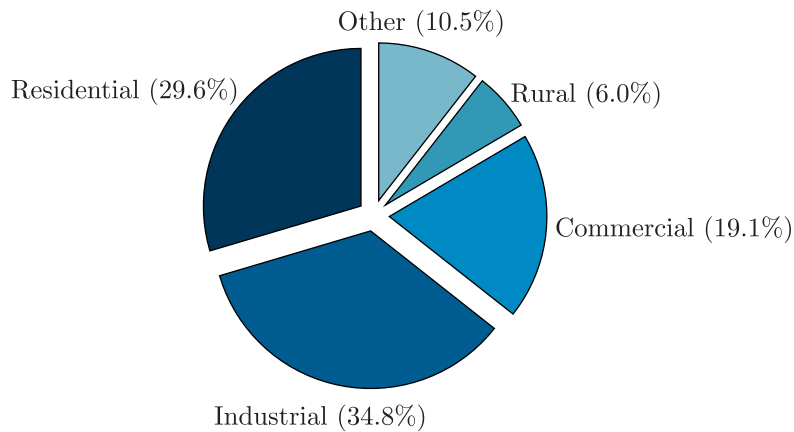
Figure 1.1 – Electrical energy consumption in Brazil between the years 2010 and 2019.



Source: Adapted from (BRAZILIAN COMPANY OF ENERGY RESEARCH, 2012) and (BRAZILIAN COMPANY OF ENERGY RESEARCH, 2020).

The increase in the use of electrical energy in the world is usually related to production, given a large part of the energy generated is consumed by the industrial sector. This is also true in the Brazilian scenario, with the industrial sector accounting for 34.8% of the country's electric energy consumption, according to data from the 2020 Statistical Yearbook for Electric Energy (2019 baseline year), as seen in Figure 1.2.

Figure 1.2 – Electrical energy consumption by type of consumer in Brazil in 2019.



Source: Adapted from (BRAZILIAN COMPANY OF ENERGY RESEARCH, 2020).

A large portion of the energy consumed by the industry is in the form of motion, through electric motors. Electric motors are cost effective devices capable of electromechanical energy conversion, however, during this process some of the energy is lost, mainly in the form of heat. The use of electric motors is seen in applications such as electric traction, conveyor belts, hydraulic pumps, industrial fans and blowers, compression, among others. Thus, the search for electric machines with better performance is of interest.

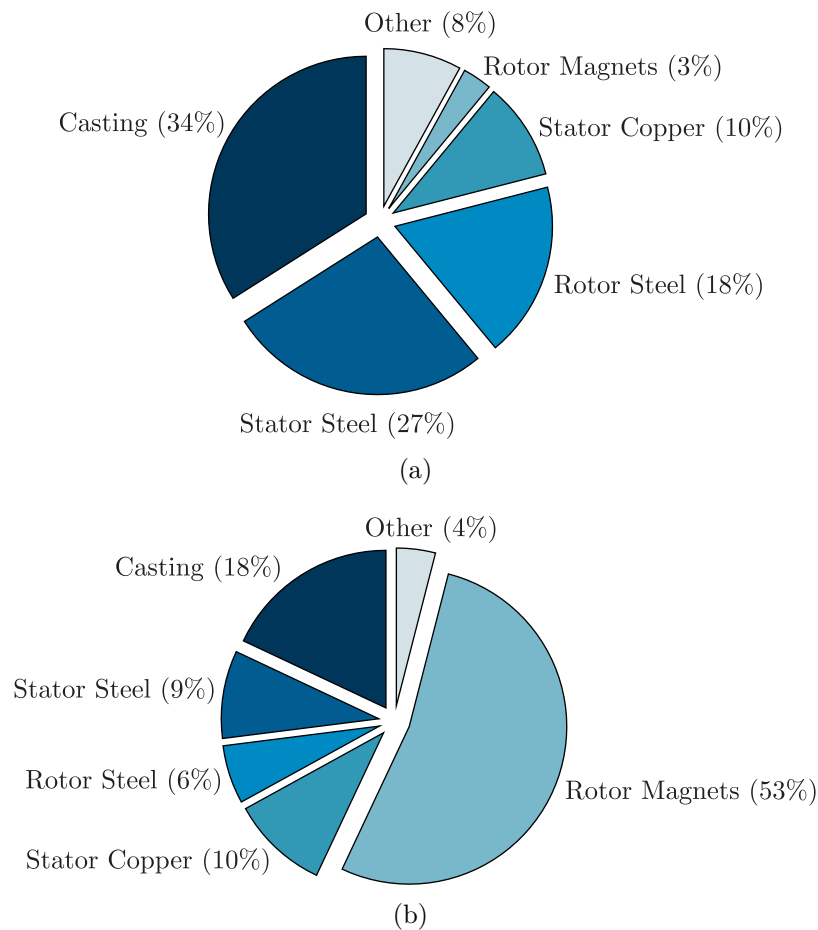
Induction Motors (IM) are the most commonly used electric motors for industrial applications. Among its advantages stand out the high robustness, low cost of manufacturing and acquisition, reduced maintenance and line-starting capability, removing the need for an inverter in a fixed speed operation. However, the IM is an asynchronous machine, meaning that the rotor speed is slower than the speed of the rotating magnetic field. This phenomenon leads to currents being induced in the rotor bars of the machine and generating its own magnetic field, which interacts with the stator field and leads to torque production. The existence of rotor currents results in copper losses and significant heating of the machine. As a result, the IM has a poor efficiency when compared to other synchronous machines (BOGLIETTI et al., 2006).

In the search for more efficient machines, the use of Permanent Magnet Synchronous Motors (PMSM) is a visible trend in industrial and electric vehicle applications (WANG et al., 2021; FILHO et al., 2021). By means of permanent magnets, the PMSM presents independent rotor excitation, allowing the design of a machine with high torque density, often resulting in a volume reduction. In addition, unlike the IM, PMSMs present negligible rotor losses, which contribute to a higher efficiency (PILLAY; KRISHNAN, 1989). While the permanent magnets allow for machine weight and volume reduction, they present several mechanical and thermal limitations. High speed operation can lead surface magnets to being detached from the rotor and thermal stress can permanently

damage the characteristics of the material (GIERAS, 2014). Moreover, for high speed operation, PMSM typically have to be operated in a field weakening region due to voltage constraints (PREINDL; BOLOGNANI, 2013; MYNAR; VESELY; VACLAVEK, 2016).

For the production of PMSMs, rare earth magnets such as Samarium Cobalt (SmCb) and Neodymium Iron Boron (NeFeB) are often used. Such materials have a high cost, making the machine a very expensive alternative and restricting its applications. Figure 1.3 shows the weight and cost distribution, respectively, between the components of an 80 kW interior permanent magnet machine, designed for vehicle traction. It can be noted that the permanent magnets account for over 50% of the cost of the machine, while only representing 3% of the overall weight (MILLER, 2013; BILGIN; JIANG; EMADI, 2019).

Figure 1.3 – Data from PMSM manufacturing. (a) Distribution of weight. (b) Distribution of cost.

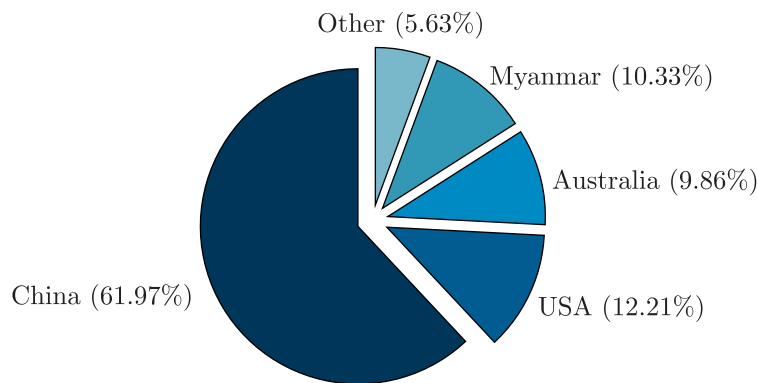


Source: Adapted from (MILLER, 2013; BILGIN; JIANG; EMADI, 2019).

In addition, the permanent magnet market is quite restricted. A large part of the reserves of rare earth materials, required for the manufacturing of permanent magnets, are concentrated in Chinese territory. According to the United States Geological Survey

(USGS), the world rare-earth-oxide extraction in 2019 was 210,000 metric tons (UNITED STATES GEOLOGICAL SURVEY, 2020). Figure 1.4 shows the percentage extraction by country, where it can be seen that China is responsible for 61.97 % of world's extraction. Moreover, rare-earth magnets present price volatility and supply chain issues, making the industry dependent on the supply of magnets from the Chinese market, being subject to its economic policies and possible sanctions (BILGIN; JIANG; EMADI, 2019). Lastly, the extraction and refining of rare earth material, as well as the manufacturing process of permanent magnets can lead to environmental impacts, which are also undesirable (BALARAM, 2019).

Figure 1.4 – World mine production of rare-earth-oxide material in 2019.



Source: Adapted from (BILGIN; JIANG; EMADI, 2019).

Therefore, a paradigm shift is expected when it comes to electrical machines. A motor with improved efficiency, when compared to a IM, and reduced production costs, when compared to a PMSM, is of interest. In this context, the use of reluctance-based machines is a viable alternative.

A type of reluctance-based machine is the Synchronous Reluctance Motor (SynRM). The SynRM presents a simple structure, mechanical robustness and low cost due to the absence of windings or magnets in its rotor structure. Compared to IMs, SynRMs present an improved efficiency and lower operating temperatures, due to the near absence of rotor losses (BOGLIETTI et al., 2006). When compared to the PMSMs, the SynRM presents a notably lower cost, given it does not present permanent magnets in its construction. Moreover, SynRMs presents sinusoidal excitation, allowing the use of drives already developed for PMSMs and IMs, without any physical changes (SCALCON et al., 2021). Furthermore, the machine presents some limitations, such as limited torque output when compared to PMSMs. In addition, increased torque ripple and poor power factor are also observed (OKAMOTO et al., 2018).

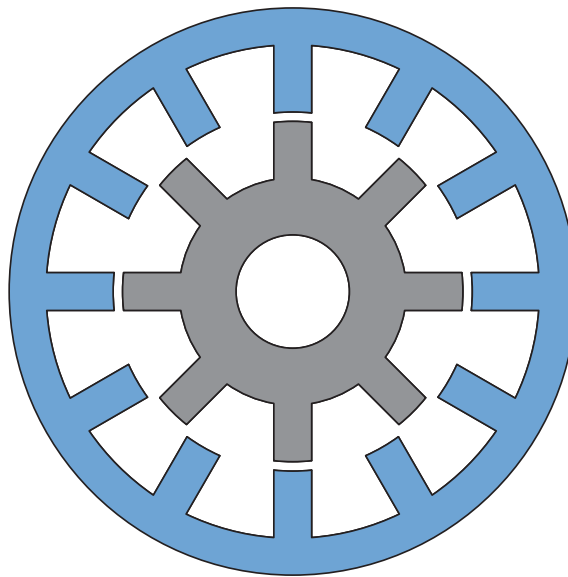
Another kind of reluctance-based machine is the switched reluctance motor, which will be discussed in the following section and is the main topic of this thesis.

1.2 SWITCHED RELUCTANCE MACHINES

Switched reluctance machines have gained interest in the past couple of decades, with literature indicating it as a viable competitor for already established electrical machines. The machine presents a simple construction, composed of a double salient structure, with concentrated windings mounted on the stator slots. The rotor of the machine is composed of a series of laminated steel pieces stacked together (BILGIN; JIANG; EMADI, 2019). As an example, a cross section of a 12/8 machine can be observed in Figure 1.5.

The torque production in a switched reluctance motor (SRM) is a result of the double salient structure of the machine and the magnetic field produced by the stator coils, leading to the production of reluctance torque. This presents itself as an advantage given that the machine does not rely on magnets or induced currents for rotor excitation. Due to its simple structure, the material costs of the machine are lower and the manufacturing process is simpler, when compared to PMSMs (STATON; MILLER; WOOD, 1993; KRISHNAMURTHY et al., 2006; BOLDEA et al., 2014).

Figure 1.5 – Cross section of a 12/8 switched reluctance machine.



Source: Author.

Switched reluctance machines are also able to operate in a wide range of speed with good efficiency. PMSMs, for instance, have output limitations due to the fixed DC link voltages and increase of back electromotive force (back-EMF) with speed, requiring field weakening strategies for high speed operation. However, SRMs rely only on the double salient structure for torque production, thus, not requiring any field weakening strategies. This makes the SRM a more interesting candidate for high speed operation, when compared to a PMSM, for example (KIYOTA; CHIBA, 2012; BILGIN et al., 2015).

Another advantage of switched reluctance machines is the inherent fault tolerance. This happens because of the machine construction, where each phase is made of concentrated individual windings. Given that each phase is isolated from the other, the machine can continue to operate even under a fault condition, with degraded performance. This is of interest for automotive and aerospace applications, for example (JACK; MECROW; HAYLOCK, 1996; BOLDEA et al., 2014; SUN et al., 2021).

Nevertheless, the switched reluctance machine has some drawbacks. The machine presents a highly non-linear behavior due to the double salient structure, magnetic saturation and position dependent phase inductances. These effects make the analysis of the SRM a more complex task (LI, 2017). In addition, current control becomes a bigger challenge, requiring the use of robust control strategies. Hysteresis current control is often used as a solution, but variable switching frequency is still an issue for electromagnetic interference (EMI) design, for example.

Moreover, the SRM is prone to high torque ripple, with the switched nature of the machine being one of the contributing factors. During phase commutation, the torque generated by each phase is added together, resulting in a pulsated waveform. High frequency switching resultant from the current controller also contributes to torque oscillations. Torque ripple is undesirable given that it can lead to mechanical vibrations, that deteriorate the machine over time.

Therefore, it can be seen that the SRM presents several advantages that make it a competitive alternative to other electric machines available on the market. However, it also exhibits a series of challenges, specially regarding its control. In order to mitigate the main drawbacks, various research papers propose different advanced control strategies, which will be detailed in the next sections.

1.3 THESIS PROPOSAL OUTLINE

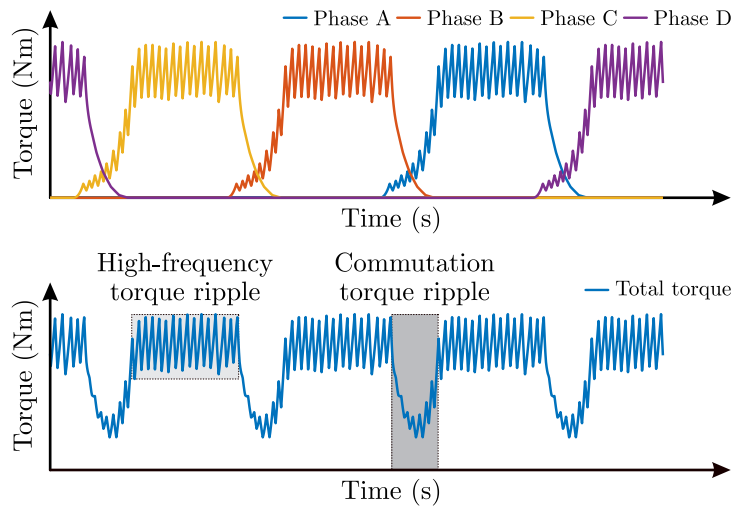
This thesis proposal has as a main objective improving the performance of SRMs through the use of advanced control strategies. By effectively reducing the torque ripple of the machine, it is possible to mitigate many of the previously mentioned disadvantages. Moreover, performance enhancement tools like these can help making an SRM drive viable for consumer applications, competing with already established IM and PMSM drives.

In the following sections, a state-of-the-art review of some of these advanced control strategies will be presented.

1.4 ADVANCED CONTROL OF SRMS

As previously mentioned, one of the main drawbacks of SRMs is the high torque ripple. Two major sources of torque ripple are present in SRMs: the commutation torque ripple and the high-frequency torque ripple (FANG et al., 2021a). The phenomenon can be observed in Figure 1.6, where a typical torque waveform for an SRM is presented.

Figure 1.6 – Sources of torque ripple in switched reluctance motors.

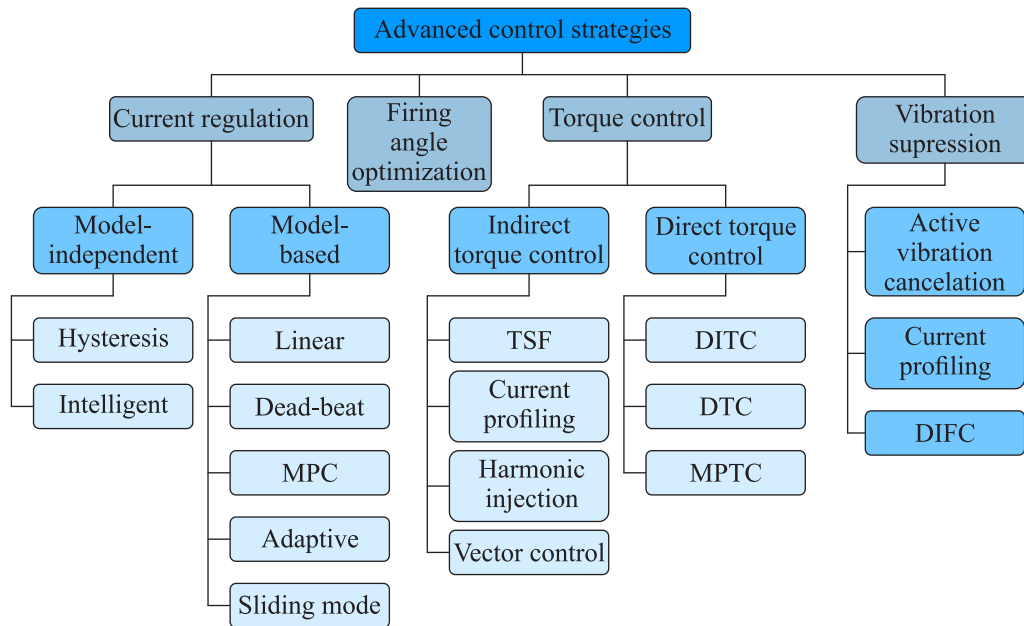


Source: Author.

The commutation torque ripple is a result of the inherent switched nature of the machine. A significant drop in torque production is observed in the commutation interval, when the outgoing phase is demagnetized and the incoming phase is excited. It should be noted that commutation often accounts for the majority of the observed torque ripple. On the other hand, high-frequency torque ripple is a result from the switching action of a current or torque regulation technique. As the name implies, it presents a high-frequency characteristic and can be affected by factors such as hardware, machine parameters, sampling and switching frequencies, among others. High-frequency torque ripple is generally less noticeable than commutation torque ripple.

In this context, advancements in power electronics and computational power of microprocessors in the past decades allowed research on SRMs to increase significantly, with torque and torque ripple characteristics of the machine emerging as a topic of interest. Over the years, several studies have been conducted in order to improve the current regulation, torque control and vibration suppression in SRMs. As a result, several advanced control strategies have been proposed for SRMs, as depicted in the diagram of Figure 1.7.

Figure 1.7 – Advanced control strategies for switched reluctance motors.



Source: Author.

Although several advanced control strategies have been developed, this thesis will focus on three techniques: firing angle optimization, torque sharing functions and current regulation. In the following subsections, a state-of-the-art review of each of these strategies will be presented.

1.5 REVIEW OF SRM FIRING ANGLE OPTIMIZATION

During operation, the angles at which phase excitation occurs, known as firing angles, play an important role in the drive performance. Proper choice can lead to reduced torque ripple or an overall higher efficiency. Due to the lack of simple analytical formulation for determining these parameters, in recent years, several research papers have aimed to improve the performance of the SRM through the firing angle optimization (FISCH et al., 1997; TORREY, 2002; MADEMLIS; KIOSKERIDIS, 2003; KIOSKERIDIS; MADEMLIS, 2005; MADEMLIS; KIOSKERIDIS, 2005; KIOSKERIDIS; MADEMLIS, 2009; XUE et al., 2010; BARROS et al., 2016; NETO et al., 2018).

In (FISCH et al., 1997) a genetic algorithm is used in order to optimize the firing angles to maximize torque production. In (MADEMLIS; KIOSKERIDIS, 2003) and later (KIOSKERIDIS; MADEMLIS, 2005), extensive analyses regarding the impact of the firing angles on the performance of SRMs operating below and above base speed are presented, respectively. In both cases, online angle commutation is performed. Such controllers do not require the magnetization curves of the machines. Experimental results show that

the proposed techniques improve the overall performance of the motor and a balance between torque ripple and energy efficiency is accomplished. The proposals are unified in (KIOSKERIDIS; MADEMLIS, 2009), where a strategy for the entire range of operation is discussed.

In (XUE et al., 2010) an optimal control method for electric vehicle SRM drives based on a multi-objective optimization is presented. Three factors are taken into account: maximum average torque, maximum average torque per RMS current and torque smoothness factor. Experimental results show that online angle commutation is able to achieve optimal operation.

In (TORREY, 2002) the impact of the firing angles on the operation of a switched reluctance generator (SRG) is discussed. A performance optimization for SRGs operating below base speed is proposed in (MADEMLIS; KIOSKERIDIS, 2005), where a balance between torque ripple and energy efficiency is achieved. More recently, a multi-objective performance optimization based on design of computational experiments applied to SRGs is proposed in (NETO et al., 2018). Optimal firing angles are determined at different speeds by a cost function containing normalized torque ripple, RMS current and peak flux. Two different space-filling designs are compared: one-factor-at-time and Latin hypercube sampling, with the latter being capable of significantly reducing computational effort. Optimal angles are implemented as a function of speed and experimental results are presented for both low and high speed operation, showing a balance between torque ripple and system efficiency.

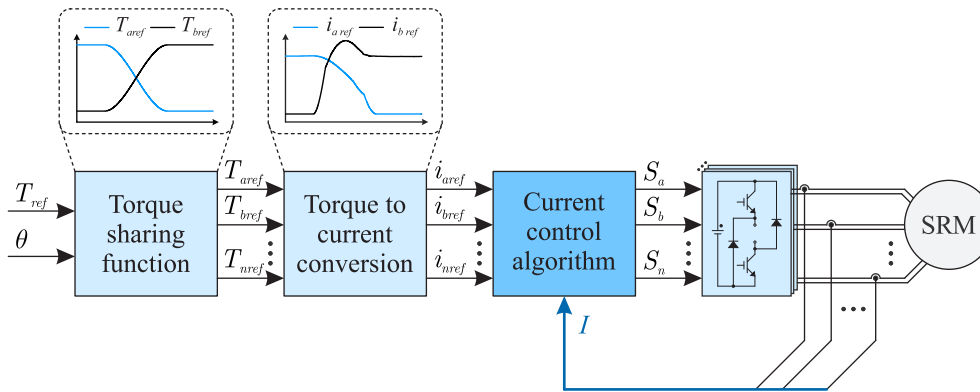
Although optimal angles can be determined and are relatively easy to be implemented, the technique presents some limitations. These methods usually rely on rectangular current references, which lead to noticeable torque ripple in the commutation region, even when considering optimized parameters (BILGIN; JIANG; EMADI, 2019). Thus, the use of advanced control techniques is necessary to achieve effective torque ripple reduction in SRMs. In this context, a state-of-the-art review of SRM torque sharing functions will be presented in the following section.

1.6 REVIEW OF SRM TORQUE SHARING FUNCTIONS

Torque sharing functions (TSF) have been extensively investigated in literature, as the technique is effective at mitigating commutation torque ripple in SRM drives. Torque sharing functions distribute a given torque reference among different SRM phases, ensuring that the sum of the total torque produced by each phase matches the expected value (LI; BILGIN; EMADI, 2019). During commutation periods, the torque is shared between two phases, the incoming and the outgoing.

With the generated torque references, a lookup table is used to convert the torque references into current references. Given the nonlinear characteristic of the SRM, these waveforms often present different shapes. The resulting reference current waveforms are then used as inputs for a current controller, which will track them in order to produce the desired torque. An example block diagram of a TSF strategy is presented in Figure 1.8.

Figure 1.8 – Example block diagram of a TSF strategy.



Source: Author.

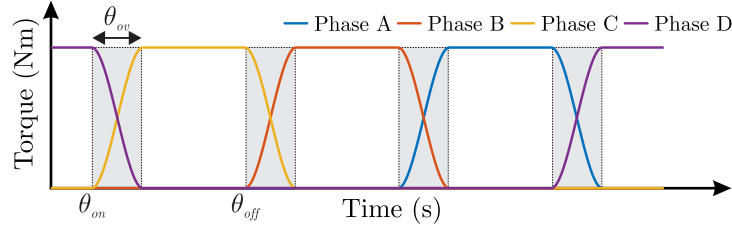
TSFs can be divided in three different categories: analytical TSFs, dynamically allocated TSFs and numerically optimized TSFs (FANG et al., 2021a). A brief review of each kind will be presented in the following subsections.

1.6.1 Analytical torque sharing functions

Analytical TSFs are the most straightforward approach to torque sharing, being often observed in literature. This strategy makes use of mathematical expressions to share the torque between the incoming and outgoing phases. Some examples of analytical TSFs are based on linear (SCHRAMM; WILLIAMS; GREEN, 1992), sinusoidal (ILIC-SPONG et al., 1987), exponential (HUSAIN; EHSANI, 1996) and cubic (SAHOO; XU; PANDA, 1999) functions. An example of the cubic TSF is presented in Figure 1.9, where θ_{on} , θ_{off}

and θ_{ov} are the turn on, turn off and overlap angles, respectively.

Figure 1.9 – Example phase torque references produced by a cubic TSF.



Source: Author.

Several parameters can be tuned in order to improve the performance of analytical TSFs, such as the overlap angles and the used function, for example. The performance optimization of analytical TSFs is investigated in (XUE; CHENG; HO, 2009). The study shows that with adequate turn on and overlap angles, improved performance is observed. A genetic algorithm is used as a means to obtain the optimal parameters, while also minimizing copper losses and extending the speed range. In (VUJICIC, 2012), analytical TSFs are optimized considering secondary objectives, such as copper losses minimization and drive performance maximization. A total of four TSFs are evaluated, with a family of novel TSFs with minimized p-norm being introduced.

Although analytical TSFs are effective at torque ripple reduction and can be further optimized for performance, some drawbacks are still observed. Due to DC bus voltage restrictions, SRM drives present a limited flux linkage rate of change, resulting in current tracking limitations, specially in high speed and high load conditions. Given that the performance of TSFs is directly dependent on accurate current tracking, this can lead to a loss in performance. As a result, TSFs that take the drive limitations into consideration have been proposed, as will be depicted in the following subsection.

1.6.2 Dynamically allocated torque sharing functions

Unlike analytical TSFs, dynamically allocated TSFs are able to address the high speed and load limitations of analytical torque sharing functions by considering the current tracking and torque production capabilities of an SRM drive in the reference generation process (FANG et al., 2021a).

The linear TSF, originally presented in (SCHRAMM; WILLIAMS; GREEN, 1992), is improved in (TSENG; CAO, 2001). The proposal accelerates phase commutation and adaptively readjusts the torque references, while also reducing the performance dependence on the turn on and turn off angles. A modified TSF for high speed operation is presented in (LEE et al., 2011). Torque compensation is provided by the incoming phase

in order to overcome the short commutation period and large tail currents observed in high speed situations. Similar strategies are also reported in (DOWLATSHAHI; NEJAD; AHN, 2013) and (GAN et al., 2021).

In (ROHAK-SEUNG et al., 2015) a fuzzy logic controller is combined with a TSF in order to provide adequate torque control, specially at high speed conditions. Additional intelligent control strategies are also reported in literature as a means to improve analytical TSFs. These strategies make use of techniques such as iterative learning controllers and neural networks, for example (SAHOO; XU; PANDA, 2001; SAHOO; PANDA; XU, 2005; LIN et al., 2006).

A nonlinear TSF is proposed in (LEE et al., 2009). The proposal uses torque error measurements in a feedback loop in order to improve tracking. In (YE; BILGIN; EMADI, 2015b), an extended speed range TSF is presented. Two operation modes are defined, determined by whether the incoming or outgoing phase presents the higher absolute value of flux linkage rate of change. A PI (proportional-integral) compensator based on torque error is used to improve performance. A similar technique is also proposed in (SUN et al., 2016).

Even though full range operation can be achieved with dynamically allocated TSFs, other metrics are also relevant in the evaluation of TSFs, such as copper losses, torque-speed performance and efficiency (BILGIN; JIANG; EMADI, 2019). Due to the complex nature of such formulations, optimization-based TSFs have also been investigated, as will be presented in the following subsection.

1.6.3 Numerically optimized torque sharing functions

Numerically optimized TSFs rely on optimization algorithms, such as the genetic algorithm (GA) or particle swarm optimization (PSO), to determine current profiles that achieve torque ripple reduction. A key advantage of this method is the fact it considers secondary objectives in the optimization procedure, such as improved efficiency, ripple-free speed or superior high speed performance, for example (FANG et al., 2021a).

In (LOVATT; STEPHENSON, 1997), optimal current references are generated with the objective of minimal RMS current, while also considering voltage limitations. TSFs are optimized in (CHOI et al., 2002) in order to allow negative torque production. The proposal has several advantages, such as being suitable for high speed operation and presenting low memory requirements, given that the current waveforms are represented by a series of B-splines. Secondary objectives, such as power losses and voltage limitations are also considered.

An offline TSF for torque ripple reduction in SRMs is proposed in (YE; BILGIN; EMADI, 2015c). The objective function is composed of two secondary objectives: min-

imization of the square phase current value and the current reference derivatives. The optimization problem is solved using the Lagrange multipliers method. A performance comparison between the proposal and analytical TSFs in the linear and magnetically saturated regions is also provided. In (LI; BILGIN; EMADI, 2019), an improved TSF for torque ripple reduction is presented. Once more, an offline approach is used, taking advantage of the flux linkage characteristics of the machine. Optimal current profiles are determined for minimal losses, while maintaining low torque ripple. Moreover, the proposal makes use of a single weight parameter, reducing complexity.

A new torque sharing function is proposed in (XIA et al., 2021). A new reference current generation is established as a means to achieve lower current tracking error. Minimal copper losses and torque ripple are the optimization objectives, while also ensuring adequate average torque production. A time-efficient torque shaping procedure is presented in (FANG et al., 2021c). A linear space torque mapping approach is used in order to accelerate the time-consuming optimization problem. Low memory requirements are also observed, given the polynomial-based implementation.

1.6.4 Comparison of the TSF strategies

A comparison of TSFs strategies reported in literature is presented in Table 1.1. The previously discussed techniques are compared in terms of advantages, disadvantages and computational complexity.

Table 1.1 – Summary and comparison of the SRM TSF strategies.

Technique	Advantages	Disadvantages	Computational complexity
Analytical TSFs	Simplicity, easy implementation, good low speed performance	Poor high speed performance, limitations are not considered, angle dependence	Low
Dynamically allocated TSFs	Full range capability, good high speed performance	Secondary objectives are not considered	Medium
Numerically optimized TSFs	Full range capability, consideration of secondary objectives	High computational complexity, large memory storage requirements	High

Source: Author.

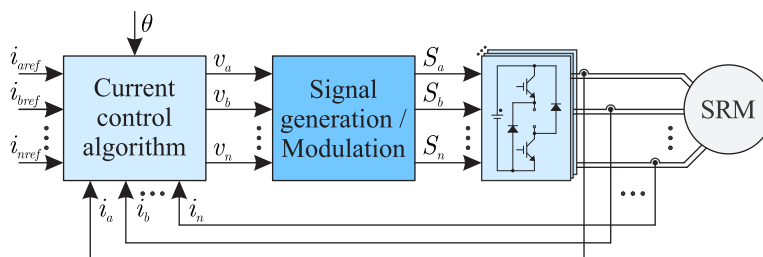
Analytical TSFs present simple implementation and are based on known mathematical functions. However, the technique presents poor high speed performance, given it does not consider the voltage limitations of the SRM drive. Moreover, the strategy is dependent on adequate turn on and overlap angle selection. Dynamically optimized TSFs are capable of full range operation, as they consider current and torque limitations in the reference generation process. Although improved performance is observed, the technique does not take into consideration secondary objectives. Lastly, numerically optimized TSFs present wide speed range capability while also achieving superior performance, given that secondary objectives are considered in the optimization problem. The main disadvantages of this approach are the high computational complexity and large memory storage requirements.

1.7 REVIEW OF SRM CURRENT CONTROL

In order to minimize the torque ripple in SRM drives using TSFs, a current controller must be able to track the expected current reference value provided by the TSFs. Moreover, the tracking capability and ripple of the current controller directly impact the performance of the torque sharing scheme. However, as it was previously mentioned, the SRM presents significant control challenges regarding its highly nonlinear behavior, due to varying phase inductance and magnetic saturation. As a result, high performance current control techniques have been investigated over the years.

In the following subsections, different current control strategies for SRMs are presented, highlighting their advantages and disadvantages. They are divided in model-independent and model-based strategies. A general SRM current control block diagram can be seen in Figure 1.10.

Figure 1.10 – General block diagram for SRM current control.



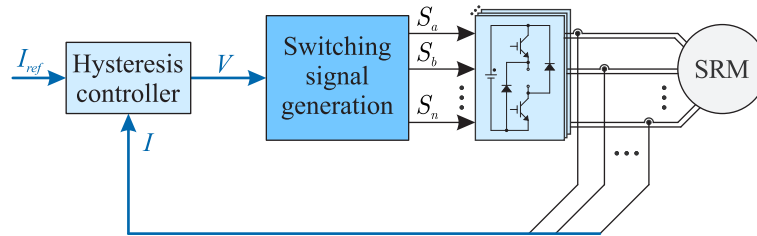
Source: Author.

1.7.1 Model-independent methods

1.7.1.1 Conventional current chopping control

Current chopping control is the most commonly applied method in SRM current control due to its model independence and fast dynamic response (PENG; EMADI, 2014). The strategy basically consists on the use of a hysteresis controller with a predetermined hysteresis band. Two different methods, named hard chopping and soft chopping, are characterized by the use of negative and zero voltage levels, respectively. The discrete number of possible switching states (1, 0 and -1) and the limited sampling frequency significantly affect the reference tracking capability of this strategy. The resulting current ripple will be much more obvious at low-speed operation and for low inductance SRMs (BILGIN; JIANG; EMADI, 2019). It should also be noted that the switching frequency varies in accordance with the sampling frequency and current hysteresis band, so the electromagnetic interface should be carefully considered in the EMI design. Different methods have been reported in the literature to address the above-mentioned issues, while also seeking to improve current tracking capability. The block diagram of a hysteresis current control approach is presented in Figure 1.11.

Figure 1.11 – Example block diagram for SRM hysteresis current control.



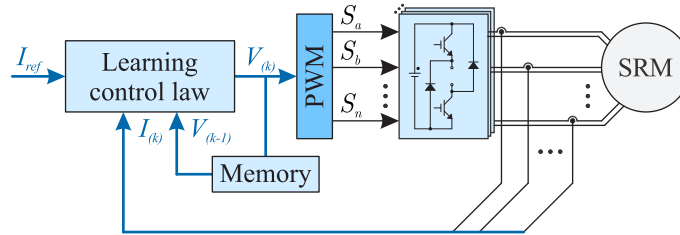
Source: Author.

1.7.1.2 Intelligent controllers

As an alternative to the hysteresis controller, but still within the field of model-independent strategies, intelligent control techniques have been investigated (SAHOO; XU; PANDA, 2001; SAHOO; PANDA; XU, 2004; ZHENG et al., 2008; YI et al., 2010; LAI et al., 2014; ALHARKAN et al., 2020). These strategies often rely on a learning mechanism in order to improve the controller's response. This can be performed online, with the controller being tuned by experimental measurements, or offline, based on sequential simulation results. The main advantages of such techniques are the ability to deal

with highly nonlinear behavior, the ability to adapt over time to parametric changes and the fact they are model independent. In addition, these techniques may be implemented using pulse-width modulation (PWM), resulting in a fixed switching frequency. The main drawbacks of these techniques are the relative slow learning process, the need for training data and significant computational complexity. An example block diagram of an iterative learning current controller is depicted in Figure 1.12.

Figure 1.12 – Example block diagram for SRM iterative learning current control.



Source: Author.

In (SAHOO; XU; PANDA, 2001) a two-stage low torque ripple SRM control scheme is presented, where an Iterative Learning Control (ILC) approach is used for both torque and current control. The authors further investigate the use of ILC for current regulation in (SAHOO; PANDA; XU, 2004), and propose a novel P-type feedback controller using an ILC block as a feedforward controller. The P-controller is tuned separately to achieve the best possible tracking performance, and once the torque reference stabilizes, the ILC further enhances current tracking. A Q-learning algorithm is used in (ZHENG et al., 2008) to provide adequate current tracking for SRMs. A scheduling mechanism is used in order to cope with the Q-learning algorithm limitations. Additional ILC based approaches are presented in (YI et al., 2010), (LAI et al., 2014) and (ALHARKAN et al., 2020).

Other intelligent control techniques such as Artificial Neural Networks (ANN) and fuzzy logic have been evaluated for torque control, torque sharing and current profiling of SRMs. However, note that, to the best of the author's knowledge, these techniques have not yet been considered in order to address the current regulation problem in SRMs.

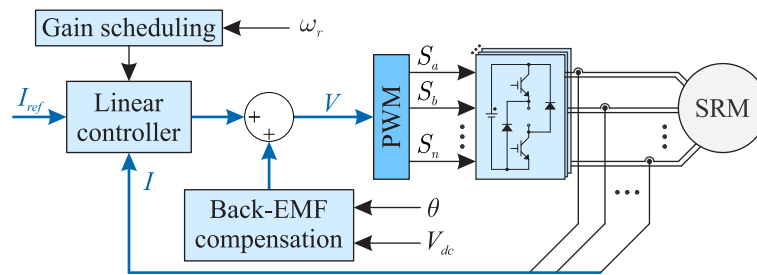
1.7.2 Model-based methods

1.7.2.1 Linear controllers

Linear controllers, such as the PI controller, are standard in industry applications. Several papers have investigated the use of these controllers for the current control of SRMs (HUSAIN; EHSANI, 1996; BAOMING; NAN, 2006; ILIC'-SPONG et al., 1987; ARAB et al., 2013; WANG; LAI, 2002; BANERJEE; SENGUPTA; DALAPATI, 2014;

MILASI; MOALLEM, 2014; AHMAD; NARAYANAN, 2016; SCHULZ; RAHMAN, 2003; SCHRODER; BEKIESCH, 2005; LIN et al., 2010; HUANG et al., 2016; HANNOUN; HILAIRET; MARCHAND, 2007; OUDDAH et al., 2014; SONG; SONG; QU, 2016). These strategies make use of mainly PI controllers to calculate a duty cycle for a PWM signal, based on the current tracking error. State feedback controllers have also been reported in (ILIC'-SPONG et al., 1987) and (ARAB et al., 2013), for example. Advantages such as a fixed switching frequency and lower current ripple when compared to hysteresis controllers are observed. Figure 1.13 presents the block diagram of a possible linear control approach for SRM current control.

Figure 1.13 – Example block diagram for SRM linear current controllers.



Source: Author.

Due to the non-linear nature of the SRM, however, the design of linear controllers becomes a challenging task. To overcome this issue, some papers present a linearized modeling of SRMs for the design of closed-loop current controllers. Small-signal modeling is presented in (WANG; LAI, 2002) and (BANERJEE; SENGUPTA; DALAPATI, 2014), where a linear SRM model is derived from nominal operating conditions. In (MILASI; MOALLEM, 2014) an SRM is also linearized around its nominal operating point, allowing the gains of a PI controller to be tuned. In (AHMAD; NARAYANAN, 2016), a small-signal model is built initially, based on the inductance profile of the machine. Then, it is used for the design of a fixed gain PI controller.

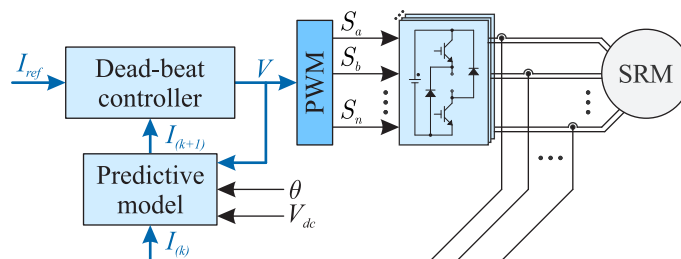
The back-EMF of the machine is a disturbance that affects current control in SRMs, generally degrading the tracking capabilities of the controllers at medium and high speeds (AHMAD; NARAYANAN, 2016). As a solution, some strategies make use of EMF compensation. In (SCHULZ; RAHMAN, 2003) and (SCHRODER; BEKIESCH, 2005) back-EMF is estimated offline, from flux linkage data. The results are then stored in lookup tables, which are used in the digital implementation. In (LIN et al., 2010) online estimation is performed by means of a neural network, not requiring prior knowledge of the machine's characteristics. A back-EMF observer is used in (HUANG et al., 2016) to achieve back-EMF cancellation. Even though ideal cancellation cannot be obtained, the technique allows the current changing rate to be increased. Moreover, the burden over the employed PI controller is lessened, with the remaining error being eliminated by

it. A simple estimation method is presented in (AHMAD; NARAYANAN, 2016), where the back-EMF is calculated based on the SRM model. The resulting strategy is not computational or memory intensive. Another alternative for improving the performance of linear controllers is the use of gain scheduling strategies (HANNOUN; HILAIRET; MARCHAND, 2007; OUDDAH et al., 2014; SONG; SONG; QU, 2016). In (HANNOUN; HILAIRET; MARCHAND, 2007) a variable gain PI controller is proposed, where the gains are adjusted as a function of both current and rotor position, ensuring better tracking performance. A parameter dependent controller using the linear parameter varying control approach is presented in (OUDDAH et al., 2014). A H_∞ control extension is chosen to design a gain scheduled current controller, by means of a polytopic representation. A convex optimization problem is built and, after solving linear matrix inequalities, the so-called self-scheduled controller is obtained by interpolation.

1.7.2.2 Dead-beat current controller

Alternative control techniques, such as dead-beat controllers, have also been investigated for the current control of SRMs. Dead-beat control makes use of a predictive model as a means to determine which voltage value should be applied in order to produce zero tracking error in one sample period. This technique presents as a main advantage a fast dynamic response. Moreover, dead-beat controllers are typically implemented with PWM, ensuring a fixed switching frequency. A known disadvantage of dead-beat controllers is the fact they rely on an accurate model and large gains. This means that model uncertainties and noise in measurements may significantly degrade the performance of the dead-beat controller, which can even lead to stability issues. Several dead-beat current control approaches have been proposed for SRMs (MIKAIL et al., 2012; MIKAIL et al., 2014; MA et al., 2019; MEHTA; HUSAIN; PRAMOD, 2019; PENG; EMADI, 2014; ZHANG et al., 2020; AHMAD; NARAYANAN, 2018; TAYLOR et al., 2020). An example block diagram for a dead-beat current controller is presented in Figure 1.14.

Figure 1.14 – Example block diagram for SRM dead-beat current controllers.



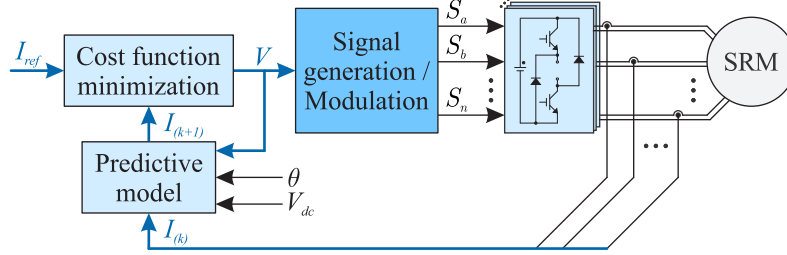
Source: Author.

In (MIKAIL et al., 2012) and (MIKAIL et al., 2014) a dead-beat predictive current controller is proposed. The proposal is capable of predicting the necessary duty cycle for the PWM pulses for any given reference current at every digital time step over the entire speed range. Similar proposals are also described in (MA et al., 2019) and (MEHTA; HUSAIN; PRAMOD, 2019), with the latter being applied to mutually coupled SRMs. Flux-based and back-EMF-based approaches are presented, where both make use of machine data, stored in the form of lookup tables. A dead-beat PWM controller is designed in (PENG; EMADI, 2014). The proposal makes use of the SRM model in order to achieve fast responses and accurate reference current tracking. As a means to deal with the SRM's nonlinear behavior and correct the model mismatch, a gain observer is introduced. In (AHMAD; NARAYANAN, 2018) a predictive dead-beat current controller is used in a current injection scheme for SRM characterization, avoiding traditional rotor-locking strategies. A deadbeat current control strategy with active thermal management is proposed in (ZHANG et al., 2020). The controller is used as an alternative to hysteresis. This enables lower switching frequencies, while still maintaining suitable performance. The frequency is dynamically adjusted based on the IGBT's temperature measurements, avoiding damage by overheating.

1.7.2.3 Model predictive current controller

Another class of predictive current controllers used for SRM current control are the model predictive controllers (MPC). This technique is characterized by the minimization of a cost function as a means to determine the control output. It can be divided in two different approaches: continuous control set (CCS), where a modulator determines the switching states based on the continuous output of the predictive controller, and finite control set (FCS), where the limited number of switching states are considered for solving the optimization problem (RODRIGUEZ et al., 2013). MPC methods present as advantages the use of an optimal control law and the possibility of including nonlinearities in the predictive model. On the other hand, MPC often presents increased computational complexity for systems with increased number of switching states. Moreover, the performance of the controller is affected by the quality of the model. Lastly, in the case of FCS-MPC, no modulator is used. This results in a variable switching frequency (OS-ÓRIO et al., 2017), which is not desirable for SRM current control applications, given the EMI related issues, for example. In this context, multiple contributions have been made regarding MPC applied to SRM current control (KIANI, 2014; LI; SHAMSI, 2015; LI; SHAMSI, 2016; MEHTA; KABIR; HUSAIN, 2018; VALENCIA et al., 2019; LI; SHAMSI, 2014; HU; GUO; YE, 2020). A model predictive current control structure for SRMs is depicted in Figure 1.15.

Figure 1.15 – Example block diagram for SRM model predictive current controllers.



Source: Author.

In (LI; SHAMSI, 2015), a model predictive current controller (MPCC) for SRMs is proposed. The proposal makes use of state estimators and model identification, in the form of an online inductance estimator, as a means to improve performance. Other advantages, such as delay compensation and a fixed switching frequency, are also observed. A similar approach is presented in (LI; SHAMSI, 2016), where an unconstrained MPCC is combined with an inductance auto-calibration mechanism, resulting in a stochastic MPCC with adaptive model calibration. A MPCC is described in (MEHTA; KABIR; HUSAIN, 2018), making use of a high accuracy lookup table (LUT) based on a semi-numerical machine model. In (VALENCIA et al., 2019) a virtual-flux FCS-MPCC for SRMs is proposed. The strategy uses flux-linkage tracking in order to indirectly control phase currents. A cost function is used to determine the switching signals that result in minimum error and, in order to reduce commutations and computational complexity, a state graph for switching states limitation is proposed.

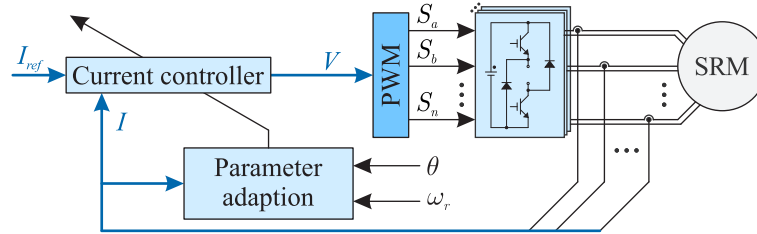
The use of MPCC has also been observed in other types of SRMs. In (LI; SHAMSI, 2014) an adaptive model predictive current controller for a double stator SRM (DSSRM) is proposed. The adaptive estimator is used as a way to cope with the time varying inductances of the DSSRM. In (HU; GUO; YE, 2020) FCS-MPCC is applied to the current control of a mutually coupled SRM (MCSRSM), as previous proposals for regular SRMs with AHB converters cannot be directly applied to MCSRSM.

1.7.2.4 Adaptive current controller

Another alternative to deal with the highly nonlinear behavior of SRMs is to dynamically adjust the controller gains. This allows the controller to be tuned online based on speed or load, for example, improving the dynamic responses and system stability. Such techniques also present as an advantage a fixed switching frequency, given they are implemented with PWM. It should be noted that adaptive controllers present cumbersome calculations, resulting in a more complex controller when compared to linear approaches,

for example. Some adaptive current control strategies have been proposed in literature (NAITOH; ISHIKAWA, 2010; MILASI; MOALLEM, 2014; PENG; YE; EMADI, 2016). The block diagram of an adaptive current controller for SRMs is presented in Figure 1.16.

Figure 1.16 – Example block diagram for SRM adaptive current controllers.



Source: Author.

In (NAITOH; ISHIKAWA, 2010) a model reference adaptive current controller is proposed. In this approach, a model with the desired characteristics, named reference model, is chosen. Such model is run in parallel with the closed loop system, where a gain adaptation mechanism is responsible for eliminating the difference between both outputs. An additional advantage of the proposal is the fact no SRM parameter lookup tables are required. A multi-loop self-tuning adaptive PI controller is presented in (MILASI; MOALLEM, 2014). First, a linearized model of the machine is considered. Then, the gains of the controllers are updated online as a function of the tracking errors, resulting in superior transient responses when compared to a fixed gain PI controller. Moreover, the controller presents a simple structure when compared to other nonlinear strategies.

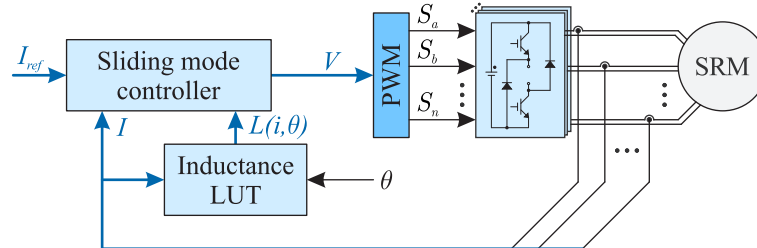
An adaptive digital PWM current controller is described in (PENG; YE; EMADI, 2016). Online gain adaptation is employed to deal with the model mismatch, ensuring both suitable dynamic responses and robustness to the algorithm. It takes full advantage of the SRM model information. Discrete-time analysis is presented, along with an improved sampling method to avoid the inherent PWM delay. The relationship of the proposal and other controllers is evaluated, showing it as an improved version of PI and dead-beat controllers.

1.7.2.5 Sliding mode current controller

Sliding mode algorithms have also been proposed as an alternative to address current control in SRM drives (MANOLAS; KALETSANOS; MANIAS, 2008; MANOLAS; PAPAFOOTIYOU; MANIAS, 2014; RUIWEI et al., 2014; YAO et al., 2010; YANG; ZHANG, 2005; YE; MALYSZ; EMADI, 2015; HU et al., 2019; HU; YE; VELNI, 2019; RAIN; HILAIRET; TALJ, 2010; SALEM et al., 2020). The technique is of interest mainly due to its robustness, necessary to deal with the nonlinear behavior of the machine. In addition,

due to PWM implementation, these techniques present a fixed switching frequency. Figure 1.17 presents the block diagram of a possible sliding mode control approach for SRM current control.

Figure 1.17 – Example block diagram for SRM sliding mode current controllers.



Source: Author.

In (MANOLAS; KALETSANOS; MANIAS, 2008) a sliding mode controller is presented. The proposal is further developed in (MANOLAS; PAPAFOITIOU; MANIAS, 2014), where a carrierless structure is used, with a state machine ensuring uniform converter switching. The controllers are inherently designed for digital implementation, given that they are based on the sliding mode control theory. In (RUIWEI et al., 2014) an adaptive sliding mode current controller is proposed. The design is carried out using a simple linear model, while the non-linear characteristics are considered as disturbances and uncertainties. Gain adaptation is employed as a means to improve the dynamic response and reduce chattering. An additional adaptive sliding mode strategy is presented in (YAO et al., 2010). A sliding mode-PI control approach is presented in (YANG; ZHANG, 2005). The combination of both techniques enables suitable reference tracking combined with robustness. An integral sliding mode current controller with constant switching frequency is proposed in (YE; MALYSZ; EMADI, 2015). The controller is designed considering a state space model with self and mutual inductances, where the stability analysis is presented for both known and bounded uncertain parameters situations. The proposal is evaluated for mutually coupled switched reluctance motors in (HU et al., 2019) and (HU; YE; VELNI, 2019), with the SRM being driven by an AHB and a three-phase voltage source inverter, respectively.

In practical applications, conventional sliding mode control strategies present chattering as a major drawback. Chattering is often referred to as a phenomenon of finite frequency and amplitude oscillations, resulting from sliding mode control. It is undesirable given it can lead to lower control accuracy and, on the SRM case, increased current ripple. Higher-order sliding modes are able to overcome this issue without significant compromises while maintaining a similar level of complexity. A second order sliding mode (SOSM) current controller is proposed in (RAIN; HILAIRET; TALJ, 2010), with gain design being carried out through successive tests. Experimental results show the robust

characteristics of the controller to phase inductance variations. More recently, in (SALEM et al., 2020) a SOSM controller is proposed. A comparative study is presented, with the SOSM controller presenting superior performance when compared to a traditional sliding mode approach, specially regarding the chattering phenomena.

1.7.3 Comparison of the current control strategies

The comparison of SRM current control strategies reported in literature is presented in Table 1.2. The previously discussed techniques are compared in terms of advantages, disadvantages, the use of model information (i.e. lookup tables), computational complexity and if fixed switching frequency is observed.

Table 1.2 – Summary and comparison of the SRM current control strategies.

Technique	Advantages	Disadvantages	Model dependence	Comput. complexity	Switching frequency
Hysteresis	Simplicity, robustness, fast dynamic response	Variable switching frequency, higher current ripple	No	Low	Variable
Intelligent	Over time adaptation, good for nonlinear problems	Slow learning process, need for training data	No	Medium	Variable / Fixed
Linear	Industry standard, simplicity	Not robust, poor fixed gain performance	Low	Low	Fixed
Dead-beat	Fast dynamic response, predictive	Sensitive to model uncertainties and noise	High	Medium	Fixed
MPC	Optimal control law, consideration of nonlinearities	Cumbersome calculations, no modulator (FCS), model dependent	High	High	Variable / Fixed
Adaptive	Robustness, online adaptation	Cumbersome calculations, complex structure	Medium	High	Fixed
Sliding mode	Robustness, fast dynamic response	Chattering	Medium	Medium	Fixed

Source: Author.

The traditional hysteresis controller is a simple model independent approach, however, it presents variable switching frequency and may present increased current ripple. Intelligent control is able to deal with the SRM nonlinearities, but requires data and extensive training. Linear control approaches are industry standard, but do not present the required robustness, often demanding gain adaptation or back-EMF compensation. Dead-beat controllers present predictive capabilities and fast dynamic response, however, are sensitive to model uncertainties and noisy measurements. In this sense, MPC presents an optimal control law and takes nonlinearities into consideration, at the cost of requiring cumbersome calculations. Adaptive techniques are robust and capable of online adaptation but often present complex calculations and a complex structure. Lastly, sliding mode approaches are capable of fast dynamic responses with a theoretical certificate of robustness. Chattering is a known drawback of the technique, which can be circumvented by adequate gain design, gain adaptation or the use of higher order sliding modes.

1.8 THESIS CONTRIBUTIONS

The contributions of this thesis, which aims to improve the performance of SRMs through advanced control strategies, are:

- Provide a PSO-based firing angle optimization strategy, taking into account torque ripple and copper losses. The optimal results are fitted for simple implementation in a microcontroller, avoiding lookup tables;
- Develop a discrete-time super-twisting sliding mode robust current control approach, capable of dealing with the high non-linearity of the machine. The algorithm is implemented using PWM, ensuring a fixed switching frequency. In addition, the proposal exhibits improved reference tracking performance;
- Provide a stability analysis of the proposed current controller, including the digital implementation delay;
- Develop a gain design methodology for super-twisting controllers;

1.9 THESIS STRUCTURE

The following thesis is divided into 5 chapters, presented as follows.

Chapter 2 presents the SRM working principles as well as the mathematical modeling of the machine. The operation under current control as well as the static converter used are shown. A simulation model on Matlab/Simulink, based on lookup tables containing machine magnetization data, is also discussed.

Chapter 3 presents a firing angle optimization procedure based on the particle swarm optimization algorithm. The proposal aims to ensure performance with a balance between reduced torque ripple and high energy efficiency. In order to avoid the use of lookup tables in digital implementation, the effect of mechanical load variation is disregarded. A conventional fine grid optimization approach is presented and then an alternative is proposed, making use of the PSO algorithm. Simulation results and experimental results are conducted in order to validate the proposal.

A robust current control approach based on a discrete-time super-twisting sliding mode algorithm is described in Chapter 4. The stability analysis of the controller is presented, taking the one sample implementation delay into account. Moreover, a methodology for choosing the controller gains is presented, using an optimization-based design. Lastly, gain adaptation is performed, aiming to improve the performance of the controller. Experimental results making use of a TSF strategy are provided to demonstrate the effectiveness of the proposed current controller, where a conventional hysteresis controller is used for comparison in terms of sampling frequencies, computational complexity, current and torque root-mean-square-errors.

Finally, Chapter 5 contains some conclusions and prospects for future work. Lastly, the publications produced during this period are also listed.

Appendix A presents a procedure for mechanical parameter estimation using a PSO algorithm. A robust speed controller by means of linear matrix inequalities is presented in Appendix B. Appendix C shows a detailed description of the experimental setup.

2 SWITCHED RELUCTANCE MACHINE FUNDAMENTALS

2.1 INTRODUCTION

In the last couple of decades, research related to the design and control of SRMs has grown significantly. Due to its constructive characteristics and high robustness, the machine presents itself as a strong candidate for use in electric vehicle and more electric aircraft applications (BILGIN et al., 2020; SAYED et al., 2021). In addition, the continuous developments in power electronics, the lower costs of semiconductor devices and the increase in processing power of microprocessors has been accelerating this process.

In this chapter, the constructive characteristics of the switched reluctance machine will be presented, where the double salient structure and the machine's inductance profile are shown.

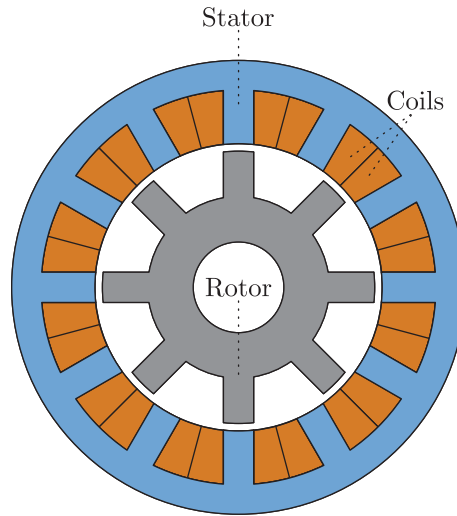
The drive required to operate the machine as a motor is presented and the stages of the static converter are analyzed. Two different techniques are presented for operating the motor at low and high speeds. Lastly, the modeling of the machine is presented, showing the electrical and mechanical dynamic equations. The model obtained is discussed, presenting the method for obtaining the simulation data, composed by the current and torque lookup tables.

2.2 SWITCHED RELUCTANCE MACHINE CHARACTERISTICS

The SRM has a very simple construction when compared to other electric machines on the market, given that it presents a double salient structure. Its excitation is provided by concentrated independent windings, mounted in the stator slots. In turn, the rotor is composed of a series of laminated electrical steel pieces stacked together. That eliminates the need for rotor windings or the use of permanent magnets, lowering the production cost of the machine (BILGIN; JIANG; EMADI, 2019).

The most commonly used structures for SRMs have symmetrical and equally spaced poles. The most common three-phase configurations have either one pair of poles per phase (6 poles in the stator and 4 poles in the rotor, 6/4) or two pairs of poles per phase (12 poles in the stator and 8 poles in the rotor, 12/8). However, machines with a greater number of phases are also presented in literature, such as the 8/6 machine, which has four phases and a pair of poles per phase (MILLER, 2002). One of the machines used in this thesis has a 12/8 structure, as shown in Figure 2.1.

Figure 2.1 – Cross section of a 12/8 SRM, with the coils, rotor and stator highlighted.



Source: Author.

The SRM usually has an even number of rotor and stator poles to ensure the magnetic duality needed to create a flux path. When the poles of the rotor and stator align, a path of minimal reluctance is formed. For motoring operation, the number of poles on the rotor and stator must be different. Thus, it is possible to improve the existence of starting torque for any given rotor position, considering that the stator poles of one of the machine's phases will always be out of alignment with the rotor poles. Note that other aspects, such as the rotor geometry, also affects the starting capability at any rotor position (BILGIN; JIANG; EMADI, 2019).

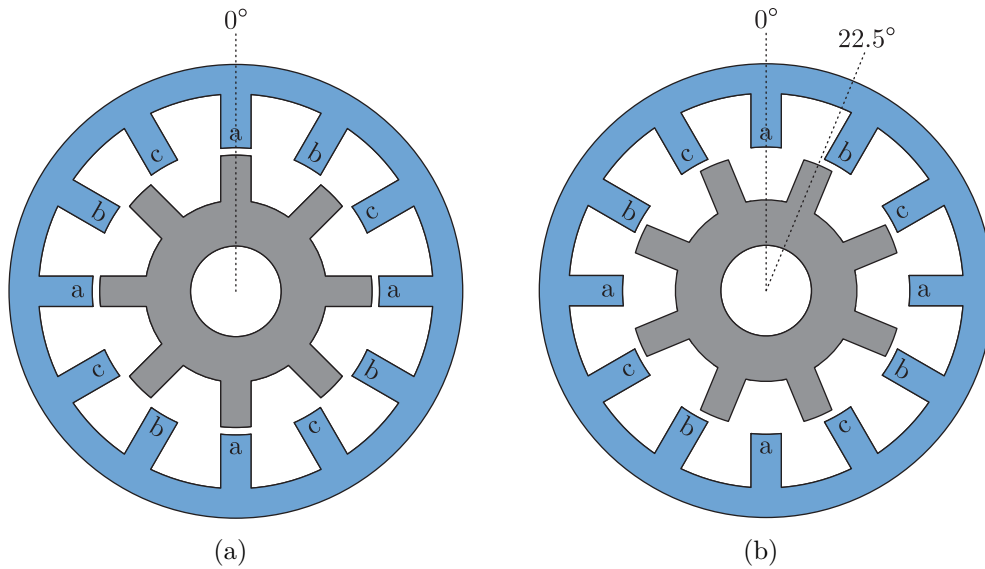
The pole configuration of the machine is highly linked to its application. For motor operation, a greater number of phases helps to mitigate electromagnetic torque ripple. Moreover, it also contributes to the system robustness, given that it presents a greater fault tolerance, a desirable characteristic in electric vehicle applications, for example (KRISHNAMURTHY et al., 2006; BILGIN et al., 2020). With a higher number of phases, however, the space available for windings within the stator slots of the machine becomes more restrict. In addition, a greater number of phases raises complexity and the overall cost of the system, given a more complex converter will be required to drive the machine (BOLDEA et al., 2014).

2.3 INDUCTANCE PROFILE

The phase inductance in SRMs is dependent on the rotor position, with the aligned and unaligned positions being the more relevant. In the aligned position, when a pair of rotor poles are aligned with a pair of stator poles, the magnetic circuit has minimal reluctance and, therefore, the equivalent circuit has maximum inductance. In the unaligned

position, when a pair of rotor poles is at the point of greatest misalignment with a pair of stator poles, the magnetic circuit has maximum reluctance and, therefore, the equivalent circuit has minimum inductance. These positions are shown in Figure 2.2.

Figure 2.2 – Rotor positions of the SRM in relation to phase a. (a) Aligned position. (b) Unaligned position.



Source: Author.

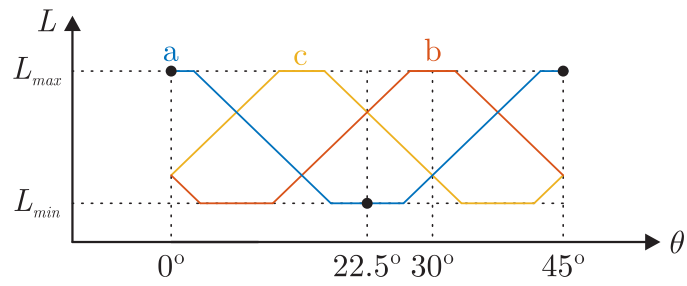
The periodic variation characteristic of the machine's inductance with respect to the rotor position is known as the inductance profile. The profile period is a function of the number of rotor poles of the machine, while the phase shift between phases is a function of the number of stator poles and the number of phases.

Considering the 12/8 machine, a period of 45° for the inductance profile and a phase shift of 15° are observed. Assuming the initial position of 0° as the aligned position of phase "a", a theoretical inductance profile of the machine can be plotted as seen in Figure 2.3. It should be noted that the profile does not have the presented shape, however, the approximation is often used for representation purposes.

In Figure 2.4 it is possible to see a cross section of the machine at three different positions, aligned with phases "a", "c" and "b", respectively. A phase shift of 15° can also be observed. Lastly, it is also noted that the cycle starts again after the sequence is finished, with phase "a" as the next phase to reach the alignment position.

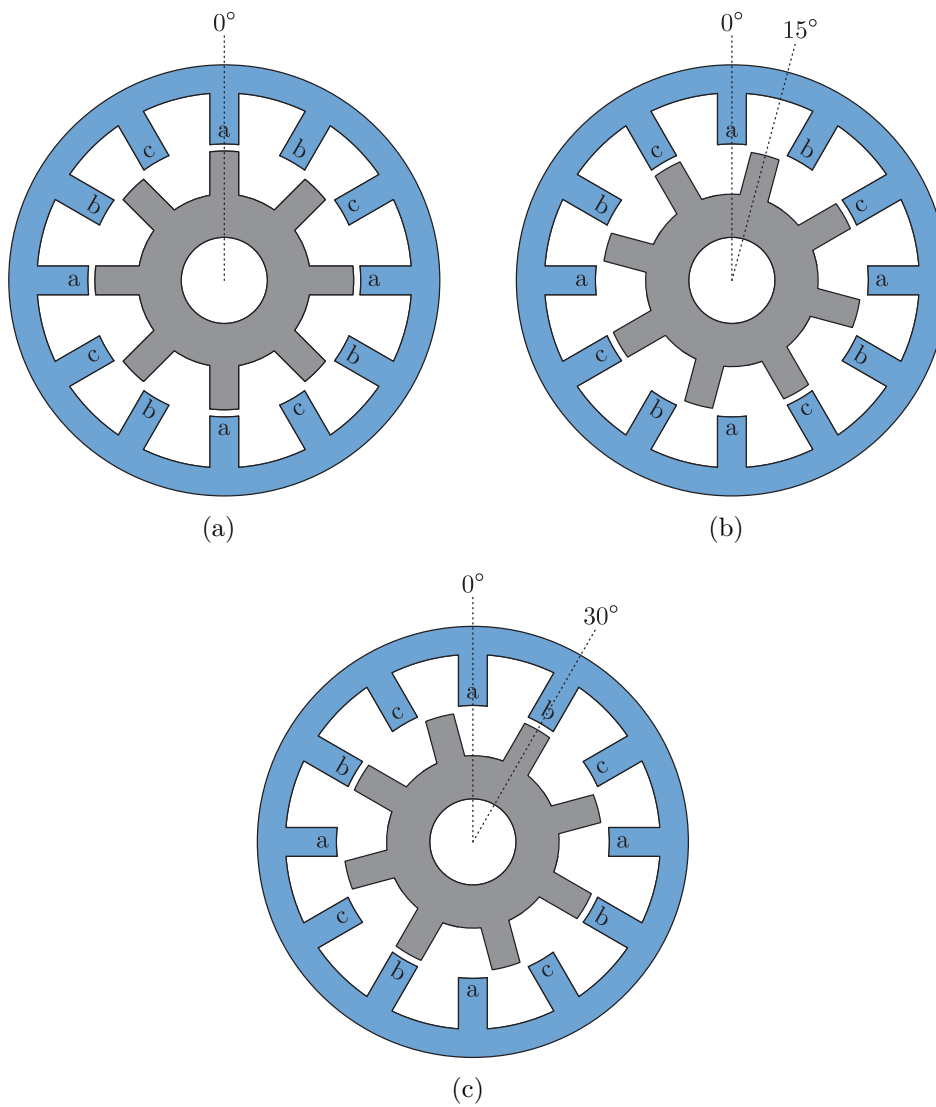
For the proper operation of the control system, the rotor position obtained from the SRM is referred to each phase, in order to obtain the relative positions of each phase. This process is done taking into account the phase shift of the machine. The relative positions can be obtained according to the expressions seen in equations (2.1), (2.2) and (2.3).

Figure 2.3 – Theoretical inductance profile for a 12/8 SRM.



Source: Author.

Figure 2.4 – SRM aligned positions in relation to each phase. (a) Phase a. (b) Phase c. (c) Phase b.



Source: Author.

$$\theta_a = \left(\frac{\theta}{45^\circ} - \alpha \right) \cdot 45^\circ \quad (2.1)$$

$$\theta_b = \theta_a - 15^\circ \quad (2.2)$$

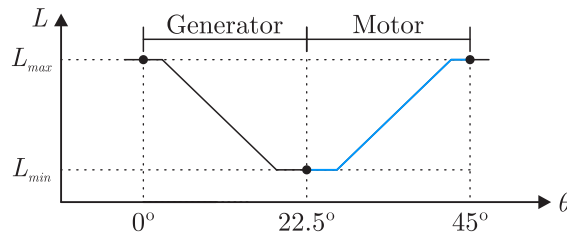
$$\theta_c = \theta_a - 30^\circ \quad (2.3)$$

where α is the lower integer of the division of $\theta/45^\circ$, θ_a is the relative position of phase “a”, θ_b is the relative position of phase “b”, θ_c is the relative position of phase “c” and θ is the rotor position. Note that θ is obtained through an encoder, attached to the machine shaft, while the phase positions are calculated based on this measurement inside the microcontroller, for example.

2.4 SWITCHED RELUCTANCE MACHINE OPERATION

The operation of a switched reluctance machine is directly connected to the firing angles, which will determine the operation as a motor or generator. The firing angles determine angles at which the excitation will start and end, defined as θ_{on} and θ_{off} , respectively. For the 12/8 machine, and considering the position of 0° as the position where a pair of rotor poles are aligned with a pair of stator poles, the machine’s operating region can be drawn on top of the inductance profile, as a function of the firing angles, as seen in the Figure 2.5. By operating in the inductance decrease interval, between 0° and 22.5° , the machine will operate as a generator, while operating in the inductance increase interval, between 22.5° and 45° , the machine will operate as a motor.

Figure 2.5 – Inductance profile of a 12/8 machine with operating regions highlighted (generator and motor).

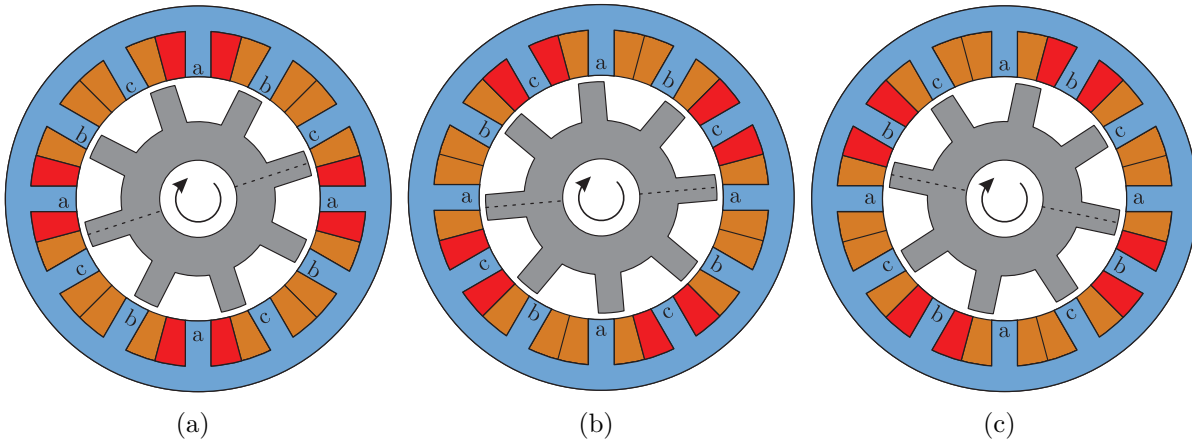


Source: Author.

2.4.1 Phase excitation

By promoting the excitation of a phase of the SRM, the rotor has a natural tendency to align itself with the stator poles, seeking an equilibrium position, due to the phenomenon of magnetic reluctance. For motoring operation, phase excitation must be carried out sequentially, making the rotor continually seek a new equilibrium position. Thus, it is noted that the operation as a motor continuously attempts to minimize reluctance, that is, it always aims to maximize the inductance of the circuit. Figure 2.6 illustrates the motor operation, where a phase is excited whenever it is in the positive slope of the inductance profile. Once a phase is near alignment, its excitation ends and the next phase in will be excited. It can be seen that in Figure 2.6 (a) phase “a” is being excited. Once it is near the aligned position, it is turned off and phase “c” begins excitation, as seen in Figure 2.6 (b). Once again, when phase “c” is near the aligned position, it is turned off and phase “b” is excited, as seen in Figure 2.6 (c).

Figure 2.6 – Sequential phase excitation for motor operation. (a) Phase a. (b) Phase c. (c) Phase b.



Source: Author.

For proper operation, a static converter and a closed loop control system are necessary, as will be presented in the following sections. In addition, variables such as the firing angles significantly affect the performance of the motor, as it will be shown in Chapter 3.

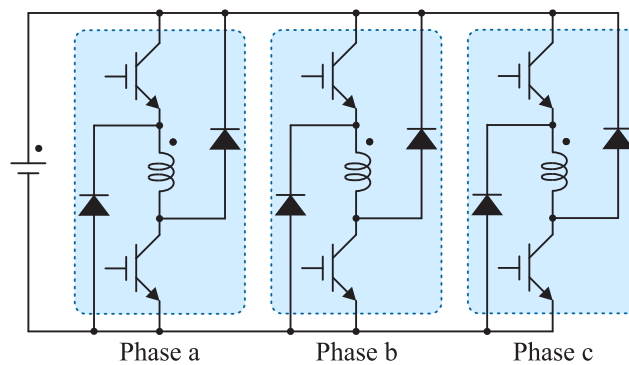
2.4.2 Asymmetric half-bridge converter

For operation, either as a motor or as a generator, the switched reluctance machine requires the use of a static converter. The drive must be able to excite the phases individually and at the correct moment, which demonstrates the importance of the rotor

position during operation. In addition, the converter needs a power supply, in order to provide the necessary energy to drive the machine, when operating as a motor, or to provide the initial excitation, when operating as a generator.

The Asymmetric Half-Bridge converter (AHB) is the most common topology used for driving switched reluctance machines. In this topology, two legs containing a switch and a diode each are connected to each phase of the machine, as seen in Figure 2.7. This configuration is very popular due to its flexibility as it allows the machine to operate as a motor or generator, with minimal changes in the converter circuit, such as the addition of a battery and a protection diode.

Figure 2.7 – Three-phase AHB converter.

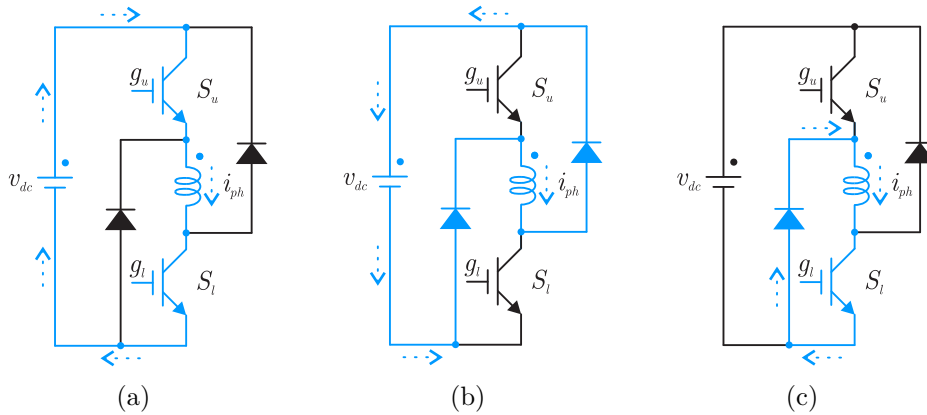


Source: Author.

By neglecting mutual coupling between phases, it is possible to analyze the operational stages of the converter separately, as seen in Figure 2.8. The first stage of operation happens when both of the switches are closed and the diodes are blocked, as presented in Figure 2.8 (a). DC-link voltage is supplied to the phase, causing current to rise while the switches remain turned on, characterizing the process of magnetization. When the switches are turned off, the energy stored in the winding causes the diodes to be forward biased, offering a new path for the current to flow. This initiates the second stage of operation, as presented in Figure 2.8 (b). Negative DC-link voltage is supplied to the phase, decreasing phase current and de-magnetizing the winding. The diodes remain in conduction until the switches are turned on again or until phase current reaches zero. A third stage can be used, where only one switch is kept on and the other switch is turned off, as presented in Figure 2.8 (c). Note that either the upper or lower switch can be used. This stage is known as freewheeling stage, because the current flows only through the phase, a switch and a diode, with zero voltage being applied to the winding.

Current control, also known as chopping, can be implemented using different stages of the AHB converter. Literature defines hard chopping when positive and negative voltage levels are used for current control, while soft chopping makes use of only positive and zero voltage levels (CHOI; AHN; LEE, 2005; BILGIN; JIANG; EMADI, 2019).

Figure 2.8 – Operational stages of the AHB converter. (a) Magnetization. (b) Demagnetization. (c) Freewheeling.



Source: Author.

It can be noted that the topology presents a unidirectional current flow, regardless of the operational stage of the converter. From a voltage standpoint, however, a bidirectional behavior is observed, given that the voltage applied to the winding changes depending of the stage of operation (MILLER, 2001).

This converter topology also enables the machine to operate under a fault condition, since it allows the control of each phase individually. The main disadvantage of this converter, however, is associated with the greater number of devices per phase, when compared to other topologies. The increased number of switches contributes to a higher overall cost of the drive, as well as to the increase in conduction and switching losses, given two devices are always in series with the excited phase (BARNES; POLLOCK, 1998).

2.5 SWITCHED RELUCTANCE MOTOR CONTROL

For variable speed operation, the SRM must be excited based on a reference generated from an external loop controller, such as a speed or torque regulator. Machine excitation can be varied in a few different ways. For low speed operation, the back-EMF is small, so it is possible to control phase currents to a desired value. With the increase in speed, however, current control starts to be degraded due to DC bus voltage limitations. The base speed concept determines the speed above which effective current control cannot be achieved due to high back-EMF. More details will be provided in the following section, where the SRM dynamic model will be presented. Thus, for operations at high speeds, only firing angles control is performed, also known as single pulse control.

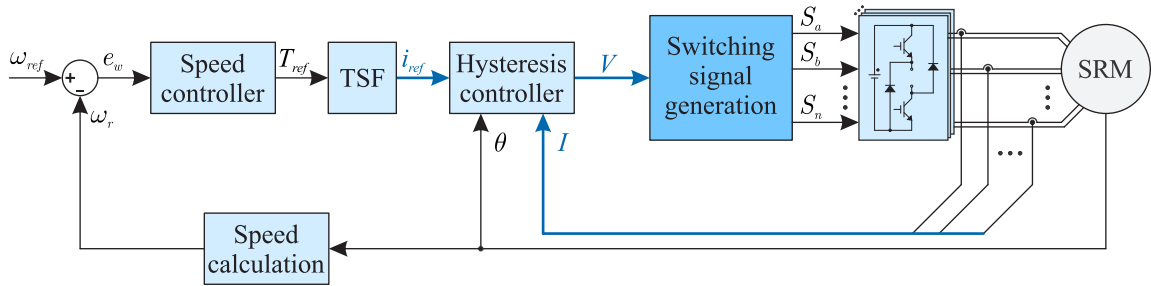
Control strategies are usually analyzed by phase, since the system can be considered decoupled for control purposes. To implement such techniques, identical controllers are

used, one for each phase, and each controller is fed back with the corresponding relative phase position. Current and single pulse control will be further explored in the following subsections. This thesis will focus on the current control below base speed, which will be further explored in the following chapters.

2.5.1 Current control

As previously mentioned, for operation below base speed, current control is used. Current control can be done in several ways, however, due to the high non-linear behavior of the SRM, hysteresis current control is often used. Hysteresis control requires the existence of an external control loop, responsible for the generation of a reference current, i_{ref} , based on a speed or torque error. The block diagram can be seen in Figure 2.9. It shows that all phase currents are measured and, depending on the relative phase position, are compared with the reference current, so that the hysteresis process can be carried out. The hysteresis band is previously defined and by comparing the current error with the limits of this band, the states of AHB converter switches are determined.

Figure 2.9 – Block diagram for hysteresis current control.



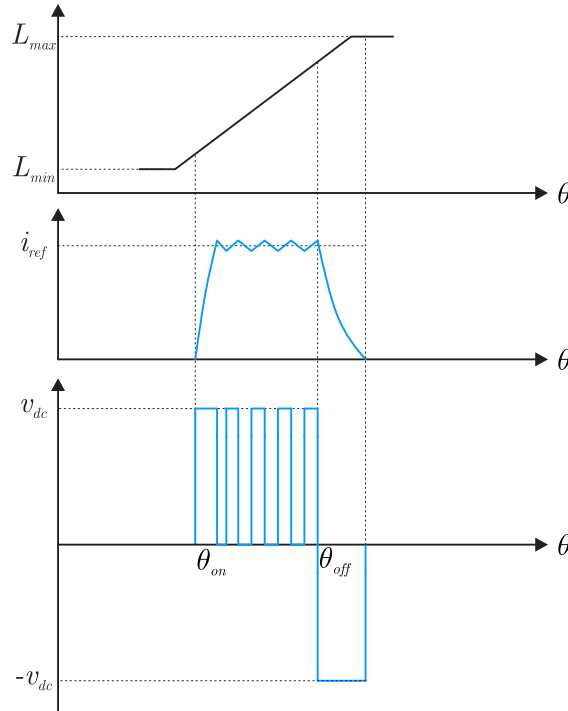
Source: Author.

Phase position is measured and verified to see if it is inside the excitation interval, that is, if any of the phases is in the inductance increase interval. This process is done by comparing the phase angle with the firing angles θ_{on} and θ_{off} . If any of the phases are between these angles, a reference current will be provided and phase excitation will occur. For phases that are outside this interval, no reference current will be given, keeping the switches of these phases turned off.

The hysteresis control procedure can be seen in Figure 2.10. Initially, when the relative position of a given phase satisfies the condition $\theta_{ph} \geq \theta_{on}$, the reference current becomes greater than zero. The converter's switches will then be turned on, causing the phase current to rise. Note that while the switches are on, the voltage across the phase is equal to the supply voltage. Once the current value reaches the upper limit of the hysteresis band, one of the switches is turned off. At this moment, one diode is forward

biased, offering a new path for current to flow. Then, phase current starts to decrease, until the lower limit of the hysteresis band is reached, where the switches are once again turned on. The process is repeated until $\theta_{ph} > \theta_{off}$ is satisfied, where both switches will be turned off and the current will decrease until it reaches zero. The switches remain open until the phase position reaches the excitation interval again.

Figure 2.10 – Inductance, current and voltage waveforms for hysteresis current control.



Fonte: Autor.

Hysteresis current control is of interest as it can be applied to the SRM without knowledge of the machine's electrical parameters. In addition, the hysteresis regulator is highly robust, given it is immune to parametric variations. This technique, however, has some disadvantages. Variable switching frequency becomes a problem, since throughout the control interval the frequency with which current reaches the hysteresis bands varies (YE; MALYSZ; EMADI, 2015; AHMAD; NARAYANAN, 2016). This can make EMI design a more complex task, for example. Another problem verified is the often higher current ripple of this technique, which directly affects torque ripple.

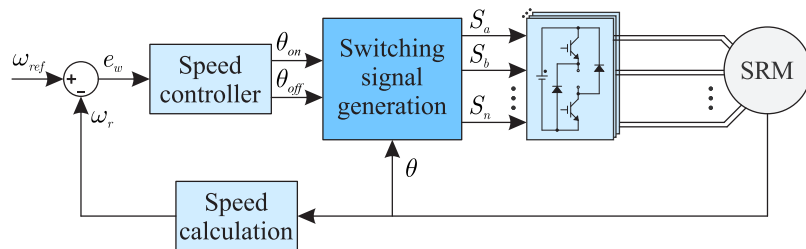
Alternatively, PWM current control techniques can be used to mitigate some of the problems previously mentioned, such as a variable switching frequency. However, the algorithms used must be robust to the non-linearities of the machine. This will be further explored in Chapter 4.

As previously mentioned, current control can be implemented using different stages of the AHB converter. This thesis makes use of both soft and hard chopping techniques.

2.5.2 Single pulse control

As previously mentioned, for operation above the base speed, current control is not viable given the voltage limitations of the drive. As a result, single pulse control is used. This technique makes use of only a single pulse in the excitation interval, where control is performed by varying the excitation interval, θ_{on} and θ_{off} . The firing angles directly impact the machine dynamics, as well as the phase current value. Note that the peak current value cannot be controlled with single pulse control. The block diagram of the single pulse control can be seen in Figure 2.11.

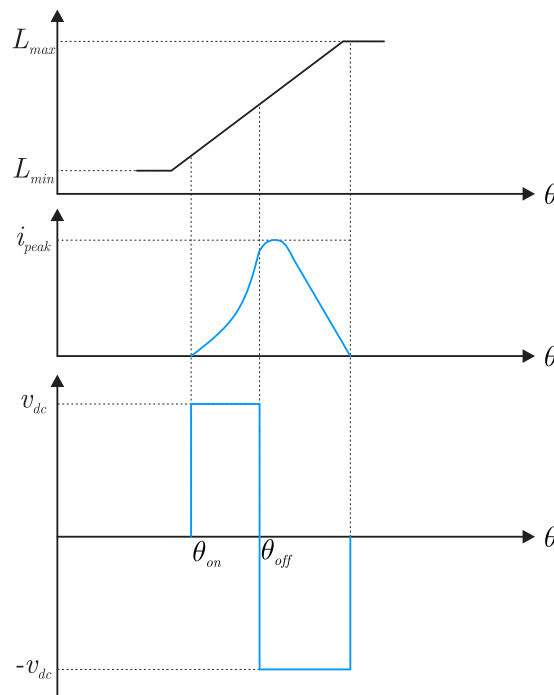
Figure 2.11 – Block diagram for single pulse control.



Source: Author.

The waveforms of the single pulse control can be seen in Figure 2.12.

Figure 2.12 – Inductance, current and voltage waveforms for single pulse control.



Source: Author.

In this configuration, the firing angles are determined through a controller based on a speed or torque tracking error. The switches of the AHB converter are controlled according to a simple switching logic, which turns them on while the condition $\theta_{on} \leq \theta_{ph} \leq \theta_{off}$ is satisfied. Note that while the position of a given phase is in the excitation interval, phase current increases, until θ_{off} is reached, where the switches are turned off and the current starts to decrease until reaching zero.

2.6 MODELING

In this section both the electrical and mechanical models of the SRM are presented, in order to express the dynamic behavior of the machine. The dependence of certain variables in relation to the rotor position, and the magnetic saturation are also considered.

2.6.1 Electrical model

In an SRM phase voltage is given by

$$v = Ri + \frac{d\phi}{dt}, \quad (2.4)$$

where ϕ is the flux linkage and R is the stator winding resistance. Magnetic saturation can be taken into account, with the flux linkage becoming a function of both current and rotor position (θ). Therefore, flux linkage can be defined as:

$$\phi(i, \theta) = L(i, \theta)i(t). \quad (2.5)$$

Replacing (2.5) in (2.4) and calculating its derivative, results

$$v = Ri + L(\theta, i)\frac{di}{dt} + i\frac{dL(\theta, i)}{dt}. \quad (2.6)$$

Expanding the derivative of the inductance in relation to time, results:

$$\frac{dL(\theta, i)}{dt} = \frac{\partial L(\theta, i)}{\partial \theta} \frac{d\theta}{dt} + \frac{\partial L(\theta, i)}{\partial i} \frac{di}{dt}. \quad (2.7)$$

By replacing (2.7) in (2.6) and rearranging the terms results (2.8).

$$v = Ri + l(\theta, i)\frac{di}{dt} + \epsilon \quad (2.8)$$

where

$$l(\theta, i) = L(\theta, i)\frac{di}{dt} + i\frac{\partial L(\theta, i)}{\partial i} \quad (2.9)$$

$$\epsilon = i\omega_r \frac{\partial L(\theta, i)}{\partial \theta} \quad (2.10)$$

$$\omega_r = \frac{d\theta}{dt} \quad (2.11)$$

The first term, $l(\theta, i)$, is referred to as incremental inductance (SALMASI; FAHIMI, 2004; GAO; SALMASI; EHSANI, 2004; YE; BILGIN; EMADI, 2015a). It accounts for the effects of magnetic saturation, by considering current, self-inductance $L(\theta, i)$ and the inductance variation caused by current. The term ϵ corresponds to the machine's back-EMF.

Equation (2.8) can be represented in a matrix form, as seen in (2.12)

$$\begin{bmatrix} v_a \\ v_b \\ v_c \end{bmatrix} = \begin{bmatrix} R_a + \omega_r \frac{\partial L_a}{\partial \theta} & 0 & 0 \\ 0 & R_b + \omega_r \frac{\partial L_b}{\partial \theta} & 0 \\ 0 & 0 & R_c + \omega_r \frac{\partial L_c}{\partial \theta} \end{bmatrix} \begin{bmatrix} i_a \\ i_b \\ i_c \end{bmatrix} + \begin{bmatrix} l_a & 0 & 0 \\ 0 & l_b & 0 \\ 0 & 0 & l_c \end{bmatrix} \frac{d}{dt} \begin{bmatrix} i_a \\ i_b \\ i_c \end{bmatrix} \quad (2.12)$$

where v_a , v_b and v_c are the phase voltages; R_a , R_b and R_c are the phase resistances; L_a , L_b and L_c are the phase self-inductances; l_a , l_b and l_c are the incremental inductances and i_a , i_b and i_c are the phase currents.

Equation (2.7) can be rewritten neglecting saturation effects. In this case, the behavior of the flux linkage in relation to current is said to be linear, with inductance becoming a function of rotor position exclusively and constant in relation to the current, as seen below.

$$\frac{dL(\theta, i)}{dt} = \frac{dL(\theta)}{dt} = \frac{\partial L(\theta)}{\partial \theta} \frac{d\theta}{dt} \quad (2.13)$$

Thus, phase voltage can be written as a function of $L(\theta)$, as seen in (2.14).

$$v = Ri + L(\theta) \frac{di}{dt} + i\omega_r \frac{\partial L(\theta)}{\partial \theta} \quad (2.14)$$

2.6.2 Torque

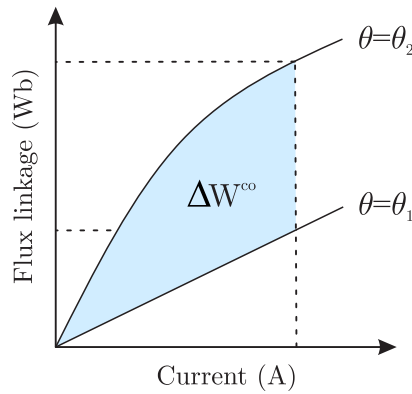
Electromagnetic torque modeling will be done in two stages: non-linear analysis, where the effects of magnetic saturation are taken into account, and linear analysis, where the saturation effects are neglected, in order to simplify the overall analysis.

2.6.2.1 Non-linear analysis

During operation, switched reluctance machines operate far from a linear magnetic region. Thus, in order to correctly model the electromechanical energy conversion process, an analysis taking into account the non-linearities of the system must be performed. To consider the saturation of the machine's magnetic circuit, the magnetization characteristics of the SRM must be taken into account, that is, the magnetization curves that relate the flux linkage behavior as a function of the current and rotor position (MILLER, 2001).

Figure 2.13 shows the magnetization characteristics for a situation where magnetic saturation is observed, with ΔW^{co} representing the variation of co-energy. Energy is defined as the integral of the current in relation to flux linkage. Co-energy, in turn, is defined as the integral of flux linkage in relation to current, as seen in (2.15) (KRISHNAN, 2001; MILLER, 2001).

Figure 2.13 – Variation of co-energy with position for a given current value.



Source: Author.

$$W_j^{co} = \int_0^i \phi(\theta, i) di, \quad (2.15)$$

where j refers to a machine phase, with $j \in N$ and $1 \leq j \leq 3$, considering a three-phase 12/8 machine, for example. The total co-energy is given by the sum of the co-energy of each phase, as seen in (2.16).

$$W^{co} = \sum_{j=1}^3 W_j^{co}(i, \theta) \quad (2.16)$$

Thus, for a given current value, the electromagnetic torque value can be determined by the rate of change of co-energy in relation to position, as seen in the equation (2.17).

$$T_e = \frac{\partial W^{co}}{\partial \theta} \quad (2.17)$$

2.6.2.2 Linear analysis

In order to perform a simplified analysis, the electromagnetic torque can be derived from the input power, using a linear approach (MILLER, 2001). The instantaneous input power, p_{in} , can be obtained by multiplying the machine voltage equation, (2.6), by current, as seen below.

$$p_{in} = vi = Ri^2 + i^2 \frac{dL(\theta)}{dt} + L(\theta)i \frac{di}{dt} \quad (2.18)$$

Since the rate of change of stored magnetic energy is given by

$$\frac{d[L(\theta)i^2]}{dt} = 2L(\theta)i \frac{di}{dt} + \frac{dL(\theta)}{dt} i^2, \quad (2.19)$$

one can isolate the term

$$L(\theta)i \frac{di}{dt} = \frac{d\left[\frac{1}{2}L(\theta)i^2\right]}{dt} - \frac{1}{2} \frac{dL(\theta)}{dt} i^2. \quad (2.20)$$

Replacing the term $L(\theta)i \frac{di}{dt}$, from equation (2.18), by (2.20) results

$$p_{in} = Ri^2 + \frac{d\left[\frac{1}{2}L(\theta)i^2\right]}{dt} + \frac{1}{2} \frac{dL(\theta)}{dt} i^2. \quad (2.21)$$

Since saturation is neglected in this analysis, it is possible to replace the derivative of inductance in (2.21), $\frac{dL(\theta)}{dt}$, with the one shown in (2.13). Therefore, the input power can be rewritten as

$$p_{in} = Ri^2 + \frac{d\left[\frac{1}{2}L(\theta)i^2\right]}{dt} + \frac{1}{2}i^2 \frac{\partial L(\theta)}{\partial \theta} \omega_r. \quad (2.22)$$

In equation (2.22) the instantaneous input power can be divided into three terms. The first term consists of copper losses in the winding. The second term represents the rate of change of the energy stored in the magnetic field and, according to the law of conservation of energy, the last term represents the power in the air gap. Since the air gap power is the product of the electromagnetic torque by the rotor speed,

$$p_g = T_e \omega_r, \quad (2.23)$$

the electromagnetic torque of the machine, ignoring the saturation effects, can be expressed as

$$T_e = \frac{1}{2}i^2 \frac{\partial L(\theta)}{\partial \theta}. \quad (2.24)$$

Once more, it is noted that the torque of the SRM has a non-linear characteristic by nature, given the varying inductance term observed in equation (2.24).

2.6.3 Mechanical model

Considering the operation as a motor, the dynamic equation of a rotating machine can be defined as

$$\dot{\omega}_r = -\frac{B}{J}\omega_r + \frac{1}{J}T_m, \quad (2.25)$$

where B is the friction coefficient and J is the rotor moment of inertia. The parameter values are estimated by the procedure described in Appendix A. Mechanical torque can be defined as

$$T_m = T_e - T_L, \quad (2.26)$$

where T_L is the load torque applied to the machine shaft.

Using the linear model, where saturation is neglected, mechanical torque can be determined by replacing equation (2.14) in (2.25). The resulting torque expression can be seen in (2.27).

$$T_m = -\frac{1}{2}i^2 \frac{dL(\theta, i)}{d\theta} + B\omega_r + J \frac{d\omega_r}{dt} \quad (2.27)$$

2.7 SIMULINK MODEL

Due to the non-linear behavior of the SRM, machine magnetization data is often used to build a simulation model. The use of finite element analysis is frequently mentioned in literature as an alternative to capturing the machine's flux linkage and torque characteristics. However, physical dimensions of the machine are required for this method, which can be a problem when they are not provided by the manufacturer. Another alternative is through experimental tests, which can provide more reliable magnetization data of the machine. The procedure used for building this model is presented in (BARROS et al., 2018) and was originally done for this specific machine in (OSÓRIO, 2017).

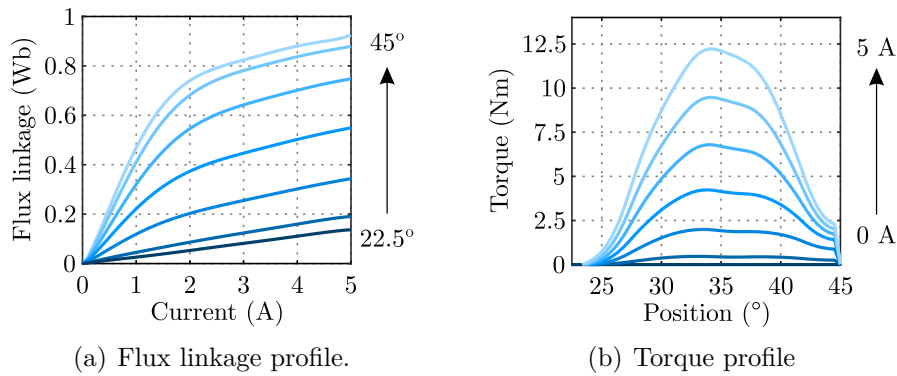
In order to obtain the magnetization data, the rotor of the machine must be placed in known positions while a voltage step is applied. With current and voltage data for different positions, the flux values can be calculated using equation (2.28), and later extended for smaller current values through polynomial regression (BARROS et al., 2018).

$$\phi(t) = \int_0^t (v - Ri) dt \quad (2.28)$$

For this Thesis, two different SRMs are used. Figure 2.14 shows the flux linkage and torque profiles of the studied 12/8 SRM (SRM 1), while Figure 2.15 shows the same

profiles for the studied 8/6 SRM (SRM 2). The effect of saturation can be observed in several of the curves, becoming more evident the closer the rotor is to the aligned position. Moreover, note that for SRM 2, FEA data is available, being obtained through JMAG software. For further detail, please refer to (LI, 2017).

Figure 2.14 – Characteristics of the 12/8 studied SRM.



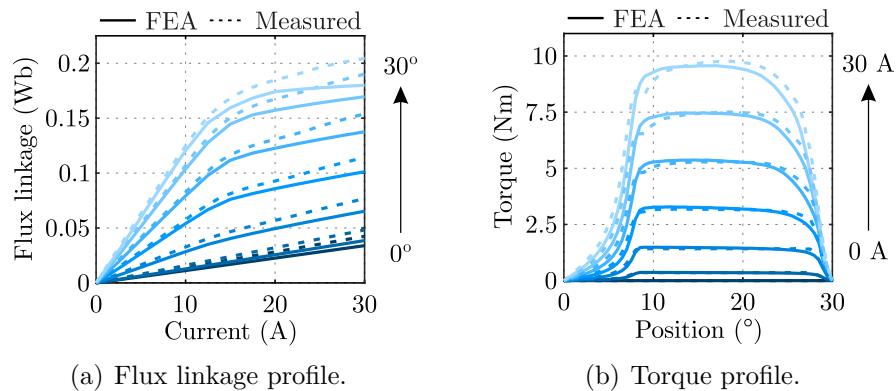
Source: Author.

Table 2.1 – Parameters of the 12/8 studied SRM.

Parameter	Value
Rated speed	1500 r/min
Rated power	2 kW
Rated torque	12 Nm
Rated voltage	400 V
Rated current (Phase RMS value)	5 A
Number of phases	3

Source: Author.

Figure 2.15 – Characteristics of the 8/6 studied SRM.



Source: Author.

Table 2.2 – Parameters of the 8/6 studied SRM.

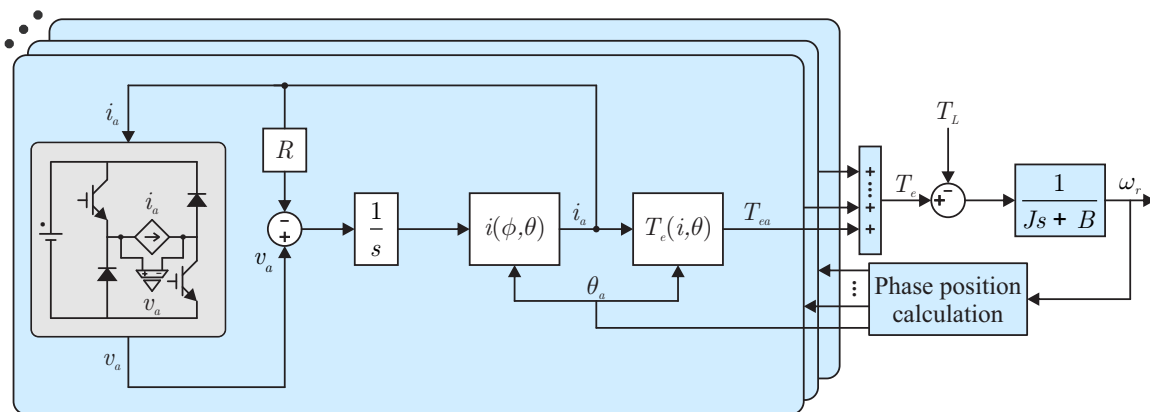
Parameter	Value
Rated speed	6000 r/min
Rated power	5.1 kW
Rated torque	8 Nm
Rated voltage	300 V
Rated current (Phase RMS value)	14.35 A
Number of phases	4

Source: Author.

Using the data from Figures 2.14 and 2.15 it is possible to build a current lookup table, $i(\phi, \theta)$, which returns the current value based on the flux linkage and rotor position, and a torque lookup table, $T_e(i, \theta)$, which return the torque value based on the current and rotor position.

A simulation model is built in Matlab/Simulink, using both lookup tables, as shown in Figure 2.16. The simulation process starts with the state of the converter switches. The phase current and voltage are then measured, allowing the flux linkage to be calculated. With the flux linkage value and the rotor position of the machine, it is possible to find the phase current value through the current table. With the new current value and still using the rotor position, the torque table is used in order to determine the electromagnetic torque value. This procedure is carried out for all of the phases of the machine, simultaneously. The total torque value is then obtained by adding the torque produced by each phase and, using the equation (2.25), the rotor speed of the SRM can be determined. The rotor position can be determined by integrating the rotor speed. Lastly, using the rotor position, the phase referred positions are calculated, including the 15° phase shift.

Figure 2.16 – Block diagram of the Simulink simulation model.



Source: Author.

2.8 CONCLUSIONS

In this chapter, the basic concepts related to the operation of SRM were presented. The constructive characteristics of SRM were shown, focusing on the double salient structure, as well as on the machine's inductance profile. The converter used to drive the machine was presented, where its operating stages were analyzed, showing how they affect the machine during motoring operation. In addition, the SRM control techniques were analyzed, focusing on two strategies: current and single pulse control. The electrical and mechanical modeling of the machine are presented, along with the simulation model, where lookup tables are used to represent the dynamic behavior of the machine. The firing angle optimization as well as the design of robust fixed switching frequency current controllers will be carried out in the following Chapters and will make use of these models.

3 PARTICLE SWARM BASED FIRING ANGLE OPTIMIZATION

3.1 INTRODUCTION

The switched reluctance machine operating principles were presented in the previous Chapter, highlighting its non-linear characteristics. From the model, it can be seen that the excitation interval, defined by the firing angles, considerably affects the performance of the SRM. Moreover, as presented in Chapter 1, a significant amount of research has been conducted regarding this topic.

This chapter presents as a contribution an SRM firing angle optimization procedure based on the particle swarm optimization algorithm. A new cost function is designed, aiming to ensure performance with a balance between reduced torque ripple and high energy efficiency. In order to avoid the use of lookup tables in digital implementation, the effect of load variation is disregarded. The procedure is intended for SRMs operating in the current controlled region, below base speed. A conventional fine grid optimization approach is presented and then an alternative is proposed, making use of the PSO algorithm. Simulation results are presented, comparing the results of each technique and showing the reduced computational effort of the proposed PSO-based procedure. After obtaining the optimal angles, a linear regression is performed, ensuring simplified digital implementation. Experimental results for the entire operating range are conducted, showing that a balance between energy efficiency and reduced torque ripple is achieved.

3.2 FIRING ANGLES

Differently than most electric machines, when operating below base speed, the SRM presents two additional degrees of freedom, its firing angles. For a given speed and load condition, several combinations of angles can be chosen, which directly impact the performance of the drive. A longer excitation interval may help to decrease torque ripple, while a smaller interval can reduce copper and iron losses, for example. Furthermore, speed and load have an effect on these parameters, requiring an entire profile to be determined.

In this context, the adequate choice of the excitation interval is of interest, and can be carried out aiming to improve one or more of the SRM's characteristics. Maximum efficiency and minimum torque ripple are criteria that cannot be satisfied simultaneously, in most situations (MADEMLIS; KIOSKERIDIS, 2003). Thus, the performance improve-

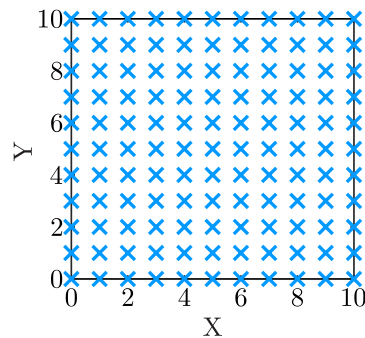
ment of an SRM can be performed by seeking a balance between reducing torque ripple and increasing energy efficiency. Given the highly nonlinear behavior of the SRM, the use of analytical formulations to determine the optimal firing angles becomes a complex task (MADEMLIS; KIOSKERIDIS, 2003; NETO et al., 2018). Hence, optimization algorithms are valuable tools in the determination of optimal firing angles.

Several studies have sought to find the optimal firing angles for SRMs, such as (TORREY, 2002; MADEMLIS; KIOSKERIDIS, 2003; KIOSKERIDIS; MADEMLIS, 2005; KIOSKERIDIS; MADEMLIS, 2009; MADEMLIS; KIOSKERIDIS, 2005; NETO et al., 2018; XUE et al., 2010; VUJICIC, 2012; BARROS et al., 2016). Many of them rely on a large number of simulations to be performed, resulting in substantial offline computational effort. Moreover, several proposals make use of lookup tables during digital implementation, requiring a significant amount of data to be stored in the microprocessor and increasing the overall complexity of the algorithm. Thus, a technique with reduced computational complexity and simple implementation is of interest, and will be presented in the following sections.

3.3 FINE GRID OPTIMIZATION

A straightforward way of performing parameter optimization is through a fine grid technique, also known as parameter sweep or brute force approach. The algorithm consists of an exhaustive search within a defined search space, usually divided in regularly spaced intervals. A generic example of a fine grid optimization can be observed in Figure 3.1, where two parameters are evaluated in equally spaced intervals.

Figure 3.1 – Fine grid optimization example.



Source: Author.

The main advantage of this strategy is that it guarantees an optimal solution will always be found. In addition, the response of the entire search space is evaluated, allowing the designer to better understand how each parameter affects the system. However, given every parameter combination is being evaluated, this optimization strategy presents higher

computational effort. Moreover, parameter sweeping strategies suffer from combinatorial explosion. As the search space increases or the parameter intervals decrease, the number of simulations grows exponentially. For the example presented in Figure 3.1, if the number of intervals were to be doubled, the number of points evaluated would increase by a factor of four, significantly increasing computational burden. Furthermore, depending on the size of the search space or the number of parameters to be optimized, a brute force approach may be impractical.

As an alternative, other strategies can be used in order to reduce computational effort while still providing the optimal results, as seen in the following section.

3.4 PARTICLE SWARM OPTIMIZATION

The use of intelligent algorithms is an efficient tool for solving problems with complex analytical formulations. An example is the particle swarm optimization (PSO), proposed by (KENNEDY; EBERHART, 1995). It is a metaheuristic inspired by the intelligence of groups observed in nature, like schools of fish and flocks of birds.

Some of the parameters used by the PSO algorithm are listed below:

- **Number of particles (N):** The number of points evaluated for each iteration of the algorithm. A larger number of particles improves convergence, however, increases computational effort. A small number of particles provides a faster solution, but may not properly evaluate certain regions of the search space.
- **Number of epochs (M):** The number of iterations of the PSO algorithm. Similar to the number of particles, a larger number of epochs improves the convergence of the algorithm, at the cost of increased execution time.
- **Cognitive and social coefficients (ψ_1 and ψ_2):** The weights that influence the particles movement based on the individual (ψ_1) and global (ψ_2) knowledge. Choosing $\psi_1 \gg \psi_2$ may result in excessive wandering, while picking $\psi_1 \ll \psi_2$ may cause premature convergence to local minima.

The algorithm starts with a group of N particles being randomly placed in the search space and the cost function being evaluated for every particle. The position of each particle, $s_x(k)$, is updated over the M epochs based on the following equations

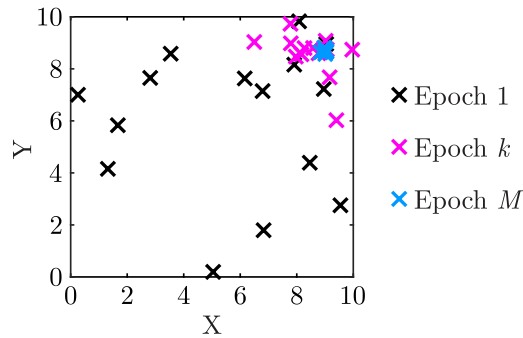
$$s_x(k+1) = s_x(k) + v_x(k+1) \quad , \quad x = 1 \dots N \quad , \quad k = 1 \dots M \quad (3.1)$$

$$v_x(k+1) = \lambda v_x(k) + \psi_1 r_1 (P_{x.best} - s_x(k)) + \psi_2 r_2 (G_{best} - s_x(k)) \quad (3.2)$$

where the speed of each particle in a given epoch, $v_x(k)$, is calculated based on the best known point by the particle ($P_{x.best}$) and the best known point by the swarm (G_{best}). Sub-index x refers to the particle number, while the value of k indicates the epoch in question. The parameters ψ_1 and ψ_2 are the cognitive and social coefficients, respectively. The terms r_1 and r_2 return a random value between 0 and 1. Lastly, λ is an inertia coefficient, used for slowing down the particles throughout the epochs (RAO, 2009).

The behavior of the PSO algorithm can be observed in a generic example, presented in Figure 3.2.

Figure 3.2 – Particle swarm optimization example.



Source: Author.

It can be seen that the particles move collectively from the initial random positions towards a point inside the search space. The swarm's convergence is visible, where nearly all the particles are grouped in the global minimum.

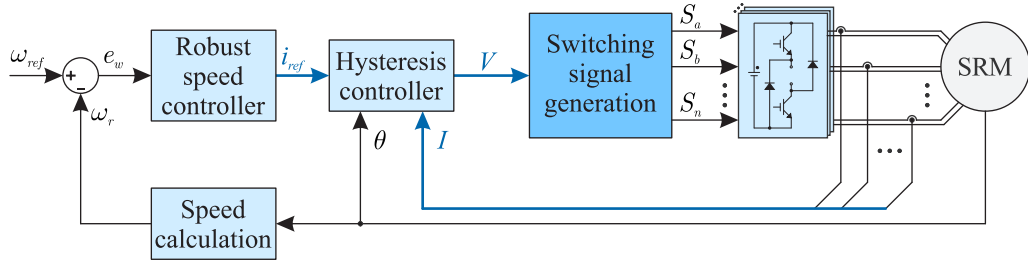
The strengths of the PSO algorithm, when compared to other optimization techniques, are its simplicity, faster convergence and the ease of implementation, avoiding cumbersome derivative calculations (GBENGA; RAMLAN, 2016), for instance. When compared to the brute force approach, presented in the previous section, a faster convergence is observed, given that the PSO algorithm does not need to sweep the entire search space, resulting in a lower number of objective function evaluations. It should be noted that the parameters of the PSO affect the results. Therefore, proper choice of the search space and algorithm parameters are necessary (SHI; EBERHART, 1998; EBERHART; SHI, 2001).

3.5 SRM FIRING ANGLE OPTIMIZATION ALGORITHMS

For operation as a motor, the firing angles of an SRM must be adjusted according to rotor speed and load in order to optimize the performance of the machine. Thus, the algorithms proposed in this section aim to determine the optimal SRM excitation interval based on dynamic simulations.

A simulation model is built in Matlab/Simulink, as described in Section 2.7. The block diagram of the control structure is presented in Figure 3.3. A robust speed controller designed via a Linear Matrix Inequality (LMI) framework, described in detail in Appendix B, is used in order to generate a reference current value based on the speed tracking error. Phase current is controlled through a hysteresis regulator, using soft-chopping. The output of the hysteresis regulator then determines the state of the AHB converter switches. SRM 1 is used for this example, having the following characteristics: three-phase 12/8 configuration, 2 kW, nominal speed of 157 rad/s and base speed of 110 rad/s.

Figure 3.3 – Block diagram of the control structure used for the simulations.



Source: Author.

In this thesis, a performance optimization for SRMs which aims to ensure a balance between reduced torque ripple and high energy efficiency is proposed. Thus, the cost function, used by the optimization algorithms, is defined as,

$$F(\theta_{on}, \theta_{off}) = \bar{T}_{ripple} + \bar{i}_{rms}^2 \quad (3.3)$$

where \bar{T}_{ripple} is the normalized torque ripple and \bar{i}_{rms}^2 is the normalized square RMS current value in phase “a”. The variables are normalized by dividing every result by the maximum verified value in the entire search space. Note that normalization is used as a means to make different unit variables compatible.

Torque ripple, T_{ripple} , is calculated as,

$$T_{ripple} = \frac{T_{max} - T_{min}}{T_{avg}} \quad (3.4)$$

where T_{max} is the maximum torque value, T_{min} is the minimum torque value and T_{avg} is the average torque value in a given time interval.

The value of \bar{i}_{rms}^2 was considered in the cost function, rather than the commonly used RMS value, to better account for the copper losses. In addition, when the current values are squared, the difference between the points becomes more evident, favoring the optimization process. A term containing peak flux value, as seen in (BARROS et al., 2016) and (NETO et al., 2018), was not considered. This is done due to the fact that copper

losses are prevalent in SRMs operating below base speed, with iron losses becoming more significant at high speeds (XUE et al., 2010). Moreover, minimizing the RMS current is a sufficiently effective approach, as it results in smaller copper losses and lower peak flux (TORREY, 2002).

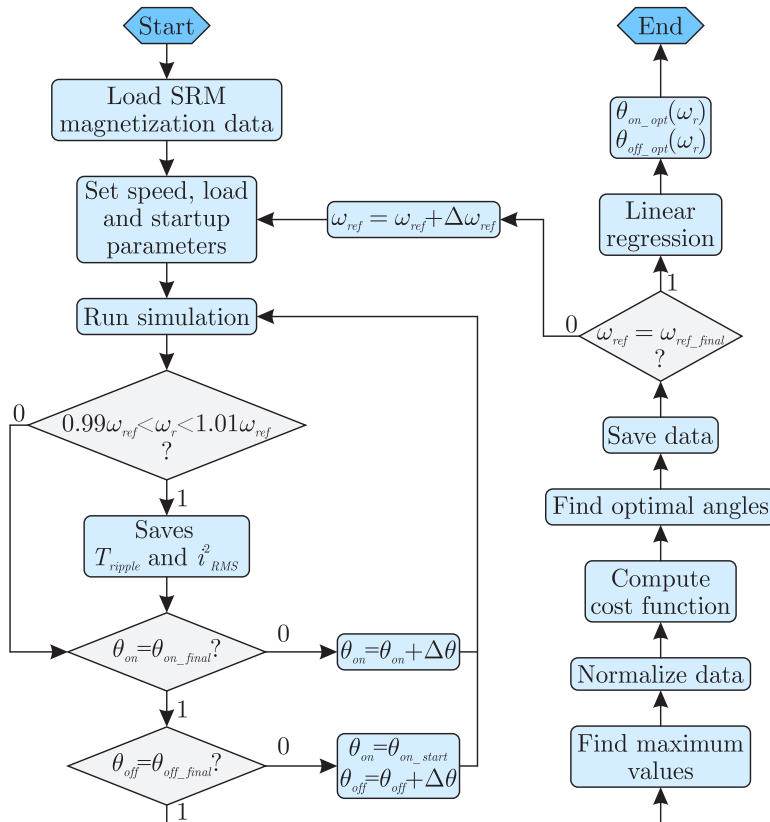
The optimal firing angles are also influenced by the load applied to the SRM (XUE et al., 2010; PAULA et al., 2020). Considering this effect, however, yields a lookup table of optimal parameters, dependent on both speed and load. In order to avoid the use of lookup tables during implementation, different load values are disregarded in the proposed optimization procedures. A load sensitivity analysis will be presented in Subsection 3.5.4.

In the following subsections two different approaches for finding the optimal firing angles will be presented, using fine grid and particle swarm optimization, respectively.

3.5.1 Fine grid optimization procedure

A flowchart of the proposed fine grid optimization procedure is presented in Figure 3.4. It was implemented in Matlab/Simulink software, with the startup parameters displayed in Table 3.1.

Figure 3.4 – Flowchart of the fine grid optimization procedure.



Source: Author.

Table 3.1 – Fine grid optimization startup parameters

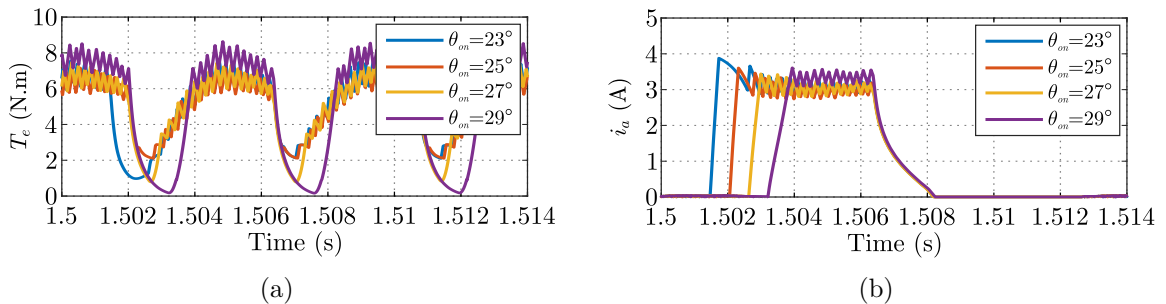
Parameter	Value
Initial speed	10 rad/s
Final speed	100 rad/s
Speed increment ($\Delta\omega_{ref}$)	10 rad/s
Mechanical load	5 Nm
θ_{on} bounds	$[23^\circ, 30^\circ]$
θ_{off} bounds	$[38^\circ, 44^\circ]$
Angle increment ($\Delta\theta$)	0.25°

Source: Author.

At first, the SRM's magnetization data is loaded, along with the startup parameters, such as speed, load and search space bounds. Then, this data is sent to Simulink and the simulation process starts. At the end of each simulation, the average speed is calculated and checked to see if it is within an acceptable error of the reference speed, in this case $\pm 1\%$. If the error is greater than $\pm 1\%$, the angle combination is disregarded in the optimization process. On the other hand, if the reference speed is reached, the torque ripple and RMS current values are stored. It should be noted that these values are obtained after the motor has reached steady state. Moreover, the speed condition is not met mostly on higher speed situations with small excitation intervals, for example.

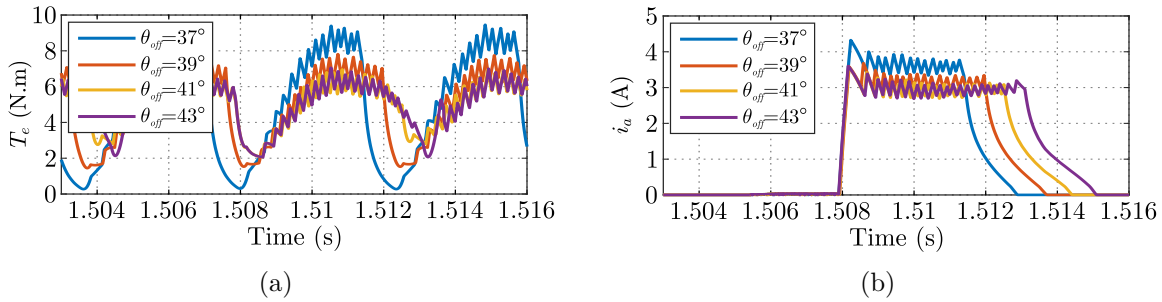
Once the values are stored, the θ_{on} angle is incremented, and the processes is repeated until the condition $\theta_{on} = \theta_{on_final}$ is met. After θ_{on_final} is reached, the value is reset and θ_{off} is incremented. The simulations are finished when $\theta_{off} = \theta_{off_final}$. Figures 3.5 (a) and (b) present the electromagnetic torque and phase “a” current waveforms for a speed of 60 rad/s, respectively. Four different values of θ_{on} are considered (23° , 25° , 27° , 29°), while θ_{off} is kept constant at 40° . Similar reasoning is presented in Figures 3.6 (a) and (b), where four different values of θ_{off} are considered (37° , 39° , 41° , 43°), while θ_{on} is kept constant at 25° .

Figure 3.5 – Simulation results for different values of θ_{on} with $\theta_{off} = 40^\circ$, at a speed of 60 rad/s. (a) Electromagnetic torque. (b) Phase “a” current.



Source: Author.

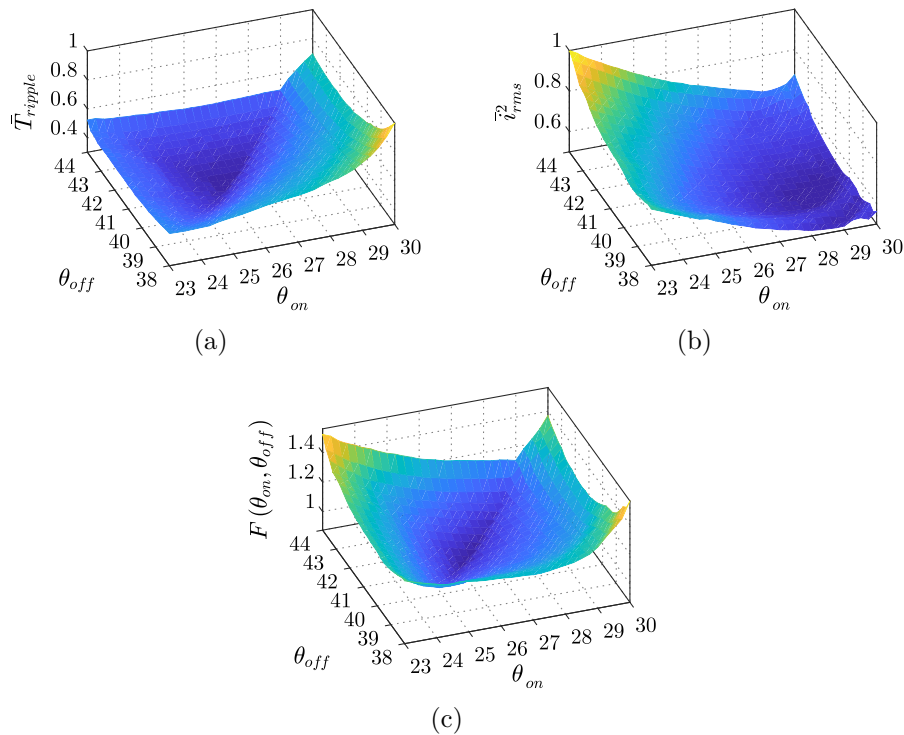
Figure 3.6 – Simulation results for different values of θ_{off} with $\theta_{on} = 25^\circ$, at a speed of 60 rad/s. (a) Electromagnetic torque. (b) Phase “a” current.



Source: Author.

After all the simulations for a given speed are performed, the maximum values of each variable are located, in order to normalize the results. The cost function, presented in (3.3), is then computed for all points, and the point with the lowest cost is located. The firing angles corresponding to this point are saved as the optimal values for that speed. Figure 3.7 shows the simulation results of normalized torque ripple, square RMS current, and cost function for all angle combinations at a speed of 60 rad/s.

Figure 3.7 – Simulation results for a speed of 60 rad/s. (a) Normalized torque ripple. (b) Normalized squared RMS current. (c) Cost function.

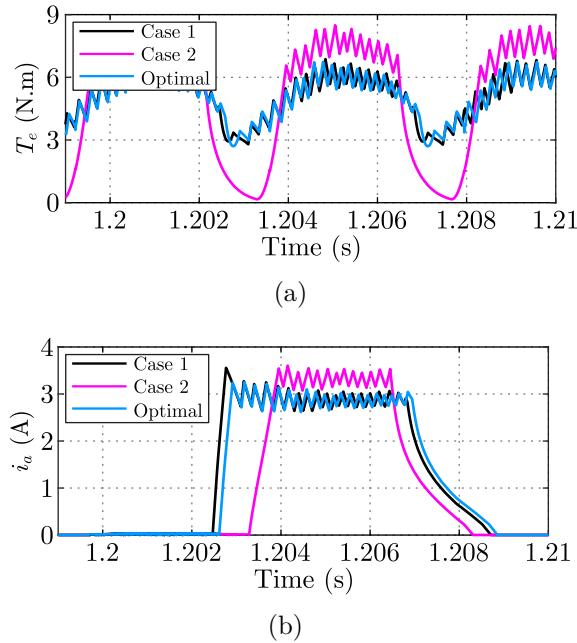


Source: Author.

In this case, the minimum value for the cost function is located at $\theta_{on} = 26.5^\circ$ and $\theta_{off} = 41.5^\circ$.

Figure 3.8 presents the electromagnetic torque and phase “a” current waveforms for a speed of 60 rad/s. For comparison purposes, three different cases are evaluated, operating in the conditions of minimum torque ripple (Case 1), minimum losses (Case 2) and in the optimal condition (Optimal), resulting from the optimization procedure. Note that Case 1 only considers the minimum \bar{T}_{ripple} metric, while Case 2 only considers the minimum \bar{i}_{rms}^2 metric.

Figure 3.8 – Simulation results for a speed of 60 rad/s. (a) Electromagnetic torque. (b) Phase “a” current.



Source: Author.

The simulation procedure is repeated until the last speed value is evaluated. With the optimum firing angles for each speed value, a linear regression is performed, where the data is fitted to a straight line, allowing easy implementation in a microprocessor. Thus, the resulting optimal firing angles for operation below base speed are given by

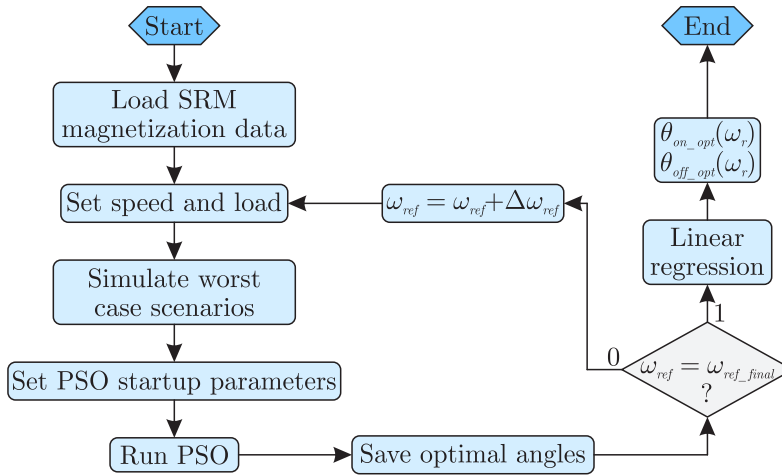
$$\begin{aligned} \theta_{on_opt}(\omega_r) &= -0.0198\omega_r + 27.72 \\ \theta_{off_opt}(\omega_r) &= -0.0198\omega_r + 42.72 \end{aligned} \quad (3.5)$$

A total of 7250 simulations were carried out during the execution of the fine grid optimization procedure.

3.5.2 Particle swarm optimization procedure

A flowchart of the proposed particle swarm optimization procedure is presented in Figure 3.9. Similarly to the fine grid procedure, it was implemented in Matlab/Simulink software, with the startup parameters displayed in Table 3.2.

Figure 3.9 – Flowchart of the particle swarm optimization procedure.



Source: Author.

Table 3.2 – Particle swarm optimization startup parameters.

Parameter	Value
Number of particles (N)	5
Number of epochs (M)	25
Cognitive coefficient (ψ_1)	0.5
Social coefficient (ψ_2)	0.5
θ_{on} bounds ($^\circ$)	[23, 30]
θ_{off} bounds ($^\circ$)	[38, 44]

Source: Author.

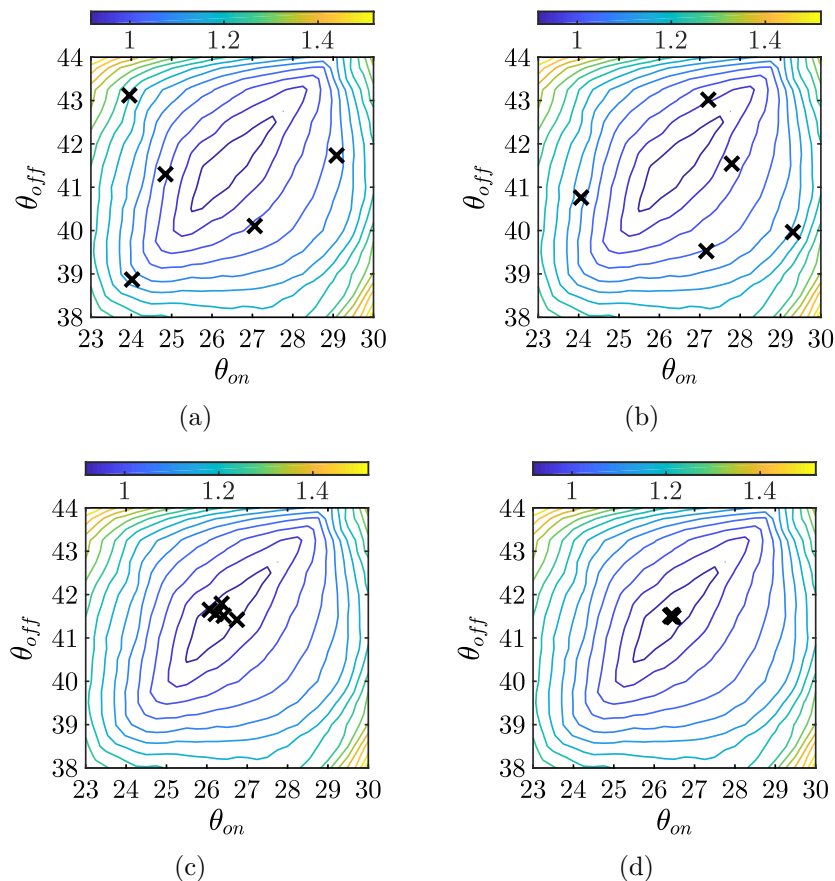
The number of epochs and particles are chosen based on preliminary tests, opting for values that resulted in good convergence and low computational effort. Moreover, the choice of equal cognitive and social coefficients is made following guidelines given in (KENNEDY; EBERHART, 1995).

At first, the SRM's magnetization data is loaded, along with the startup parameters, such as speed, load and firing angle bounds. Then, before the start of the PSO, two simulations are performed, in order to obtain the maximum values for torque ripple and RMS current within the search space. The values are often located at the smaller and bigger excitation intervals, respectively. Prior knowledge of these values is necessary

because the terms in the cost function must be normalized at the end of each simulation, given the nature of the PSO algorithm. After that, data is sent to Simulink and the simulation process starts. At the end of each simulation, it is verified whether the reference speed has been reached, and, if not, a value of $F(\theta_{on}, \theta_{off}) = 1000$ is assigned to the cost function, indicating to the algorithm that the angle combination is not suitable. Once the PSO algorithm reaches the set number of epochs, the best known result is stored as the optimal firing angles for the evaluated speed.

Figure 3.10 shows the simulation results for the PSO algorithm, in four different epochs, at a speed of 60 rad/s. When compared to the contours of Figure 3.7 (c), plotted on the background, it is possible to observe that the particles converge to the minimum of the function just like the fine grid method does, while performing significantly less simulations.

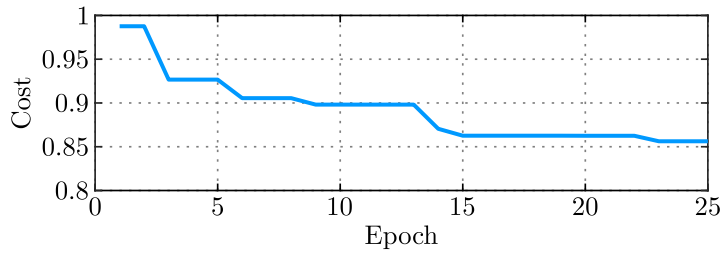
Figure 3.10 – Simulation results for a speed of 60 rad/s. (a) Epoch 1. (b) Epoch 10. (c) Epoch 18. (d) Epoch 25.



Source: Author.

Figure 3.11 shows the evolution of cost function value over the epochs, allowing the convergence of the PSO algorithm to be observed.

Figure 3.11 – Evolution of cost function value over the epochs.



Source: Author.

Once again, the simulation procedure is repeated until the last speed value is evaluated. With the optimum firing angles for each speed value, a linear regression is performed, where the data is fitted to a straight line. The resulting optimal firing angles are given by

$$\begin{aligned}\theta_{on_opt}(\omega_r) &= -0.0189\omega_r + 27.71 \\ \theta_{off_opt}(\omega_r) &= -0.0192\omega_r + 42.75\end{aligned}\quad (3.6)$$

A total of 1270 simulations were carried out during the execution of the particle swarm optimization procedure, resulting in a 82.5% reduction of the computational effort when compared to the fine grid optimization procedure.

3.5.3 Optimization procedures comparison

The optimal firing angles and the final cost function value for both procedures are presented in Table 3.3.

Table 3.3 – Optimization results for the fine grid and particle swarm procedures.

Speed (rad/s)	Fine grid			PSO		
	θ_{on} (°)	θ_{off} (°)	Cost	θ_{on} (°)	θ_{off} (°)	Cost
10	27.75	42.75	0.8714	27.66	42.68	0.8538
20	27.25	42.25	0.9857	27.41	42.57	0.9914
30	27.00	42.00	0.9657	27.00	42.00	0.9889
40	27.00	42.00	0.9746	26.69	41.69	0.9582
50	26.75	41.75	0.9229	26.78	41.78	0.9204
60	26.50	41.50	0.8744	26.48	41.48	0.8562
70	26.00	41.00	0.7812	26.48	41.51	0.7836
80	26.00	41.00	0.8070	26.50	41.51	0.7993
90	26.00	41.00	0.7634	25.99	40.99	0.7744
100	26.00	41.00	0.5534	25.68	40.75	0.5554

Source: Author.

It can be observed that the optimal angle results are similar in both cases. It can also be seen that, for certain speeds, the PSO based procedure is able to find lower cost function values when compared to the fine grid procedure, indicating that a condition with better performance was found. It should be noted that due to the random nature of the PSO algorithm startup, results may vary. However, with a large enough number of particles and epochs, the convergence of the algorithm is verified.

In order to analyze the dispersion of the PSO algorithm results, the procedure was repeated 10 times for the speed of 60 rad/s. From the obtained results, it is possible to calculate the coefficient of variation for the final values of the cost function and optimal firing angles, according to

$$CV = \frac{\sigma}{\mu}, \quad (3.7)$$

where CV is the coefficient of variation, σ is the standard deviation and μ is the mean. The results are shown in (A.4).

$$CV_{\theta_{on}} = 0.49\%; \quad CV_{\theta_{off}} = 0.30\%; \quad CV_{F(\theta_{on}, \theta_{off})} = 0.67\% \quad (3.8)$$

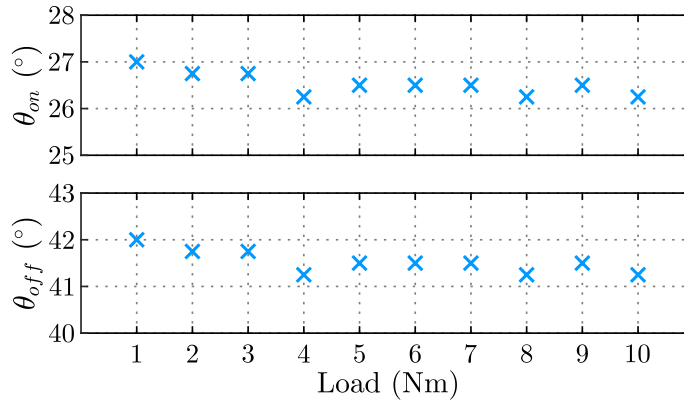
A low dispersion is verified within the results, indicating good convergence and repeatability of the proposed PSO procedure in this case study.

3.5.4 Load sensitivity

The optimal firing angles are also influenced by the load applied to the SRM (XUE et al., 2010; PAULA et al., 2020). Electromagnetic torque estimation for SRMs, however, is more complex when compared to the speed measurement, inherently available in a variable speed drive. In addition, considering different load conditions in the optimization procedure significantly increases the computational cost of the problem. The result of the procedure becomes a lookup table of optimal firing angles, requiring significant memory allocation in digital implementation and increasing the overall complexity of the control algorithm.

Considering that the proposal disregards the load torque in the optimization procedure, this section aims to assess the sensitivity of the obtained results to mechanical load variations. Figure 3.12 presents the result of the fine grid optimization procedure for different load values, at a speed of 60 rad/s.

Figure 3.12 – Optimal firing angles as a function of the load torque at a speed of 60 rad/s.



Source: Author.

For low load conditions, a greater difference is observed in relation to the optimal value, at 5 Nm. For various applications, however, the operation of electric motors in these conditions is of less interest. For medium and high load conditions the values are within 1% difference of the obtained optimal parameters. The algorithm, then, operates a portion of the time in or near the optimal region. For lower load conditions, the SRM operates in a sub-optimal region. Therefore, even when disregarding the effects different load conditions, adequate system performance is observed, while still presenting a simple implementation, since the use of lookup tables is avoided. However, note that to ensure the best possible performance, load must be considered in the optimization procedure.

3.6 EXPERIMENTAL RESULTS

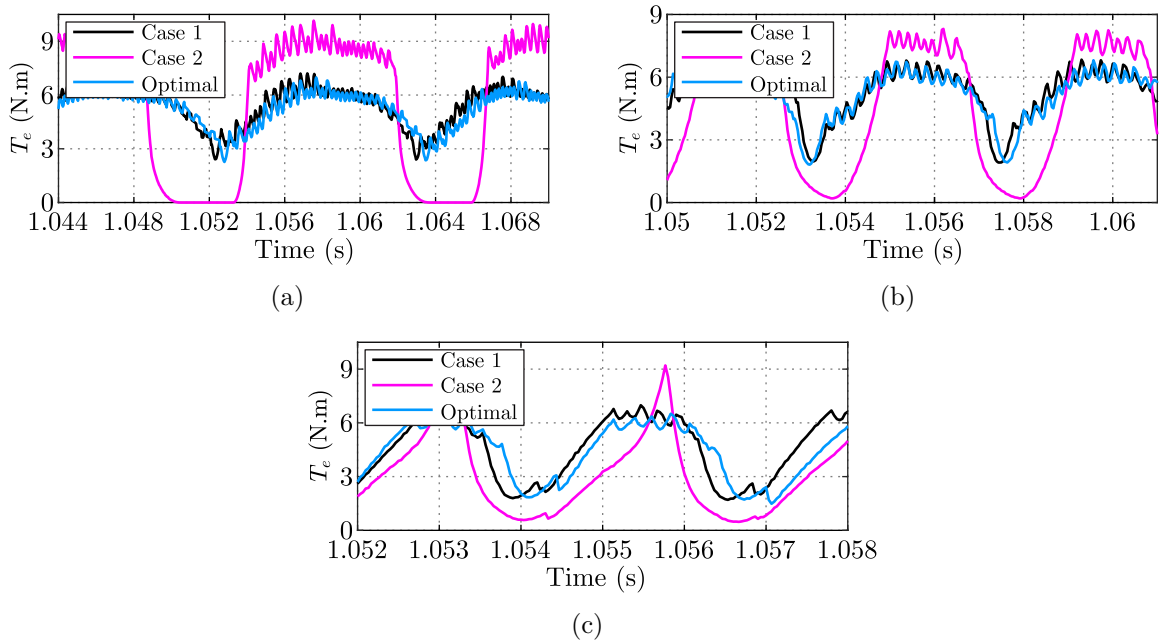
In this section, experimental results are presented for SRM 1 operating with variable firing angles, in order to validate the proposed optimization procedures. The experimental setup used is described in Appendix C. The SRM is coupled to an induction machine, which operates as a self-excited generator. The terminals of the induction machine are connected to a capacitor bank and resistors, providing a load for the SRM. A regulated DC power supply (500V/20A) is connected to the DC bus. A Minipa sound meter, model MSL-1350, is used to measure the sound level during the SRM operation, in order to verify the acoustic noise production. However, note that no radial force optimization is considered in the proposed procedure.

The control system is implemented in a Texas Instruments TMS320F28335 digital signal processor and the rotor position is obtained through a 10-bit absolute encoder. A sampling frequency of $f_s = 30$ kHz is used.

Initially, experimental results are obtained for the SRM operating at speeds of 20, 60 and 100 rad/s. The system is evaluated for the conditions of minimum torque ripple

(Case 1), minimum losses (Case 2) and for the condition resulting from the optimization procedure (Optimal). Figures 3.13 and 3.14 show the electromagnetic torque and phase “a” currents, respectively. The torque waveforms are obtained through the torque lookup table (BARROS et al., 2018), using the characteristics presented in Chapter 2. The approach makes use of current and rotor position experimental data, stored in the DSP memory, to recover the torque waveforms. The performance of the three cases, for the different speed values, can also be compared through the results presented in Table 3.4.

Figure 3.13 – Experimental results of electromagnetic torque for different speeds. (a) 20 rad/s. (b) 60 rad/s. (c) 100 rad/s.



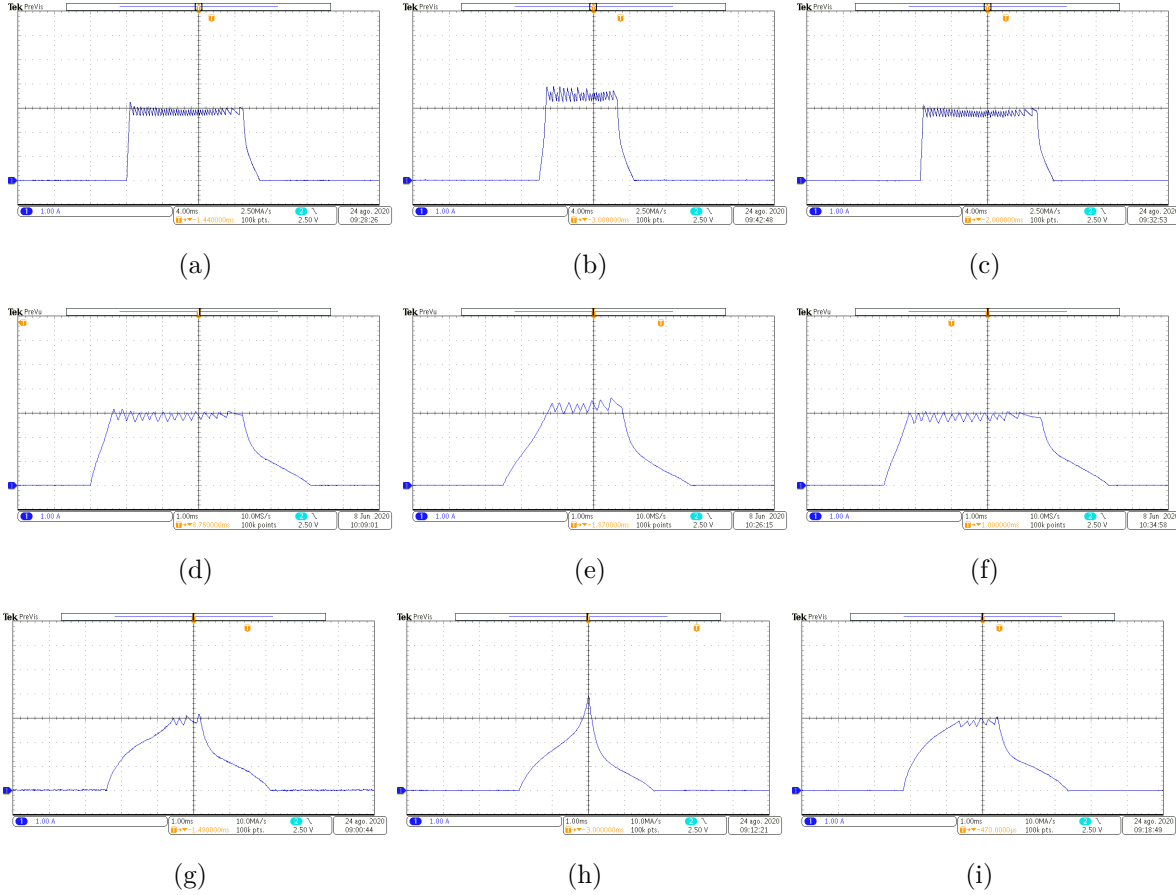
Source: Author.

Table 3.4 – Experimental results comparison.

Speed	Variable	Case 1	Case 2	Optimal
20 rad/s	i_{rms} (A)	1.857	1.663	1.818
	T_{avg} (N.m)	5.21	4.94	5.06
	T_{ripple} (%)	92.3	197.9	95.15
60 rad/s	i_{rms} (A)	1.717	1.512	1.691
	T_{avg} (N.m)	5.12	4.46	5.00
	T_{ripple} (%)	100.5	189.0	102.4
	Acoustic noise (dB)	65.8	77.6	69.1
100 rad/s	i_{rms} (A)	1.601	1.178	1.567
	T_{avg} (N.m)	4.46	3.17	4.23
	T_{ripple} (%)	121.6	293.5	135.1

Source: Author.

Figure 3.14 – Experimental results of phase “a” current. Speed of 20 rad/s: (a) Case 1; (b) Case 2; (c) Optimal. Speed of 60 rad/s: (d) Case 1; (e) Case 2; (f) Optimal. Speed of 100 rad/s: (g) Case 1; (h) Case 2; (i) Optimal. CH1: Phase “a” current (1 A/div).



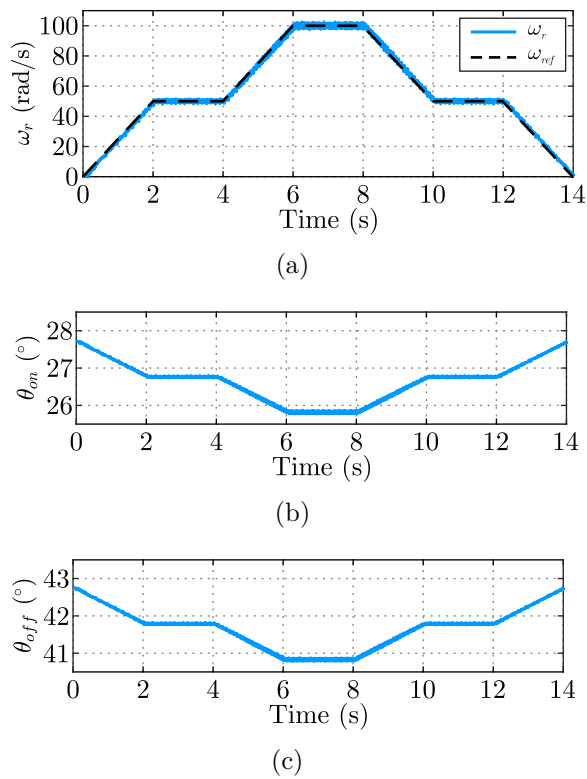
Source: Author.

For case 1, the smallest torque ripple values are verified for all three evaluated speeds, however, a greater current amplitude is observed and, consequently, greater losses. Additionally, case 1 presents the lowest acoustic noise value, measured at a speed of 60 rad/s. For the situation with minimum losses, case 2, the lowest values of RMS current are observed, however, high torque ripple and acoustic noise are detected. It should also be noted that the reduced interval and high back-EMF at the speed of 100 rad/s lead to a result with single pulse operation in Figure 3.14 (e). The optimal case presents a very similar behavior to Case 1 over the analyzed speed range, within a 5% difference in torque ripple and RMS current values. In order to adequately ensure a balance between torque ripple reduction and increased energy efficiency, weighting factors should be considered in equation (3.3). For this example, note that a higher weight is required for the i_{rms}^2 metric in order to ensure a balanced performance. In addition, note that the cost function used can be modified in order to meet different objectives, while still making use of the proposed

procedure.

In order to further validate the proposed strategy, a variable speed result is presented in Figure 3.15. The speed reference consists of two ramps followed by two plateaus, at the speeds of 50 and 100 rad/s. The profile is mirrored so that the deceleration characteristic is also observed. The firing angles are calculated according to (3.6). Satisfactory tracking of the speed reference is observed. The angles are adjusted according to the rotor speed, allowing the SRM to continuously operate in the region determined by the optimization procedure.

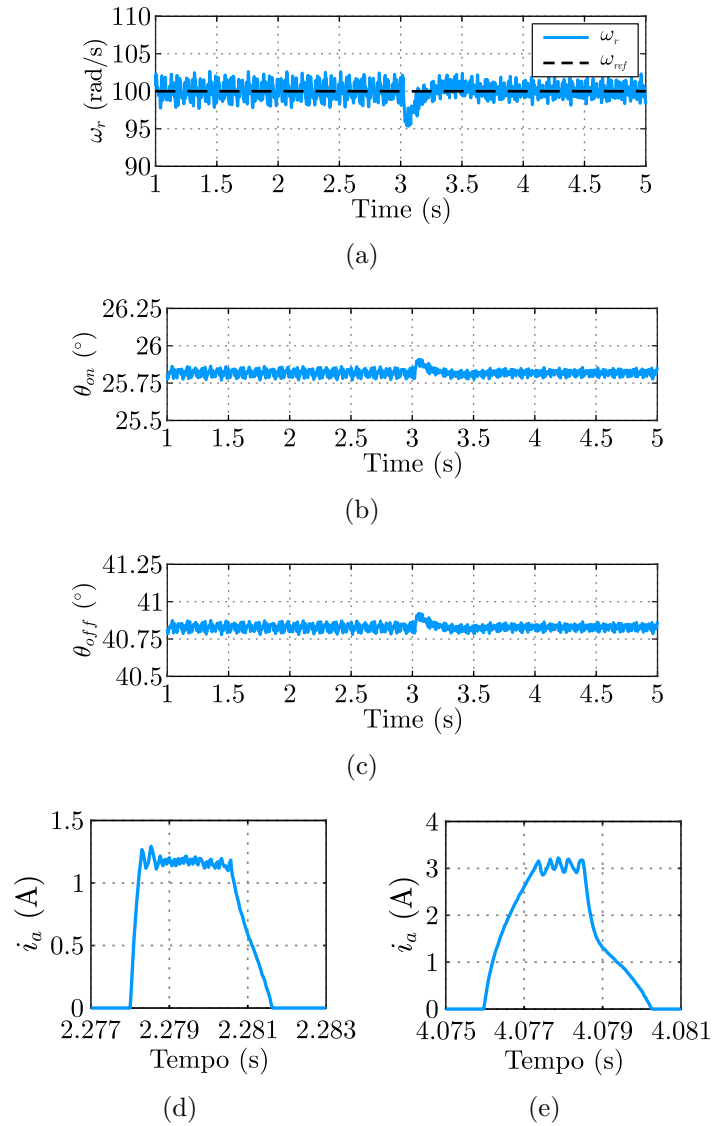
Figure 3.15 – Experimental result for variable speed operation. (a) Measured and reference speed. (b) θ_{on} . (c) θ_{off} .



Source: Author.

Figure 3.16 presents the response for rejection of a load step disturbance. This test is carried out in order to evaluate the procedure under variable load conditions. Initially, the speed reference is set to 100 rad/s and on $t = 3$ s a load step of approximately 5.5 Nm is applied to the SRM. The load is imposed by means of a self-excited induction generator connected to a three-phase resistive load, made up of three 90 Ω resistors connected in a Y configuration. The current waveforms before and after the load step disturbance are presented in Figures 3.16 (d) and 3.16 (e), respectively.

Figure 3.16 – Experimental result for load step disturbance. (a) Measured and reference speed. (b) θ_{on} . (c) θ_{off} . (d) Phase “a” current before load step. (e) Phase “a” current after load step.



Source: Author.

The system presents satisfactory speed regulation when subject to a load disturbance. The angles are briefly changed during the load step, following the speed transient. Finally, an increase in phase current amplitude is observed, caused by the connection of the resistive load to the induction generator.

3.7 CONCLUSION

In this Chapter, an SRM firing angle optimization procedure based on the particle swarm optimization algorithm was proposed. The procedure proved to be equally capable of locating optimal parameters when compared to the fine grid approach, while reducing computational effort by approximately 82.5%. Furthermore, the PSO procedure presented low dispersion, indicating the good repeatability of the proposal. Through the sensitivity analysis, the effects of different mechanical loads in the optimization procedure were shown, resulting in a system that operates in a sub-optimal region for certain load values. Simulation and experimental results proved that the proposed procedure achieved performance with a balance between efficiency and torque ripples.

Although torque ripple reduction is achieved by the proposed algorithm, note that the measured values are still within the 90 to 120% range, which may be unacceptable for several applications. As a means to effectively reduce torque ripple, a TSF strategy will be employed in the following Chapter. Adequate current reference tracking can help to further improve the performance of TSFs. As a result, in the following Chapter, a discrete-time robust current controller will be proposed, aiming to ensure superior tracking performance with a fixed switching frequency.

4 DISCRETE-TIME SUPER-TWISTING SLIDING MODE CURRENT CONTROLLER WITH FIXED SWITCHING FREQUENCY

4.1 INTRODUCTION

Torque ripple can be effectively reduced with the use of torque sharing functions, a technique that allows a constant torque to be produced by generating adequate current references for each active phase. However, the performance of such strategy relies on accurate current controllers (XUE; CHENG; HO, 2009).

Hysteresis control is the most commonly used strategy for the current control of SRMs, due to its simplicity and independence of the model (BILGIN; JIANG; EMADI, 2019; YE; BILGIN; EMADI, 2015c). This technique also presents advantages such as fast dynamic response, high robustness and lack of sensitivity for parametric variations. However, it presents drawbacks such as a variable switching frequency, due to the varying phase inductance. Moreover, during digital implementation, sampling limitations lead to higher current ripple and, consequently, torque ripple. These issues are significantly more noticeable in low-speed conditions and SRMs with low inductance values. Increasing the sampling frequency can be used to improve the performance of hysteresis controllers, reducing current ripple (FANG et al., 2021b). However, it also tends to increase the cost of the overall control system.

In order to avoid these issues, SRM current control strategies with fixed switching frequency have been investigated in the past few years (DHALE; NAHID-MOBARAKEH; EMADI, 2021; FANG et al., 2021a).

This Chapter presents as a main contribution a novel discrete-time super-twisting sliding mode (DTSTSM) current control scheme for switched reluctance motors. The proposed controller presents robustness, while maintaining a simple structure, not requiring any knowledge of the machine parameters on implementation. In addition, the proposal presents enhanced tracking performance, delivering lower current and torque ripple, especially in the low to medium speed range. The strategy is implemented with the use of PWM, ensuring a fixed switching frequency. The stability analysis is investigated by means of a Lyapunov approach and, unlike what has been previously reported in literature, the digital control implementation delay is taken into account, through an augmented model. One difficulty of super-twisting sliding mode controllers is the appropriate gain selection. To overcome this issue and guarantee a systematic and straightforward design stage, a third contribution is given by a novel gain design procedure, where a cost function

is used to determine the suitable controller gains, leading to fast dynamic responses and low current ripple. The procedure is repeated for different speeds, allowing the DTSTSM controller gains to be adjusted online, according to the rotor speed. Experimental results are provided to demonstrate the effectiveness of the DTSTSM controller, where a conventional hysteresis controller is used for comparison in terms of sampling frequencies, computational complexity, current and torque root-mean-square-errors.

The main contributions of this Chapter can be summarized as follows:

1. A novel DTSTSM current controller with fixed switching frequency for SRMs. Compared to other PWM-based controllers, the proposed controller does not require lookup tables or any knowledge of the machine parameters on hardware implementation, presenting a simple structure and robust performance.
2. An original stability analysis, using an augmented model that takes into account the one sample digital implementation delay.
3. A systematic and straightforward gain design procedure for super-twisting sliding mode controllers. In addition, gain adaptation is employed with respect to rotor speed, allowing improved tracking over a wide range of speed.

4.2 DISCRETE-TIME SUPER-TWISTING SLIDING MODE CURRENT CONTROLLER

Conventional discrete-time sliding mode control strategies exhibit chattering as a major drawback in practical applications. Chattering is a phenomenon referred to as oscillations of finite amplitude and frequency, which occurs as a result of the sliding action of the controller. This effect is undesirable as it can decrease control accuracy and, on SRM current controllers, lead to increased current ripple (UTKIN; LEE, 2006). The super-twisting algorithm, proposed by (LEVANT, 1993), is able to effectively reduce chattering, without major compromises (GONZALEZ; MORENO; FRIDMAN, 2012; BARATIERI; PINHEIRO, 2016). In this section, a discrete-time super-twisting sliding mode current controller for SRMs is described. A novel stability proof, considering the digital implementation delay through an augmented model, is also presented.

4.2.1 Controller structure

First, consider a sliding surface, $s(k)$, defined as

$$s(k) = e(k) = i(k) - i_{ref(k)} \tag{4.1}$$

where $e(k)$ is the current tracking error, $i(k)$ is the measured phase current and $i_{ref(k)}$ is the reference current. In accordance with (KOCH; REICHHARTINGER, 2019), a DTSTSM control law can be written as

$$v(k) = -k_1 |s(k)|^{\frac{1}{2}} sign(s(k)) + u(k) \tag{4.2}$$

$$u(k) = \gamma u_{(k-1)} - k_2 T_s sign(s(k)) \tag{4.3}$$

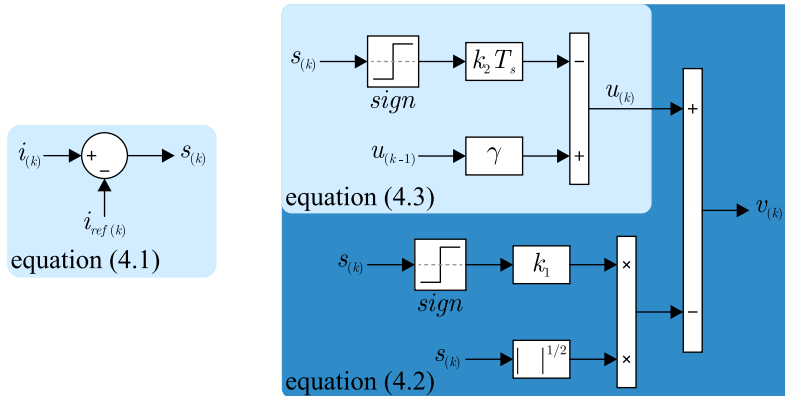
where $v(k)$ is the controller output, $u(k)$ is the auxiliary variable of the DTSTSM controller, γ is a fixed gain with $0 < \gamma < 1$, k_1 and k_2 are the controller gains and T_s is the sampling period.

The signal function, $sign(s(k))$, is defined as

$$sign(s(k)) = \begin{cases} 1 & \text{if } s(k) > 0 \\ 0 & \text{if } s(k) = 0 \\ -1 & \text{if } s(k) < 0 \end{cases} . \tag{4.4}$$

A block diagram of the DTSTSM controller, described in equations (4.1)–(4.3), is presented in Figure 4.1. Note that for implementation, the controller only requires knowledge of the gains as well as the reference and measured currents, not requiring any lookup table or additional machine parameters.

Figure 4.1 – Block diagram of the DTSTSM controller.

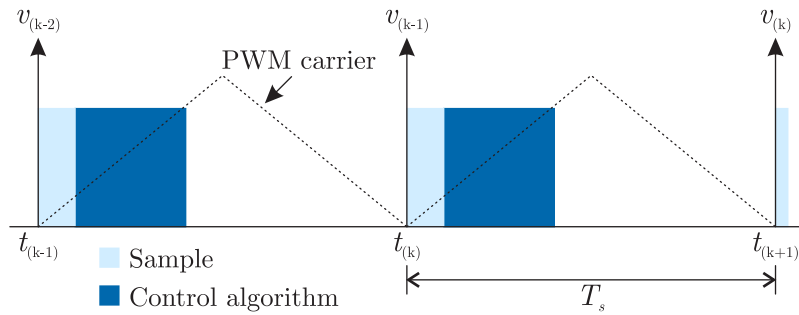


Source: Author.

4.2.2 Stability analysis

In digitally controlled motor drives, it is common practice to sample the phase currents and rotor position at the same instant that the voltage commands are updated. In symmetric PWM applications, these variables are updated once per cycle, thus, resulting in an intrinsic delay of T_s , as depicted in Figure 4.2 (KIM et al., 2010). If not properly addressed, this phenomenon may affect the stability of the closed-loop system.

Figure 4.2 – Digital implementation delay in discrete-time control systems using symmetric PWM.



Source: Author.

In order to address this issue, first the discrete form of (2.8) can be obtained by using the forward Euler method, as seen in (4.5).

$$i_{(k+1)} = \left(1 - T_s \frac{R}{l(\theta, i)}\right) i_{(k)} - \frac{T_s}{l(\theta, i)} \epsilon_{(k)} + \frac{T_s}{l(\theta, i)} v_{(k)} \quad (4.5)$$

Next, an augmented model can be derived from (4.5), where an additional state, $v_d(k)$, is included to account for the digital control implementation delay.

$$\begin{aligned} \begin{bmatrix} i_{(k+1)} \\ v_d(k+1) \end{bmatrix} &= \begin{bmatrix} 1 - T_s \frac{R}{l(\theta, i)} & \frac{T_s}{l(\theta, i)} \\ 0 & 0 \end{bmatrix} \begin{bmatrix} i_{(k)} \\ v_d(k) \end{bmatrix} \\ &+ \begin{bmatrix} 0 \\ 1 \end{bmatrix} v_{(k)} + \begin{bmatrix} -\frac{T_s}{l(\theta, i)} \epsilon_{(k)} \\ 0 \end{bmatrix} \end{aligned} \quad (4.6)$$

Then, considering the model presented in (4.6) and the controller given in (4.2) and (4.3), the nonlinear augmented system can be rewritten in the form of

$$\mathbf{x}_{(k+1)} = \mathbf{A} \mathbf{x}_{(k)} + \mathbf{B}_{(k)} s_{(k)} + \boldsymbol{\xi}_{(k)} \quad (4.7)$$

where

$$\begin{aligned} \mathbf{x}_{(k)} &= \begin{bmatrix} x_{1(k)} & x_{2(k)} & x_{3(k)} \end{bmatrix}^T \\ &= \begin{bmatrix} s_{(k)} & v_d(k) & u_{(k)} \end{bmatrix}^T \end{aligned} \quad (4.8)$$

$$\mathbf{A} = \begin{bmatrix} 1 - T_s \frac{R}{l(\theta, i)} & \frac{T_s}{l(\theta, i)} & 0 \\ 0 & 0 & 1 \\ 0 & 0 & \gamma \end{bmatrix} \quad (4.9)$$

$$\mathbf{B}_{(k)} = \begin{bmatrix} 0 & -k_1 |s_{(k)}|^{\frac{1}{2}} & -k_2 T_s \end{bmatrix}^T \quad (4.10)$$

$$\begin{aligned} \boldsymbol{\xi}_{(k)} &= \begin{bmatrix} \xi_{1(k)} & 0 & 0 \end{bmatrix}^T \\ &= \begin{bmatrix} -\frac{T_s}{l(\theta, i)} \epsilon_{(k)} - \left(i_{ref(k+1)} - \left(1 - T_s \frac{R}{l(\theta, i)} \right) i_{ref(k)} \right) & 0 & 0 \end{bmatrix}^T \end{aligned} \quad (4.11)$$

The stability of the closed loop system, taking the one sample delay into account, is given by the following theorem.

Theorem 1: Consider the nonlinear system given in (4.7), with gains chosen as $k_1 > 0$, $k_2 > 0$, $0 < \gamma < 1$ and if the following linear matrix inequality (SALGADO et al., 2014; BARATIERI; PINHEIRO, 2016; WANG et al., 2020)

$$\mathbf{A}^T (\mathbf{P} + \mathbf{P} (\boldsymbol{\Lambda}_1 + \boldsymbol{\Lambda}_2) \mathbf{P}) \mathbf{A} - (1 - \rho) \mathbf{P} + \mathbf{Q} \leq 0 \quad (4.12)$$

has a positive-definite solution $\mathbf{P} = \mathbf{P}^T > 0$ for a given $\mathbf{Q} = \mathbf{Q}^T > 0$, $\boldsymbol{\Lambda}_1 = \boldsymbol{\Lambda}_1^T > 0$ and $\boldsymbol{\Lambda}_2 = \boldsymbol{\Lambda}_2^T > 0$, then the trajectories of the system described in (4.7) converge asymptotically to a region centered at the origin $\mathbf{O} = \{x : \|x\|^2 < r\}$, with a radius given by

$$r = \frac{c}{\rho} \quad (4.13)$$

where

$$\begin{aligned} 0 &< \rho < 1 \\ c &= \left(\frac{\alpha_2}{2\sqrt{\alpha_1}} \right)^2 + \alpha_3 \\ \alpha_1 &= \lambda_{\min}(\mathbf{Q}) > 0 \\ \alpha_2 &= \lambda_{\max}(\mathbf{Z}) k_1^2 \\ \alpha_3 &= \lambda_{\max}(\mathbf{Z}) (k_2 T_s)^2 + \lambda_{\max}(\mathbf{H}) \xi_{1(k)}^2 \\ \mathbf{Z} &= \mathbf{Z}^T = \boldsymbol{\Lambda}_1^{-1} + \boldsymbol{\Lambda}_3^{-1} + \mathbf{P} > 0 \\ \mathbf{H} &= \mathbf{H}^T = \boldsymbol{\Lambda}_2^{-1} + \mathbf{P} \boldsymbol{\Lambda}_3 \mathbf{P} + \mathbf{P} > 0 \end{aligned}$$

Proof. The proof of Theorem 1 is based on (SALGADO et al., 2014; BARATIERI; PINHEIRO, 2016; WANG et al., 2020).

Consider the Lyapunov candidate function

$$V_{(k)} := \left\| \mathbf{x}_{(k)} \right\|_{\mathbf{P}}^2 = \mathbf{x}_{(k)}^T \mathbf{P} \mathbf{x}_{(k)}. \quad (4.14)$$

So $\Delta V_{(k)} = V_{(k+1)} - V_{(k)}$ can be rewritten as

$$\Delta V_{(k)} = \mathbf{x}_{(k+1)}^T \mathbf{P} \mathbf{x}_{(k+1)} - \mathbf{x}_{(k)}^T \mathbf{P} \mathbf{x}_{(k)}. \quad (4.15)$$

where $\mathbf{P} = \mathbf{P}^T > 0$.

Replacing the augmented model, (4.7), in (4.15), results

$$\begin{aligned} \Delta V_{(k)} = & \left(\mathbf{A} \mathbf{x}_{(k)} + \mathbf{B}_{(k)} \text{sign}(s_{(k)}) + \boldsymbol{\xi}_{(k)} \right)^T \mathbf{P} \left(\mathbf{A} \mathbf{x}_{(k)} + \mathbf{B}_{(k)} \text{sign}(s_{(k)}) + \boldsymbol{\xi}_{(k)} \right) \\ & - \mathbf{x}_{(k)}^T \mathbf{P} \mathbf{x}_{(k)}. \end{aligned} \quad (4.16)$$

Expanding (4.16) results in

$$\begin{aligned} \Delta V_{(k)} = & \mathbf{x}_{(k)}^T \left(\mathbf{A}^T \mathbf{P} \mathbf{A} - \mathbf{P} \right) \mathbf{x}_{(k)} + \mathbf{x}_{(k)}^T \mathbf{A}^T \mathbf{P} \mathbf{B}_{(k)} \text{sign}(s_{(k)}) + \mathbf{x}_{(k)}^T \mathbf{A}^T \mathbf{P} \boldsymbol{\xi}_{(k)} \\ & + \mathbf{B}_{(k)}^T \mathbf{P} \mathbf{A} \mathbf{x}_{(k)} \text{sign}(s_{(k)}) + \mathbf{B}_{(k)}^T \mathbf{P} \mathbf{B}_{(k)} + \mathbf{B}_{(k)}^T \mathbf{P} \boldsymbol{\xi}_{(k)} \text{sign}(s_{(k)}) \\ & + \boldsymbol{\xi}_{(k)}^T \mathbf{P} \mathbf{A} \mathbf{x}_{(k)} + \boldsymbol{\xi}_{(k)}^T \mathbf{P} \mathbf{B}_{(k)} \text{sign}(s_{(k)}) + \boldsymbol{\xi}_{(k)}^T \mathbf{P} \boldsymbol{\xi}_{(k)}. \end{aligned} \quad (4.17)$$

Using the Λ inequality (POZNYAK, 2010),

$$\mathbf{X}^T \mathbf{Y} + \mathbf{Y}^T \mathbf{X} \leq \mathbf{X}^T \boldsymbol{\Lambda} \mathbf{X} + \mathbf{Y}^T \boldsymbol{\Lambda}^{-1} \mathbf{Y}, \quad (4.18)$$

allows for the following terms to be obtained

$$\mathbf{x}_{(k)}^T \mathbf{A}^T \mathbf{P} \mathbf{B}_{(k)} \text{sign}(s_{(k)}) + \mathbf{B}_{(k)}^T \mathbf{P} \mathbf{A} \mathbf{x}_{(k)} \text{sign}(s_{(k)}) \leq \mathbf{x}_{(k)}^T \mathbf{A}^T \mathbf{P} \boldsymbol{\Lambda}_1 \mathbf{P} \mathbf{A} \mathbf{x}_{(k)} + \mathbf{B}_{(k)}^T \boldsymbol{\Lambda}_1^{-1} \mathbf{B}_{(k)} \quad (4.19)$$

$$\mathbf{x}_{(k)}^T \mathbf{A}^T \mathbf{P} \boldsymbol{\xi}_{(k)} + \boldsymbol{\xi}_{(k)}^T \mathbf{P} \mathbf{A} \mathbf{x}_{(k)} \leq \mathbf{x}_{(k)}^T \mathbf{A}^T \mathbf{P} \boldsymbol{\Lambda}_2 \mathbf{P} \mathbf{A} \mathbf{x}_{(k)} + \boldsymbol{\xi}_{(k)}^T \boldsymbol{\Lambda}_2^{-1} \boldsymbol{\xi}_{(k)} \quad (4.20)$$

$$\mathbf{B}_{(k)}^T \mathbf{P} \boldsymbol{\xi}_{(k)} \text{sign}(s_{(k)}) + \boldsymbol{\xi}_{(k)}^T \mathbf{P} \mathbf{B}_{(k)} \text{sign}(s_{(k)}) \leq \boldsymbol{\xi}_{(k)}^T \mathbf{P} \boldsymbol{\Lambda}_3 \mathbf{P} \boldsymbol{\xi}_{(k)} + \mathbf{B}_{(k)}^T \boldsymbol{\Lambda}_3^{-1} \mathbf{B}_{(k)} \quad (4.21)$$

where $\boldsymbol{\Lambda}_1 = \boldsymbol{\Lambda}_1^T > 0$, $\boldsymbol{\Lambda}_2 = \boldsymbol{\Lambda}_2^T > 0$ and $\boldsymbol{\Lambda}_3 = \boldsymbol{\Lambda}_3^T > 0$.

Then, substituting (4.19), (4.20) and (4.21) in (4.17) results

$$\begin{aligned} \Delta V_{(k)} \leq & \mathbf{x}_{(k)}^T \left(\mathbf{A}^T \mathbf{P} \mathbf{A} - \mathbf{P} \right) \mathbf{x}_{(k)} + \mathbf{x}_{(k)}^T \mathbf{A}^T \mathbf{P} \boldsymbol{\Lambda}_1 \mathbf{P} \mathbf{A} \mathbf{x}_{(k)} + \mathbf{B}_{(k)}^T \boldsymbol{\Lambda}_1^{-1} \mathbf{B}_{(k)} \\ & + \mathbf{x}_{(k)}^T \mathbf{A}^T \mathbf{P} \boldsymbol{\Lambda}_2 \mathbf{P} \mathbf{A} \mathbf{x}_{(k)} + \boldsymbol{\xi}_{(k)}^T \boldsymbol{\Lambda}_2^{-1} \boldsymbol{\xi}_{(k)} + \boldsymbol{\xi}_{(k)}^T \mathbf{P} \boldsymbol{\Lambda}_3 \mathbf{P} \boldsymbol{\xi}_{(k)} \\ & + \mathbf{B}_{(k)}^T \boldsymbol{\Lambda}_3^{-1} \mathbf{B}_{(k)} + \mathbf{B}_{(k)}^T \mathbf{P} \mathbf{B}_{(k)} + \boldsymbol{\xi}_{(k)}^T \mathbf{P} \boldsymbol{\xi}_{(k)} \end{aligned} \quad (4.22)$$

Equation (4.22) above can be rewritten as

$$\begin{aligned} \Delta V_{(k)} \leq & \mathbf{x}_{(k)}^T \left\{ \mathbf{A}^T \left[\mathbf{P} + \mathbf{P} (\boldsymbol{\Lambda}_1 + \boldsymbol{\Lambda}_2) \mathbf{P} \right] \mathbf{A} - \mathbf{P} \right\} \mathbf{x}_{(k)} \\ & + \mathbf{B}_{(k)}^T \left(\boldsymbol{\Lambda}_1^{-1} + \boldsymbol{\Lambda}_3^{-1} + \mathbf{P} \right) \mathbf{B}_{(k)} \\ & + \boldsymbol{\xi}_{(k)}^T \left(\boldsymbol{\Lambda}_2^{-1} + \mathbf{P} \boldsymbol{\Lambda}_3 \mathbf{P} + \mathbf{P} \right) \boldsymbol{\xi}_{(k)}. \end{aligned} \quad (4.23)$$

By adding and subtracting $\rho V_{(k)}$ to (4.23) and rearranging the terms results

$$\begin{aligned} \Delta V_{(k)} \leq & \mathbf{x}_{(k)}^T \left\{ \mathbf{A}^T [\mathbf{P} + \mathbf{P} (\boldsymbol{\Lambda}_1 + \boldsymbol{\Lambda}_2) \mathbf{P}] \mathbf{A} - (1 - \rho) \mathbf{P} \right\} \mathbf{x}_{(k)} \\ & + \mathbf{B}_{(k)}^T (\boldsymbol{\Lambda}_1^{-1} + \boldsymbol{\Lambda}_3^{-1} + \mathbf{P}) \mathbf{B}_{(k)} \\ & + \boldsymbol{\xi}_{(k)}^T (\boldsymbol{\Lambda}_2^{-1} + \mathbf{P} \boldsymbol{\Lambda}_3 \mathbf{P} + \mathbf{P}) \boldsymbol{\xi}_{(k)} - \rho V_{(k)} \end{aligned} \quad (4.24)$$

where $0 < \rho < 1$.

If the LMI

$$\mathbf{A}^T [\mathbf{P} + \mathbf{P} (\boldsymbol{\Lambda}_1 + \boldsymbol{\Lambda}_2) \mathbf{P}] \mathbf{A} - (1 - \rho) \mathbf{P} = -\mathbf{Q} \quad (4.25)$$

is feasible for a given $\mathbf{Q} = \mathbf{Q}^T > 0$, the inequality (4.24) can be rewritten as

$$\begin{aligned} \Delta V_{(k)} \leq & -\mathbf{x}_{(k)}^T \mathbf{Q} \mathbf{x}_{(k)} + \mathbf{B}_{(k)}^T (\boldsymbol{\Lambda}_1^{-1} + \boldsymbol{\Lambda}_3^{-1} + \mathbf{P}) \mathbf{B}_{(k)} \\ & + \boldsymbol{\xi}_{(k)}^T (\boldsymbol{\Lambda}_2^{-1} + \mathbf{P} \boldsymbol{\Lambda}_3 \mathbf{P} + \mathbf{P}) \boldsymbol{\xi}_{(k)} - \rho V_{(k)}. \end{aligned} \quad (4.26)$$

Equation (4.26) can be presented as

$$\Delta V_{(k)} \leq -\mathbf{x}_{(k)}^T \mathbf{Q} \mathbf{x}_{(k)} + \mathbf{B}_{(k)}^T \mathbf{Z} \mathbf{B}_{(k)} + \boldsymbol{\xi}_{(k)}^T \mathbf{H} \boldsymbol{\xi}_{(k)} - \rho V_{(k)} \quad (4.27)$$

where $\mathbf{Z} = \boldsymbol{\Lambda}_1^{-1} + \boldsymbol{\Lambda}_3^{-1} + \mathbf{P}$ and $\mathbf{H} = \boldsymbol{\Lambda}_2^{-1} + \mathbf{P} \boldsymbol{\Lambda}_3 \mathbf{P} + \mathbf{P}$, with $\mathbf{Z} = \mathbf{Z}^T > 0$ and $\mathbf{H} = \mathbf{H}^T > 0$.

Considering the following definitions

$$\mathbf{x}_{(k)}^T \mathbf{Q} \mathbf{x}_{(k)} = \|\mathbf{x}_{(k)}\|_{\mathbf{Q}}^2, \quad \mathbf{B}_{(k)}^T \mathbf{Z} \mathbf{B}_{(k)} = \|\mathbf{B}_{(k)}\|_{\mathbf{Z}}^2, \quad \boldsymbol{\xi}_{(k)}^T \mathbf{H} \boldsymbol{\xi}_{(k)} = \|\boldsymbol{\xi}_{(k)}\|_{\mathbf{H}}^2 \quad (4.28)$$

the following inequalities can be derived

$$\begin{aligned} \lambda_{\min}(\mathbf{Q}) \|\mathbf{x}_{(k)}\|^2 & \leq \|\mathbf{x}_{(k)}\|_{\mathbf{Q}}^2 \leq \lambda_{\max}(\mathbf{Q}) \|\mathbf{x}_{(k)}\|^2 \\ \lambda_{\min}(\mathbf{Z}) \|\mathbf{B}_{(k)}\|^2 & \leq \|\mathbf{B}_{(k)}\|_{\mathbf{Z}}^2 \leq \lambda_{\max}(\mathbf{Z}) \|\mathbf{B}_{(k)}\|^2 \\ \lambda_{\min}(\mathbf{H}) \|\boldsymbol{\xi}_{(k)}\|^2 & \leq \|\boldsymbol{\xi}_{(k)}\|_{\mathbf{H}}^2 \leq \lambda_{\max}(\mathbf{H}) \|\boldsymbol{\xi}_{(k)}\|^2. \end{aligned} \quad (4.29)$$

Then, (4.27) can be rewritten as

$$\Delta V_{(k)} \leq -\lambda_{\min}(\mathbf{Q}) \|\mathbf{x}_{(k)}\|^2 + \lambda_{\max}(\mathbf{Z}) \|\mathbf{B}_{(k)}\|^2 + \lambda_{\max}(\mathbf{H}) \|\boldsymbol{\xi}_{(k)}\|^2 - \rho V_{(k)} \quad (4.30)$$

By expanding the terms $\|\mathbf{B}_{(k)}\|^2$ and $\|\boldsymbol{\xi}_{(k)}\|^2$ it results

$$\Delta V_{(k)} \leq -\lambda_{\min}(\mathbf{Q}) \|\mathbf{x}_{(k)}\|^2 + \lambda_{\max}(\mathbf{Z}) \left[k_1^2 |x_{1(k)}| + (k_2 T_s)^2 \right] + \lambda_{\max}(\mathbf{H}) \xi_{1(k)}^2 - \rho V_{(k)} \quad (4.31)$$

Given that $|x_{1(k)}| \leq \|\mathbf{x}_{(k)}\|$, (4.31) can be expressed as

$$\begin{aligned} \Delta V_{(k)} &\leq -\alpha_1 \|\mathbf{x}_{(k)}\|^2 + \alpha_2 \|\mathbf{x}_{(k)}\| + \alpha_3 - \rho V_{(k)} \\ &= -\left(\sqrt{\alpha_1} \|\mathbf{x}_{(k)}\| - \frac{\alpha_2}{2\sqrt{\alpha_1}}\right)^2 + \left(\frac{\alpha_2}{2\sqrt{\alpha_1}}\right)^2 + \alpha_3 - \rho V_{(k)} \end{aligned} \quad (4.32)$$

where $\alpha_1 = \lambda_{\min}(\mathbf{Q}) > 0$, $\alpha_2 = \lambda_{\max}(\mathbf{Z}) k_1^2$ and $\alpha_3 = \lambda_{\max}(\mathbf{Z}) (k_2 T_s)^2 + \lambda_{\max}(\mathbf{H}) \xi_{1(k)}^2$.

Then,

$$\Delta V_{(k)} \leq c - \rho V_{(k)} \quad (4.33)$$

where $c = \left(\frac{\alpha_2}{2\sqrt{\alpha_1}}\right)^2 + \alpha_3$.

Equation (4.33) can be expressed as

$$V_{(k+1)} \leq (1 - \rho) V_{(k)} + c \quad (4.34)$$

whose solution is given by

$$V_{(k)} \leq (1 - \rho)^k V_{(0)} + \sum_{i=0}^{k-1} (1 - \rho)^{k-1-i} c \quad (4.35)$$

and the upper limit can be calculated by

$$\lim_{k \rightarrow \infty} V_{(k)} \leq \frac{c}{\rho}. \quad (4.36)$$

Thus, the convergence radius of the controller is

$$r \leq \frac{c}{\rho} \quad (4.37)$$

□

In the following section, a gain design procedure for super-twisting sliding mode controllers will be proposed.

4.3 GAIN DESIGN PROCEDURE

The proper selection of a DTSTSM controller gains is necessary in order to guarantee acceptable performance and low chattering (GONZALEZ; MORENO; FRIDMAN, 2012). Due to the wide gain constraint intervals, traditional sliding mode control design is not an efficient approach. Moreover, for the SRM current control application, different sets of gains lead to different settling times and current ripple values. Generally, larger gains lead to faster settling times, however, they also tend to increase overshoot and current ripple. Smaller gains, on the other hand, present a slower response along with a lower current ripple. Given the highly non-linear behavior of the SRM, the use of analytical formulations to determine the controller gains becomes a complex task. Additionally, the back-EMF of the machine plays an important role, generally degrading the tracking capability of the controller at higher speeds (AHMAD; NARAYANAN, 2016).

In this context, an optimization-based design can be an interesting tool. Using an offline grid search algorithm allows several points of a defined search space to be evaluated, where a cost function is used to determine suitable controller gains, which present the best trade-off between reference tracking and low current ripple. Moreover, the performance of the controller can be improved by online gain adaptation, with respect to the rotor speed. In the following subsections, a novel gain design procedure for a DTSTSM controller and a design example are presented, respectively.

4.3.1 Design procedure

To guide the algorithm, a cost function, $F(k_1, k_2 T_s)$, is defined as the sum of the absolute value of the current tracking error,

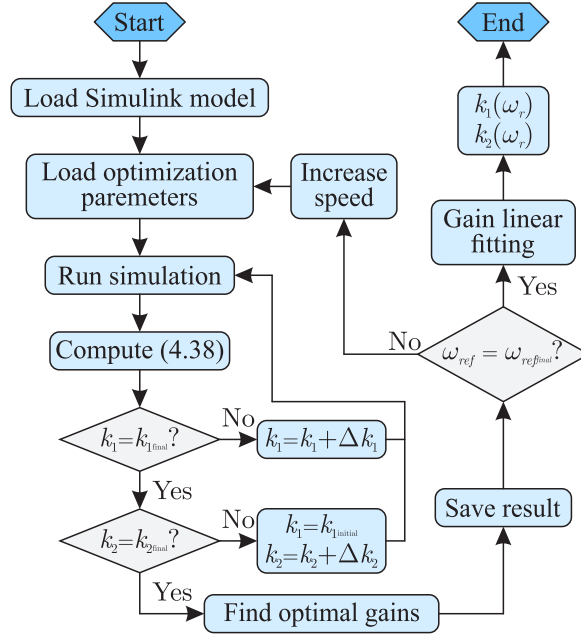
$$F(k_1, k_2 T_s) = \max \left(\sum_0^{\theta_{exc}} |s(k)| \right), \quad (4.38)$$

where θ_{exc} is the excitation period.

This choice is made as a means to find a set of gains that present good tracking capability, with both a fast transient response and low current ripple. Note that the cost function is calculated during the excitation interval, when the reference phase current is greater than zero.

The proposed design procedure is presented in Figure 4.3.

Figure 4.3 – Flowchart of the proposed gain design procedure.



Source: Author.

The procedure is performed offline and starts with the simulation model being loaded in Matlab/Simulink. Then, the optimization parameters are set, them being: the search space and the gain increments. Following this, the simulation procedure starts, where one simulation is performed for each pair of gains. At the end of each simulation, the cost function is calculated and the value is stored. Once every simulation has been executed, the gains that yielded the lowest cost function value are stored as the optimal gains for that particular speed. Following this, the reference speed is incremented and the procedure is repeated until the every desired speed value is evaluated. Lastly, a linear fitting is performed, where the optimal gains are fitted to a straight line, allowing simple digital implementation.

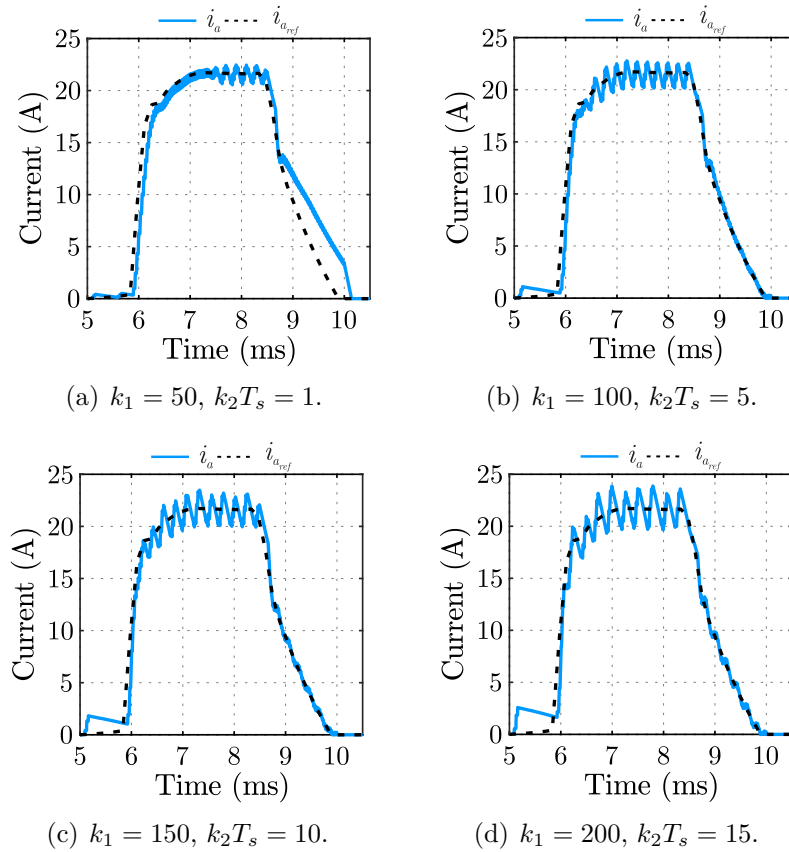
4.3.2 Design example

This subsection aims to present a gain design example for the a DTSTSM current controller using the proposed methodology, while also providing experimental validation in the following section.

For this example, SRM 2 is used, with the parameters shown in Table 2.2 and Figure 2.15, using the SRM model depicted in the end of Chapter 2. The sampling and switching frequencies are set to 30 kHz, and a pulse-width modulation with triangular carrier is used. The reference phase currents are generated according to the TSF presented

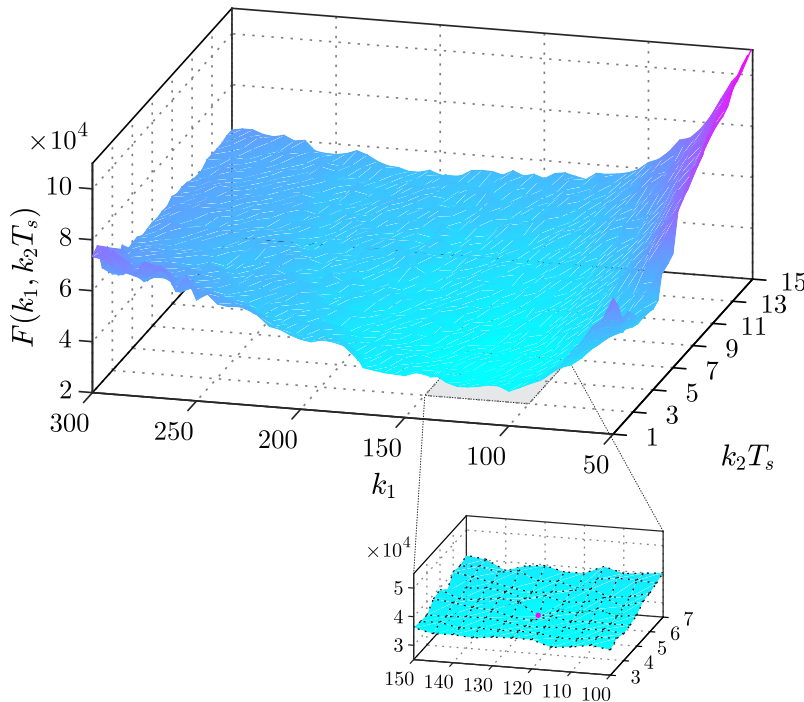
in (LI; BILGIN; EMADI, 2019). In this case, the search space was defined as $50 \leq k_1 \leq 300$, evaluated at $\Delta k_1 = 5$ increments and $1 \leq k_2 T_s \leq 15$, evaluated at $\Delta k_2 T_s = 0.5$ increments. Simulations are performed for every gain combination inside the interval. In order to show the effects of different gain combinations, Figure 4.4 presents simulation results for four different sets of gains at a speed of 1000 r/min. Note how different gains affect tracking capability and current ripple. The cost function values for the entire search space at the same speed are presented on Figure 4.5. In this case, the gains that yielded the best performance (i.e., minimize the cost function) are $k_1 = 125$ and $k_2 T_s = 5$. The phase current and cost function waveforms for this set of gains, at a speed of 1000 r/min, are presented in Figure 4.6.

Figure 4.4 – Simulation results for different gain combinations at 1000 r/min with a 6 Nm load.



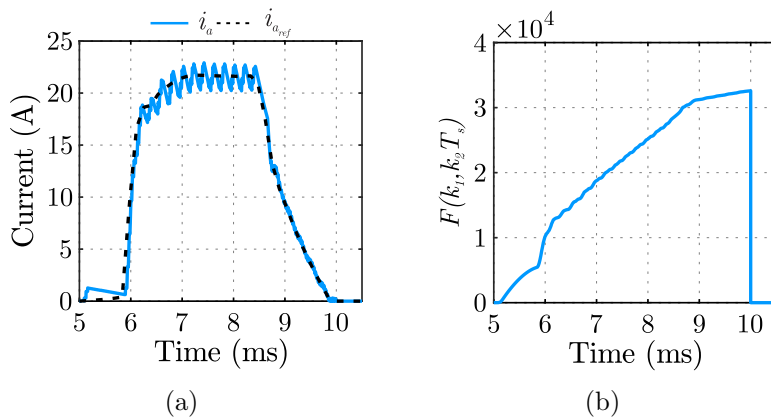
Source: Author.

Figure 4.5 – Cost function values at a speed of 1000 r/min, highlighting the region of the search space containing the optimal gain combination.



Source: Author.

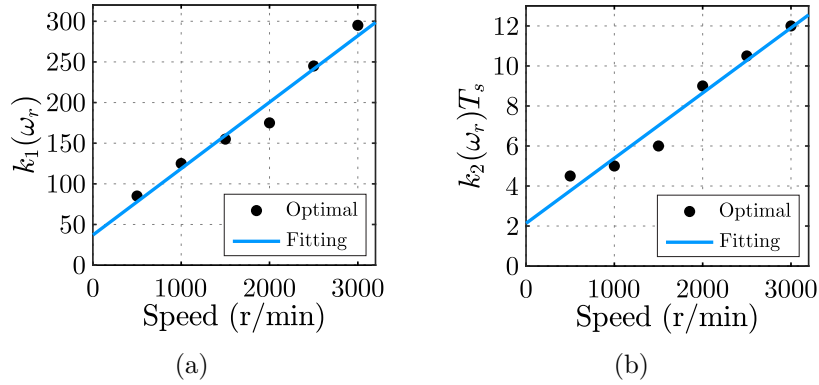
Figure 4.6 – Simulation results for the optimal gains at a speed of 1000 r/min. (a) Phase current. (b) Cost function.



Source: Author.

Given that the performance of the controller can be enhanced by gain adjustment, the procedure is repeated in 500 r/min increments, until reaching the speed of 3000 r/min. After that, a linear fitting of the resulting gains is performed, allowing for simple implementation. The optimal results as well as the linear regression are presented in Figure 4.7.

Figure 4.7 – Optimal gains for the proposed DTSTSM controller as a function of speed. (a) k_1 . (b) $k_2 T_s$.



Source: Author.

For digital implementation, gains k_1 and $k_2 T_s$ are calculated according to (4.39) and (4.40), respectively.

$$k_1(\omega_r) = 0.08171 |\omega_r| + 37 \quad (4.39)$$

$$k_2(\omega_r) T_s = 0.003257 |\omega_r| + 2.133 \quad (4.40)$$

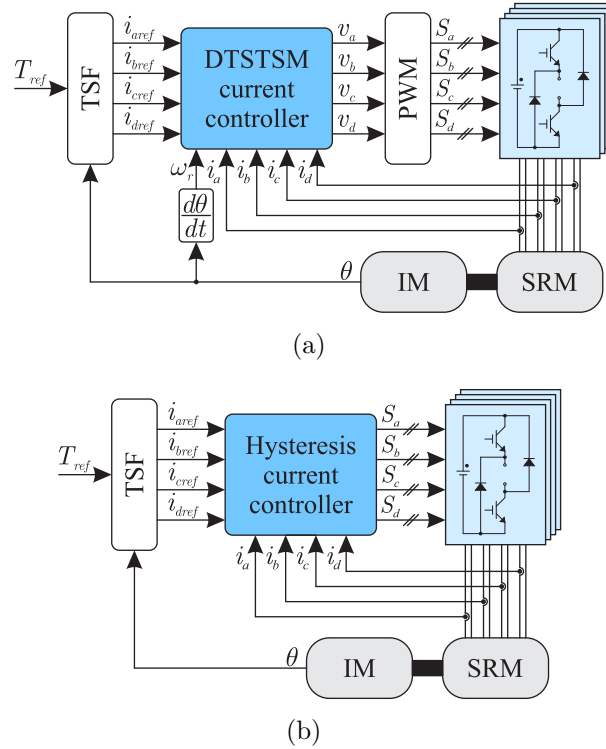
It is important to highlight that the proposed design procedure is carried out offline, not demanding any sort of online tuning. In addition, it must be pointed out that the gains obtained by simulation results are directly used for experimental validation, not requiring any additional design steps. Lastly, note that multiple load values are not considered in the gain design procedure. This is done as a means to maintain a simple controller structure, avoiding the use of lookup tables during implementation and ensuring a faster design stage. Moreover, given the robustness of the DTSTSM controller, the above-mentioned are reasonable design choices.

4.4 EXPERIMENTAL RESULTS

In this section experimental tests are conducted in order to verify the effectiveness of the proposed DTSTSM current controller. The characteristics of the SRM used, SRM 2, are presented in Figure 2.15, while additional parameters of the machine are given in Table 2.2. The setup is composed of an SRM, a four-phase AHB converter and an induction machine (IM), coupled to the SRM. The load torque is imposed by the IM, which operates as a generator, while the SRM is controlled with predetermined current references (FANG et al., 2021c). For additional details, refer to Appendix C.

Figure 4.8 (a) shows the block diagram of the proposed current control structure. A DSP TMS320F28335 is used for digital implementation. The sampling and switching frequencies are set to $f_s = f_{sw} = 30$ kHz, and a pulse-width modulation with triangular carrier is used. The duty cycle used in the PWM is given by $v_{(k)}/V_{dc}$ in soft chopping mode and by $0.5 + 0.5 (v_{(k)}/V_{dc})$ in hard chopping mode, where V_{dc} is the DC bus voltage (PENG; YE; EMADI, 2016). The process is depicted in Figure 4.9. Soft chopping is applied while $\theta < \theta_{off}$, while hard chopping is used after $\theta > \theta_{off}$, with the turn-off angles being stored in a lookup table. Analogous reasoning is used for hysteresis current control.

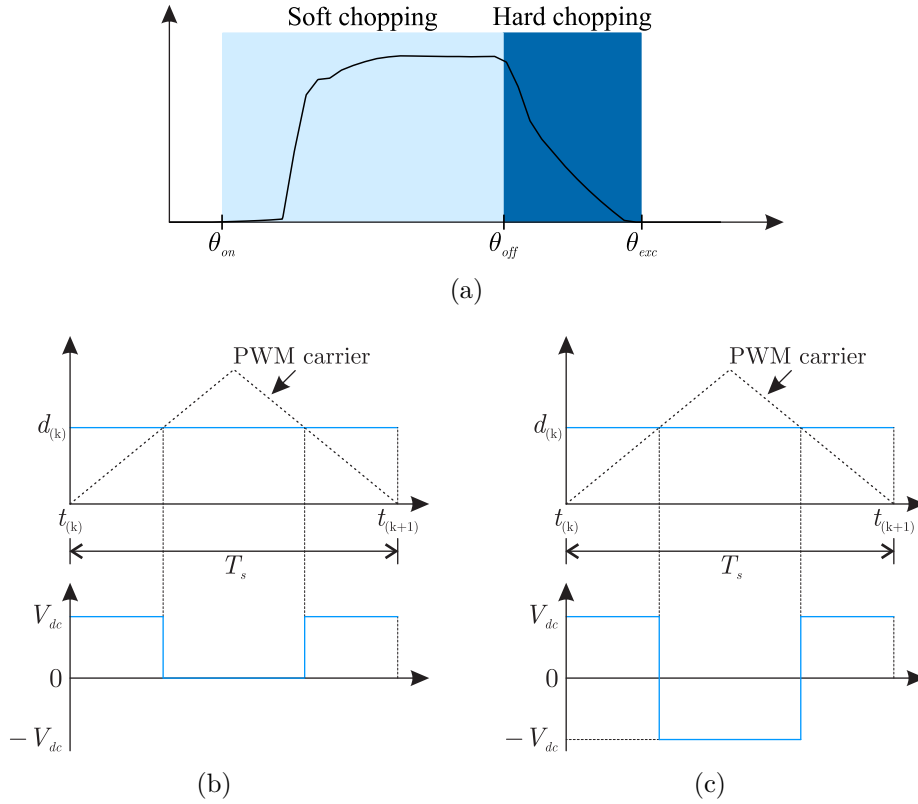
Figure 4.8 – Block diagram of the current control strategies. (a) DTSTSM controller. (b) Hysteresis controller.



Source: Author.

The reference phase currents are generated according to the TSF presented in (LI; BILGIN; EMADI, 2019). For digital implementation, the DTSTSM controller gains are calculated according to (4.39) and (4.40). For comparison purposes, hysteresis current control with a hysteresis band of 1 A was applied to the same SRM, as depicted in Figure 4.8 (b). The band has been set based on the characteristics of the SRM drive (BILGIN; JIANG; EMADI, 2019). Note that different values can be considered, which will in turn affect the dynamic performance of the strategy. The sampling frequency was set to 57 kHz, the highest achievable value considering the limited performance of the DSP used (FANG et al., 2021c). The higher value when compared to the DTSTSM controller is

Figure 4.9 – PWM characteristics. (a) Current reference example with chopping regions highlighted. (b) Soft chopping waveforms. (c) Hard chopping waveforms.



Source: Author.

chosen purposefully, allowing for a comparable performance with the proposed controller (YE; MALYSZ; EMADI, 2015). Due to digital implementation, the hysteresis controller also presents a one sample delay.

As a means to measure the tracking capability and current ripple of the proposed controller, which directly affect the torque ripple characteristic of the SRM, measurements of the current and torque root-mean-square errors (RMSE) are performed (YE; MALYSZ; EMADI, 2015; TAYLOR et al., 2020). The current and torque RMSE are defined as, respectively,

$$i_{RMSE} = \sqrt{\frac{1}{N} \sum_{n=1}^N (i_{ref}(k) - i(k))^2}, \quad (4.41)$$

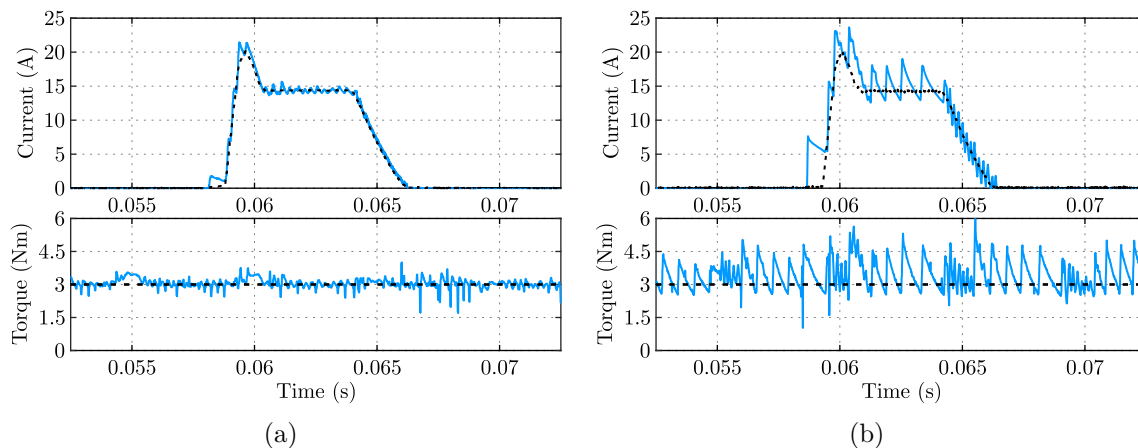
$$T_{RMSE} = \sqrt{\frac{1}{N} \sum_{n=1}^N (T_{ref}(k) - T_e(k))^2}, \quad (4.42)$$

where N is the number of data points.

4.4.1 Steady state performance

Figure 4.10 shows experimental results for the proposed DTSTSM and hysteresis controllers under a 3 Nm load at a speed of 500 r/min. A 12-bit digital to analog converter is used to measure the reference current and instantaneous torque waveforms, with the latter making use of a lookup table containing characteristics of the studied SRM. It can be observed that the proposal presents a fast transient response as well as adequate reference tracking. The robustness of the proposal can also be observed, as it operates properly in the region of magnetic saturation. When compared to the hysteresis controller, significantly lower current and torque ripple are observed, while using close to a 50% smaller sampling frequency.

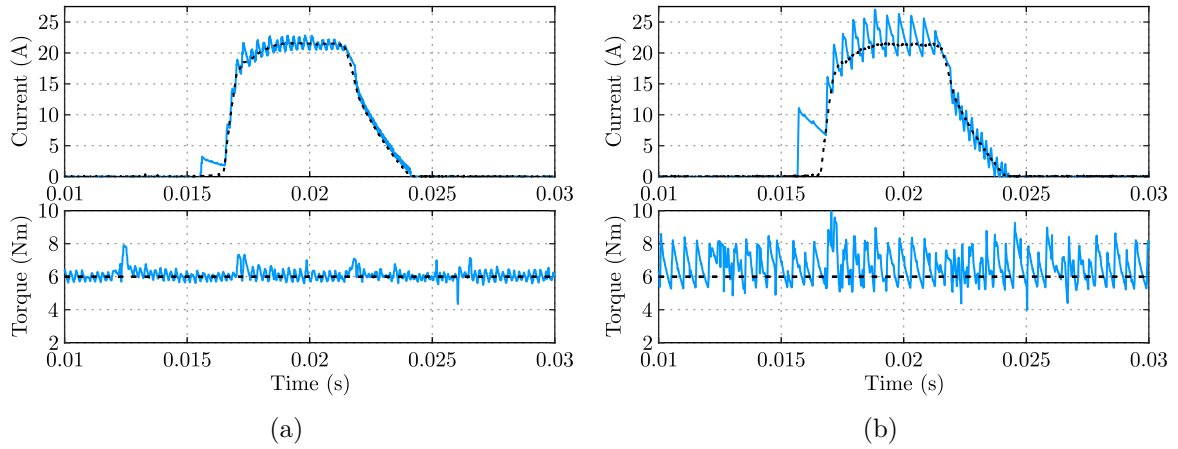
Figure 4.10 – Experimental results for a speed of 500 r/min and a 3 Nm load. (a) DTSTSM controller ($f_s = 30$ kHz). (b) Hysteresis controller ($f_s = 57$ kHz).



Source: Author.

In order to verify the robustness of the controller to different load levels, Figure 4.11 presents the experimental results for the proposed DTSTSM and hysteresis controllers under a 6 Nm load, still at a speed of 500 r/min. Once more, the proposal presents suitable tracking along with reduced current ripple. In addition, it can be seen that the controller is able to maintain the expected behavior for different load conditions, while making use of the same gains.

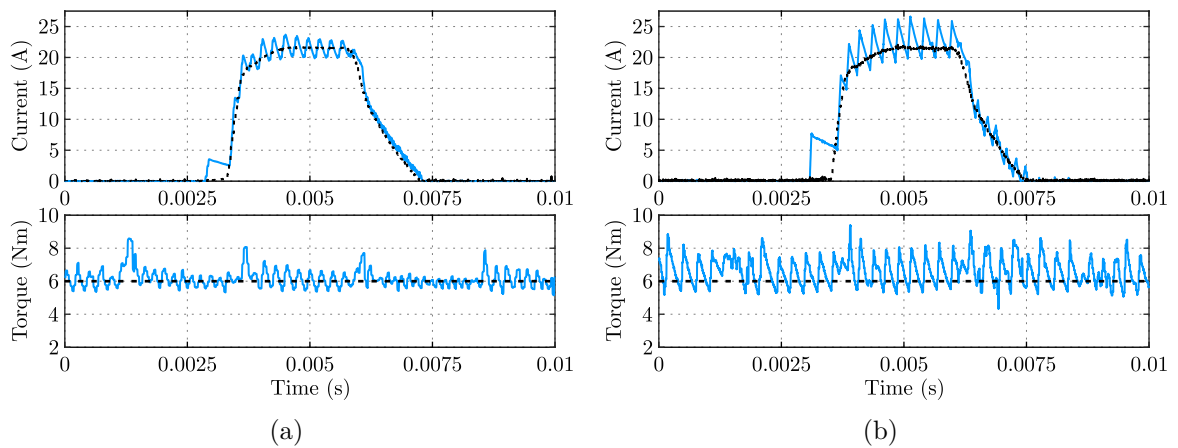
Figure 4.11 – Experimental results for a speed of 500 r/min and a 6 Nm load. (a) DTSTSM controller ($f_s = 30$ kHz). (b) Hysteresis controller ($f_s = 57$ kHz).



Source: Author.

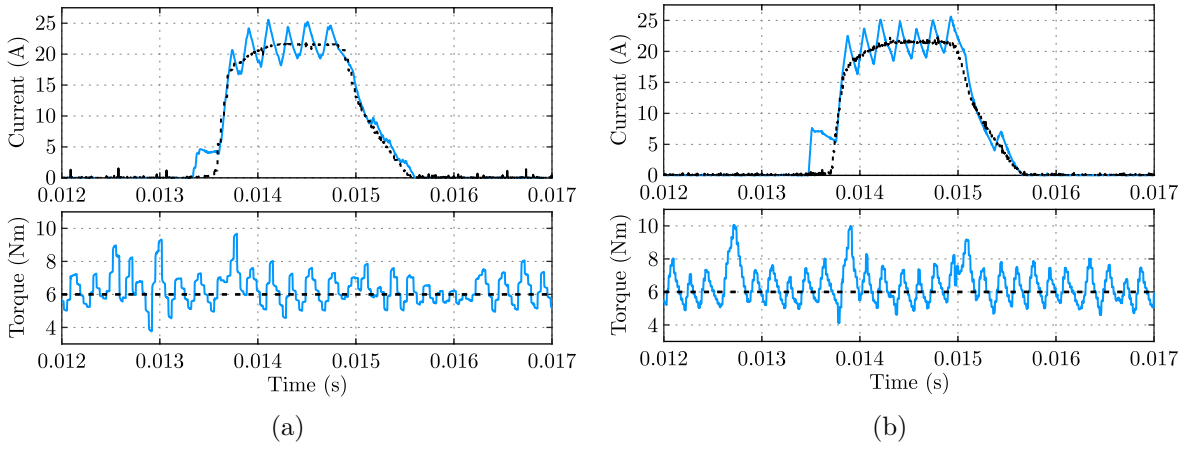
In order to evaluate the performance of the controllers at different speeds, experimental results for both controllers under a 6 Nm load at the speeds of 1000, 2000 and 3000 r/min are presented in Figs. 4.12, 4.13 and 4.14, respectively. It can be seen that the proposal presents good reference tracking even at higher speeds. As an example, it can be seen that at 3000 r/min the DTSTSM is able to present comparable tracking to the hysteresis controller, while making use of reduced sampling rate and guaranteeing a fixed switching frequency.

Figure 4.12 – Experimental results for a speed of 1000 r/min and a 6 Nm load. (a) DTSTSM controller ($f_s = 30$ kHz). (b) Hysteresis controller ($f_s = 57$ kHz).



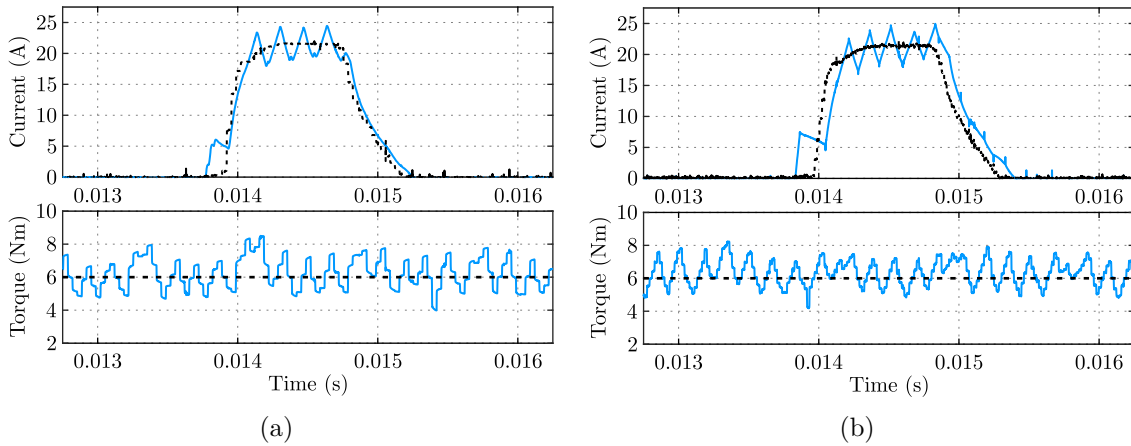
Source: Author.

Figure 4.13 – Experimental results for a speed of 2000 r/min and a 6 Nm load. (a) DT-STSM controller ($f_s = 30$ kHz). (b) Hysteresis controller ($f_s = 57$ kHz).



Source: Author.

Figure 4.14 – Experimental results for a speed of 3000 r/min and a 6 Nm load. (a) DT-STSM controller ($f_s = 30$ kHz). (b) Hysteresis controller ($f_s = 57$ kHz).



Source: Author.

A comprehensive quantitative analysis is shown in Tables 4.1 and 4.2, where measurements of current and torque RMSE are presented for both controllers under a 3 Nm and 6 Nm load, respectively. The tests are carried out at the speeds of 500, 1000, 2000 and 3000 r/min.

Table 4.1 – Comparison of the DTSTSM and hysteresis current controllers for a 3 Nm load.

Speed (r/min)	DTSTSM controller		Hysteresis controller	
	i_{RMSE} (A)	T_{RMSE} (Nm)	i_{RMSE} (A)	T_{RMSE} (Nm)
500	0.4567	0.2252	1.6515	0.7859
1000	0.6356	0.3015	1.7522	0.6859
2000	1.1098	0.6016	1.4706	0.6502
3000	1.5780	1.0626	1.9762	0.8626

Table 4.2 – Comparison of the DTSTSM and hysteresis current controllers for a 6 Nm load.

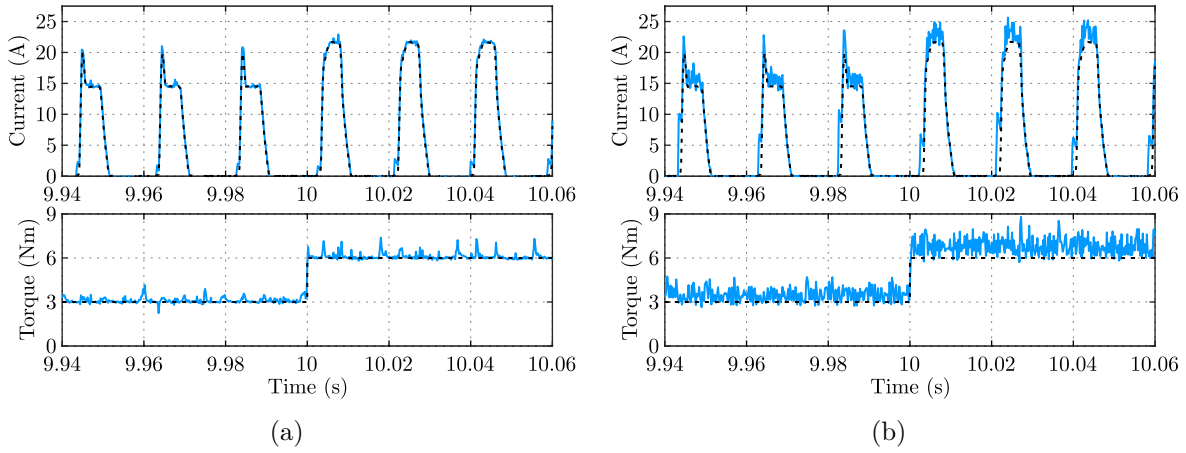
Speed (r/min)	DTSTSM controller		Hysteresis controller	
	i_{RMSE} (A)	T_{RMSE} (Nm)	i_{RMSE} (A)	T_{RMSE} (Nm)
500	0.7191	0.3524	2.3321	1.1198
1000	0.9427	0.5488	2.0863	1.0270
2000	1.3433	0.9811	1.8360	1.0978
3000	1.5577	0.9820	2.5513	0.8511

As seen in Tables 4.1 and 4.2, the proposed controller presents smaller current and torque RMSE values across the evaluated speed range when compared to hysteresis control. It should be noted that with the increase in speed, and consequently back-EMF, the response of the hysteresis controller improves, however, the DTSTSM controller is still able to present a comparable performance at the speed of 3000 r/min. Moreover, the proposal has the benefit of ensuring a fixed switching frequency while also making use of a significantly lower sampling rate.

4.4.2 Dynamic performance

As a means to further evaluate the proposal, dynamics tests are carried out. First, to evaluate the robustness to load disturbances, Figure 4.15 shows experimental results of a dynamic load test for the proposed DTSTSM and hysteresis controllers, at a speed of 500 r/min. Initially, the motor operates under a 3 Nm load, and at $t = 10$ s the load is increased to 6 Nm.

Figure 4.15 – Experimental results for a dynamic load condition, at a speed of 500 r/min.
(a) DTSTSM controller ($f_s=30$ kHz). (b) Hysteresis controller ($f_s=57$ kHz).



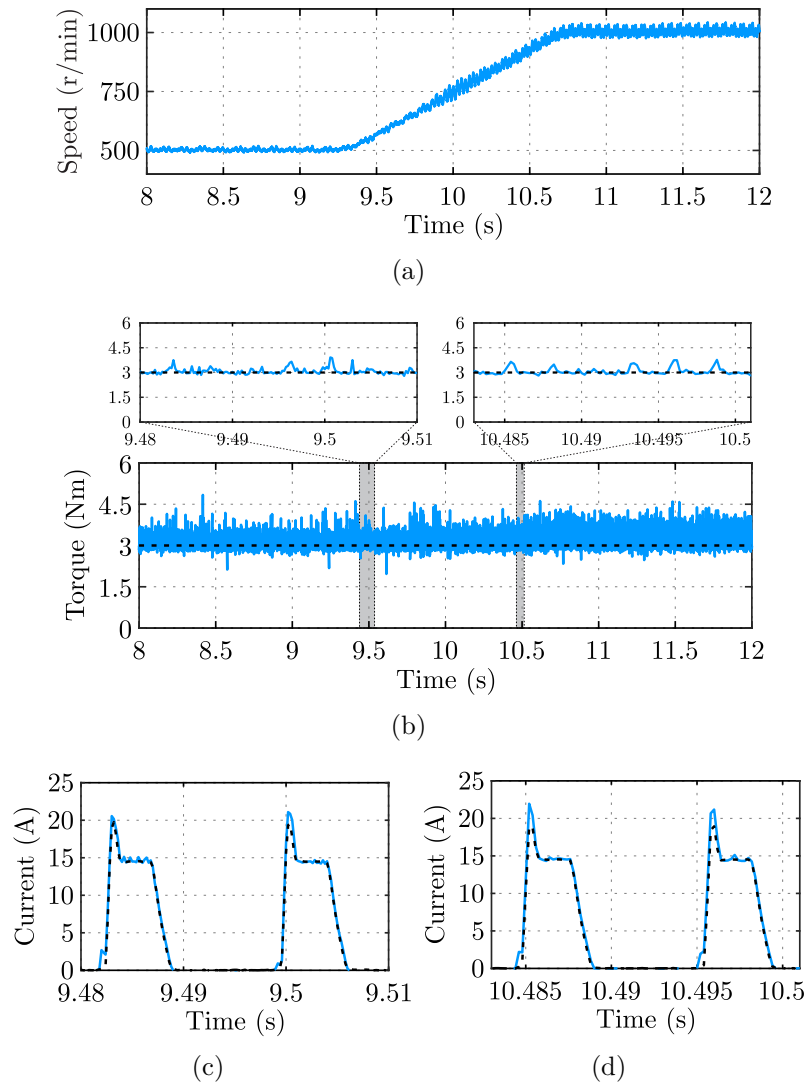
Source: Author.

It can be observed that the proposal presents a fast transient response as well as good disturbance rejection. Similarly to the steady state results, significantly lower current and torque ripple are observed when compared to the hysteresis controller, while using approximately half the sampling frequency.

In order to test the performance in variable speed conditions, a dynamic speed test for the proposed DTSTSM and hysteresis controllers is presented in Figure 4.16. The motor is initially controlled to 500 r/min, and then the speed is increased in a ramp until reaching 1000 r/min, under a 3 Nm load.

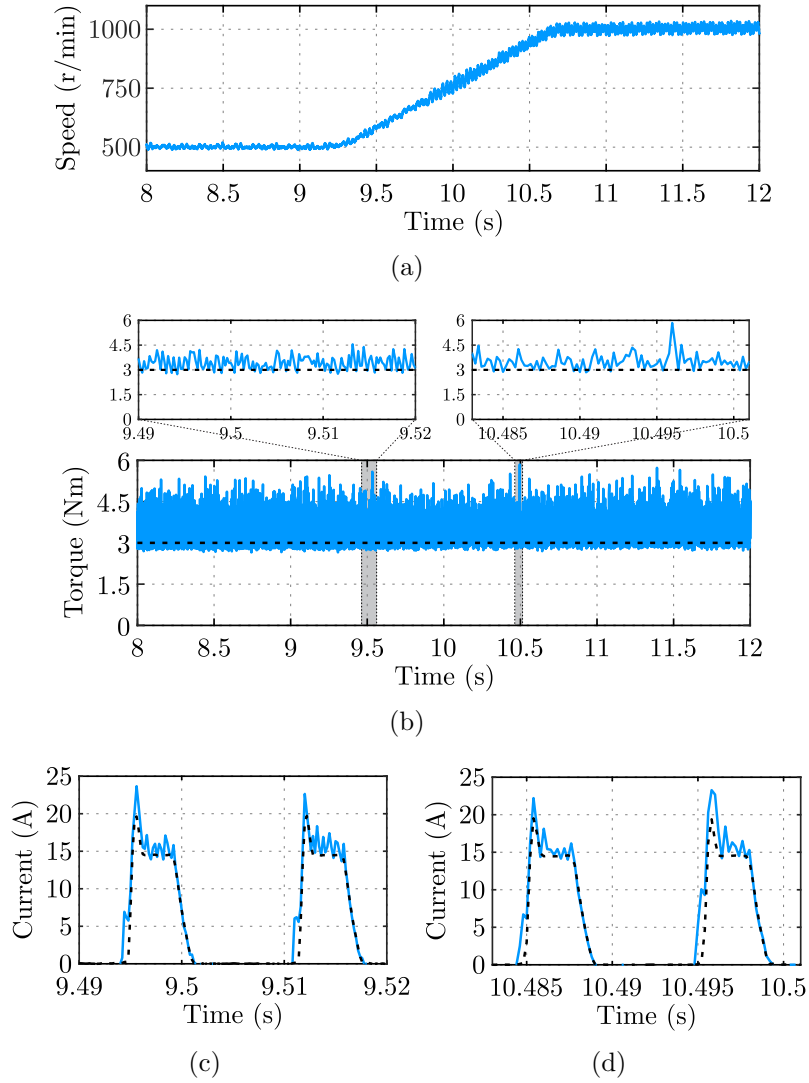
It is observed that the proposal presents suitable reference current and torque tracking throughout the test, including the speed variation period. Again, reduced current and torque ripple are verified when compared to the hysteresis controller.

Figure 4.16 – Experimental results for the DTSTSM controller ($f_s = 30$ kHz) in a variable speed condition, under a 3 Nm load. (a) Rotor speed. (b) Torque. (c) Phase current highlight 1. (d) Phase current highlight 2.



Source: Author.

Figure 4.17 – Experimental results for the Hysteresis controller ($f_s = 57$ kHz) in a variable speed condition, under a 3 Nm load. (a) Rotor speed. (b) Torque. (c) Phase current highlight 1. (d) Phase current highlight 2.



Source: Author.

4.4.3 Efficiency comparison

In order to further evaluate the proposal, an efficiency comparison is carried out. The efficiency, η , is calculated as,

$$\eta = \frac{P_{out}}{P_{in}} \quad (4.43)$$

where P_{in} is the input power and P_{out} is the output power.

The input power is defined as,

$$P_{in} = V_{dc}i_{avg} \quad (4.44)$$

where i_{avg} is the average DC bus current.

The output power is defined as,

$$P_{out} = \omega_r T_{avg} \quad (4.45)$$

where T_{avg} is the average electromagnetic torque.

The efficiency results for both controllers in the operating conditions of the steady state tests is presented in Table 4.3. Moreover, the RMS current values are given in Table 4.4. The switching frequency value for the hysteresis controller varies from $f_{sw} = 1-22$ kHz. The proposal, as previously mentioned, presents a fixed switching frequency of $f_{sw} = 30$ kHz.

Table 4.3 – Efficiency comparison of the DTSTSM and hysteresis current controllers.

Speed (r/min)	3 Nm		6 Nm	
	DTSTSM controller	Hysteresis controller	DTSTSM controller	Hysteresis controller
500	47.73%	51.12%	57.79%	57.81%
1000	57.36%	62.71%	67.40%	68.27%
2000	68.84%	70.59%	75.25%	75.55%
3000	73.21%	73.94%	79.05%	79.09%

Table 4.4 – RMS current comparison of the DTSTSM and hysteresis current controllers.

Speed (r/min)	3 Nm		6 Nm	
	DTSTSM controller	Hysteresis controller	DTSTSM controller	Hysteresis controller
500	8.4791 A	9.0857 A	11.5301 A	12.3963 A
1000	8.6429 A	9.1585 A	11.4211 A	12.1394 A
2000	8.8416 A	8.8331 A	11.3540 A	11.8267 A
3000	8.7602 A	8.6766 A	11.4554 A	11.6424 A

It can be seen that the DTSTSM controller presents a slightly lower efficiency, when compared to the hysteresis controller. From Table 4.4, it can be observed that the proposal has overall lower RMS current values, leading to smaller copper losses. However, due to the increased switching frequency of the DTSTSM controller, the switching losses of the proposed controller are higher, leading to a slightly smaller system efficiency, more evident in the lower speed range.

4.4.4 Computational burden comparison

In order to evaluate the computational complexity of both controllers, a measurement of the execution time of the control algorithm is presented in Table 4.5. The measure takes into consideration the torque sharing as well as the current controller, with both of the controllers being tested in the same hardware and without any code optimizations. Note that only the resulting current reference waveforms from (LI; BILGIN; EMADI, 2019) are stored in the DSP, with the cumbersome reference current generation process being carried out entirely offline. It can be observed that the DTSTSM proposal presents an execution time very similar to the hysteresis approach, meaning it presents comparable computational complexity and showing that it could be used in low cost microcontrollers available in industry and product oriented applications.

Table 4.5 – Comparison of the execution time of the control algorithms.

Algorithm	DTSTSM	Hysteresis
Total execution time	18.44 μ s	17.32 μ s

4.5 CONCLUSION

In this Chapter, a discrete-time super-twisting sliding mode current control scheme for switched reluctance motors is proposed. The proposal is implemented via PWM, ensuring a fixed switching frequency, while maintaining a simple structure, not requiring any knowledge of the machine parameters on implementation. A novel procedure for gain design is described, using a cost function to determine gains which ensure good tracking capability, allowing a systematic and straightforward design stage. The procedure is repeated for different speed values, allowing for a variable gain structure, where the gains are adjusted during operation based on the rotor speed. The control strategy is developed in discrete-time and the stability analysis is carried out considering the digital control implementation delay, by means of Lyapunov analysis. Experimental results show that the proposal has a comparable performance to a traditional hysteresis controller, while

using a significantly lower sampling frequency and ensuring a fixed switching frequency. Moreover, current and torque RMSE measurements attest to the good performance of the controller, showing a superior tracking performance especially at the lower speed range. Lastly, the proposed controller presents similar computational complexity to the hysteresis approach, making it a viable candidate for low cost microcontrollers present in industry and product oriented applications.

5 CONCLUSIONS AND PERSPECTIVES

5.1 FINAL CONSIDERATIONS

This thesis presents contributions in the field of advanced control strategies for SRMs. These techniques seek to improve the performance of SRMs, specially regarding torque ripple minimization, aiming to mitigate a known drawback of the machine.

Chapter 2 presents the fundamental concepts related to the operation of SRM drives. Topics such as the constructive characteristics of SRMs, focusing on the double salient structure, and the machine's typical inductance profile are shown. The converter used to drive the machine is presented, detailing the operating stages and demonstrating how they affect the motor during operation. In addition, current and single pulse control techniques are also presented. Modeling of the machine is shown, along with the simulation model, where machine data are used to represent the dynamic behavior of the SRM. From the fundamentals, the main advantages of the machine are verified. On the other hand, the main drawbacks are also observed, specially the inherent high torque ripple of the machine.

The PSO-based firing angle optimization procedure, presented in Chapter 3, enables the motor to operate in an optimal region based only on the speed of the machine. Through the proposed cost function, the performance is optimized with a trade-off between low torque ripple and high energy efficiency. The use of the PSO algorithm allows the computational effort of the procedure to be significantly reduced, without affecting the quality of the results. A load sensitivity analysis shows that when operating under different load conditions the system operates in a sub-optimal region for certain load values. Such result was expected, given that load torque was not considered in the optimization process. Although it can be observed that the proposed control strategy is able to effectively reduce torque ripple in SRMs, it should be noted that these techniques have limitations and that the resulting torque characteristic can still be improved by making use of techniques such as torque sharing functions, for example. However, these techniques rely on accurate current controllers.

In this context, a discrete-time super-twisting sliding mode current control scheme for switched reluctance motors, proposed in Chapter 4, presents improved reference current tracking, with fast dynamic responses and low current ripple. Moreover, the strategy ensures a fixed switching frequency due to the use of PWM, while maintaining a simple structure, not requiring any knowledge of the machine parameters on implementation. Theoretical stability analysis is carried out considering the digital implementation delay, resulting in an original stability analysis. As a solution to the complex task of gain design

of super-twisting controllers, an additional contribution of this thesis, a novel gain design procedure is described, making use of an optimization-based approach to determine gains which ensure good tracking capability, allowing an automatic, systematic and straightforward design stage. The procedure is repeated for different speed conditions, enabling a variable gain structure, adjusted during operation according to rotor speed. Experimental results show that the DTSTSM proposal has a comparable performance to the traditional hysteresis controller in both steady state and dynamic situations. This is achieved while making use of a notably lower sampling frequency and ensuring a fixed switching frequency. Measurements of current and torque RMSE are used to demonstrate the good performance of the DTSTSM controller, showing a superior tracking performance at the lower speed range. Lastly, similar computational complexity to the hysteresis approach is observed, making the DTSTSM controller a viable candidate for low cost microcontrollers present in industry and product oriented applications.

Thus, it was proved that the advanced control strategies proposed in this thesis are able to improve the performance of SRMs, being competitive with other control schemes described in the literature.

Lastly, Appendices A to C provide additional contributions as well as support for this thesis.

5.2 FUTURE WORK

From this Thesis, several future work topics can be explored.

Regarding Chapter 3, weighting factors should be considered in the cost function in order to ensure a balance between different metrics, such as the ones mentioned in this thesis. Moreover, the procedure can be extended to consider different speed and load conditions, ensuring optimal performance. In addition, the proposed firing angle optimization procedure can be applied to SRGs in wind power applications, for example. Just like SRMs, the optimal firing angles are also influenced by the load connected to the SRG. However, due to the nature of wind energy conversion systems, an optimal output power profile is often used, where for every speed condition a specific load value is calculated. Thus, this would overcome the main shortcoming of the proposed method, given that the application does not require optimization for multiple load levels in a particular speed value.

Regarding Chapter 4, a few different ideas can be explored. Initially, a finite-time convergence analysis should be carried out, ensuring that the algorithm converges to the sliding surface. This is of interest given that only a stability proof has been presented for the proposed algorithm. In addition, more sophisticated sliding surfaces can be investigated, such as an integral one. If adequately designed, this could potentially

improve the performance of the DTSTSM algorithm, or enable a simpler implementation, making use of fixed gains over a wide speed range. Moreover, the design of traditional discrete-time sliding mode controllers can be further investigated for SRMs. Aspects such as discrete-time implementation, control law formulation and gain design have not been deeply investigated and leave margin for future contributions. Lastly, aspects such as switching and conduction losses in semiconductor devices while using PWM-based current controllers should be investigated, and compared to the traditional hysteresis approach. As it is briefly discussed in this thesis, a more accurate controller with higher switching frequency may result in lower efficiency in certain operating conditions. An analysis should be conducted, indicating the trade-offs as a function of switching and sampling frequency, for example. The analysis could also be extended to the hysteresis current controllers, investigating metrics in different conditions of hysteresis band and sampling frequencies.

5.3 PUBLICATIONS

The following papers have been submitted for peer review and presented during the development of this thesis. They are, in chronological order:

- Papers published in scientific journals:
 1. OSÓRIO, C. R. D.; SCALCON, F. P.; KOCH, G. G.; MONTAGNER, V. F.; VIEIRA, R. P.; GRÜNDLING, H. A. Controle Robusto Aplicado a Geradores de Relutância Variável Conectados à Rede. **Eletrônica de Potência (Impresso)**, v. 25, n. 3, p.1 - 11, 2020. DOI: 10.18618/REP.2020.3.0015.
 2. SCALCON, F. P.; OSÓRIO, C. R. D.; KOCH, G. G.; GABBI, T. S.; VIEIRA, R. P.; GRÜNDLING, H. A.; OLIVEIRA, R. C. L. F.; MONTAGNER, V. F. Robust Control of Synchronous Reluctance Motors by Means of Linear Matrix Inequalities. **IEEE Transactions on Energy Conversion**, 2020. DOI: 10.1109/TEC.2020.3028568.
 3. SCALCON, F. P.; GABBI, T. S.; VIEIRA, R. P.; GRÜNDLING, H. A. Melhoria de Desempenho de Motores de Relutância Variável via Algoritmo de Enxame de Partículas. **Eletrônica de Potência (Impresso)**, v. 25, n. 4, p.492 - 502, 2020. DOI: 10.18618/REP.2020.4.0038.
 4. KOCH, G. G.; OSÓRIO, C. R. D.; SCALCON, F. P.; GABBI, T. S.; OLIVEIRA, R. C. L. F.; MONTAGNER, V. F. Controle Robusto por Meio de LMIs Aplicado a Motores Síncronos de Ímãs Permanentes com Parâmetros Incertos. **Eletrônica de Potência (Impresso)**, v. 26, n. 1, p.115 - 124, 2021. DOI: 10.18618/REP.2021.1.0066.

5. FANG, G.; SCALCON, F. P.; XIAO, D.; VIEIRA, R. P.; GRÜNDLING, H. A.; EMADI, A. Advanced Control of Switched Reluctance Motors (SRMs): A Review on Current Regulation, Torque Control and Vibration Suppression. **IEEE Open Journal of the Industrial Electronics Society**, v. 2, p. 280-301, 2021, DOI: 10.1109/OJIES.2021.3076807.
- Papers accepted for publication in scientific journals:
 1. SCALCON, F. P.; FANG, G.; VIEIRA, R. P.; GRÜNDLING, H. A.; EMADI, A. Discrete-Time Super-Twisting Sliding Mode Current Controller with Fixed Switching Frequency for Switched Reluctance Motors. **IEEE Transactions on Power Electronics**, 2021.
 - Papers presented in national and international conferences:
 1. SCALCON, F. P.; GABBI, T. S.; VIEIRA, R. P.; GRÜNDLING, H. A. Decoupled Vector Control Based on Disturbance Observer Applied to the Synchronous Reluctance Motor. **21st European Conference on Power Electronics and Applications (EPE)**, 2019.
 2. SCALCON, F. P.; VOLPATO FILHO, C. J.; LAZZARI, T.; GABBI, T. S.; VIEIRA, R. P.; GRÜNDLING, H. A. Sensorless Control of a SynRM Drive Based on a Luenberger Observer with an Extended EMF Model. **45th Annual Conference of the IEEE Industrial Electronics Society (IECON)**, 2019.
 3. OSÓRIO, C. R. D.; SCALCON, F. P.; VIEIRA, R. P.; MONTAGNER, V. F.; GRÜNDLING, H. A. Controle Robusto de Geradores de Relutância Variável Conectados à Rede Elétrica. **12th Seminar on Power Electronics and Control (SEPOC)**, 2019.
 4. PEDROSO, D. A.; SCALCON, F. P.; NICOLINI, A. M.; PINHEIRO, H.; RECH, C. Técnicas de Regulação do Ponto de Neutro para Conversor NPC 3 Níveis. **12th Seminar on Power Electronics and Control (SEPOC)**, 2019.
 5. SCALCON, F. P.; PEDROSO, D. A.; VIEIRA, R. P.; GRÜNDLING, H. A.; RECH, C. Conversor NPC Assimétrico com Histerese Multinível para Acionamento de Motores de Relutância Variável. **12th Seminar on Power Electronics and Control (SEPOC)**, 2019.
 6. LAZZARI, T.; SCALCON, F. P.; VOLPATO FILHO, C. J.; GABBI, T. S.; STEFANELLO, M.; VIEIRA, R. P. Controle Vetorial Sensorless de MSIP com FCEM Não Senoidal Baseado em Observadores de Estados. **12th Seminar on Power Electronics and Control (SEPOC)**, 2019.

7. LAZZARI, T.; SCALCON, F. P.; VOLPATO FILHO, C. J.; GABBI, T. S.; STEFANELLO, M.; VIEIRA, R. P. Sensorless Control of Nonsinusoidal Back-EMF PMSM Based on State Observer. **5th IEEE Southern Power Electronics Conference (SPEC) & 15th Brazilian Power Electronics Conference (COBEP)**, 2019.
8. OSÓRIO, C. R. D.; SCALCON, F. P.; VIEIRA, R. P.; MONTAGNER, V. F.; GRÜNDLING, H. A. Robust Control of Switched Reluctance Generator In Connection With a Grid-Tied Inverter. **5th IEEE Southern Power Electronics Conference (SPEC) & 15th Brazilian Power Electronics Conference (COBEP)**, 2019.
9. SCALCON, F. P.; GABBI, T. S.; VIEIRA, R. P.; GRÜNDLING, H. A.; RECH C. Controle de um Motor de Relutância Variável com Conversor Flying Capacitor Assimétrico e Histerese Multinível. **XXIII Congresso Brasileiro de Automática (CBA)**, 2020.
10. SCALCON, F. P.; GABBI, T. S.; VIEIRA, R. P.; GRÜNDLING, H. A. Otimização dos Ângulos de Disparo de um Motor de Relutância Variável via Algoritmo de Enxame de Partículas. **XXIII Congresso Brasileiro de Automática (CBA)**, 2020.

REFERENCES

- AHMAD, S. S.; NARAYANAN, G. Linearized modeling of switched reluctance motor for closed-loop current control. **IEEE Transactions on Industry Applications**, v. 52, n. 4, p. 3146–3158, 2016.
- _____. Predictive control based constant current injection scheme for characterization of switched reluctance machine. **IEEE Transactions on Industry Applications**, v. 54, n. 4, p. 3383–3392, 2018.
- ALHARKAN, H. et al. Q-learning scheduling for tracking current control of switched reluctance motor drives. In: **2020 IEEE Power and Energy Conference at Illinois (PECI)**. [S.l.: s.n.], 2020. p. 1–6.
- ARAB, M. W. et al. Current controller for switched reluctance motors using pole placement approach. In: **2013 International Electric Machines Drives Conference**. [S.l.: s.n.], 2013. p. 1119–1125.
- ASTRÖM, K.; WITTENMARK, B. **Computer-controlled systems: theory and design**. [S.l.]: Prentice Hall, 1997. ISBN 9780133148992.
- BALARAM, V. Rare earth elements: A review of applications, occurrence, exploration, analysis, recycling, and environmental impact. **Geoscience Frontiers**, v. 10, n. 4, p. 1285–1303, 2019.
- BANERJEE, R.; SENGUPTA, M.; DALAPATI, S. Design and implementation of current mode control in a switched reluctance drive. In: **2014 IEEE International Conference on Power Electronics, Drives and Energy Systems (PEDES)**. [S.l.: s.n.], 2014. p. 1–5.
- BAOMING, G.; NAN, Z. Dsp-based discrete-time reaching law control of switched reluctance motor. In: **2006 CES/IEEE 5th International Power Electronics and Motion Control Conference**. [S.l.: s.n.], 2006. v. 2, p. 1–5.
- BARATIERI, C. L.; PINHEIRO, H. New variable gain super-twisting sliding mode observer for sensorless vector control of nonsinusoidal back-emf pmsm. **Control Engineering Practice**, v. 52, p. 59–69, 2016. ISSN 0967-0661.
- BARNES, M.; POLLOCK, C. Power electronic converters for switched reluctance drives. **IEEE Transactions on Power Electronics**, v. 13, n. 6, p. 1100–1111, Nov 1998. ISSN 0885-8993.
- BARROS, T. A. d. S. et al. Algoritmos para otimização do desempenho de geradores a relutância variável aplicados em geração eólica. **Revista Eletrônica de Potência**, v. 21, n. 1, p. 32–41, 2016.

- BARROS, T. A. D. S. et al. Automatic characterization system of switched reluctance machines and nonlinear modeling by interpolation using smoothing splines. **IEEE Access**, v. 6, p. 26011–26021, 2018. ISSN 2169-3536.
- BHOWMICK, D.; MANNA, M.; CHOWDHURY, S. K. Estimation of equivalent circuit parameters of transformer and induction motor from load data. **IEEE Transactions on Industry Applications**, v. 54, n. 3, p. 2784–2791, 2018.
- BILGIN, B. et al. Making the case for switched reluctance motors for propulsion applications. **IEEE Transactions on Vehicular Technology**, v. 69, n. 7, p. 7172–7186, 2020.
- BILGIN, B.; JIANG, J.; EMADI, A. **Switched Reluctance Motor Drives: Fundamentals to Applications**. [S.l.]: CRC Press, 2019. ISBN 9781351396721.
- BILGIN, B. et al. Making the case for electrified transportation. **IEEE Transactions on Transportation Electrification**, v. 1, n. 1, p. 4–17, 2015.
- BOGLIETTI, A. et al. Thermal analysis of induction and synchronous reluctance motors. **IEEE Transactions on Industry Applications**, v. 42, n. 3, p. 675–680, 2006.
- BOLDEA, I. et al. Automotive electric propulsion systems with reduced or no permanent magnets: An overview. **IEEE Transactions on Industrial Electronics**, v. 61, n. 10, p. 5696–5711, Oct 2014. ISSN 0278-0046.
- BOYD, S. et al. **Linear Matrix Inequalities in System and Control Theory**. Philadelphia, PA: SIAM Studies in Applied Mathematics, 1994.
- BRAZILIAN COMPANY OF ENERGY RESEARCH. **Statistical Yearbook of Electricity - Base Year 2011**. [S.l.], 2012.
- _____. **Statistical Yearbook of Electricity - Base Year 2019**. [S.l.], 2020.
- CALVINI, M. et al. PSO-based self-commissioning of electrical motor drives. **IEEE Transactions on Industrial Electronics**, v. 62, n. 2, p. 768–776, 2015.
- CHOI, C. et al. A new torque control method of a switched reluctance motor using a torque-sharing function. **IEEE Transactions on Magnetics**, v. 38, n. 5, p. 3288–3290, 2002.
- CHOI, J.-H.; AHN, J.; LEE, J. The characteristic analysis of switched reluctance motor considering dc-link voltage ripple on hard and soft chopping modes. **IEEE Transactions on Magnetics**, v. 41, n. 10, p. 4096–4098, 2005.
- DHALE, S.; NAHID-MOBARAKEH, B.; EMADI, A. A review of fixed switching frequency current control techniques for switched reluctance machines. **IEEE Access**, v. 9, p. 39375–39391, 2021.

- DOWLATSHAHI, M.; NEJAD, S. M. S.; AHN, J.-W. Torque ripple minimization of switched reluctance motor using modified torque sharing function. In: **2013 21st Iranian Conference on Electrical Engineering (ICEE)**. [S.l.: s.n.], 2013. p. 1–6.
- EBERHART; SHI, Y. Particle swarm optimization: developments, applications and resources. In: **Proceedings of the 2001 Congress on Evolutionary Computation (IEEE Cat. No.01TH8546)**. [S.l.: s.n.], 2001. v. 1, p. 81–86 vol. 1.
- FANG, G. et al. Advanced control of switched reluctance motors (SRMs): A review on current regulation, torque control and vibration suppression. **IEEE Open Journal of the Industrial Electronics Society**, v. 2, p. 280–301, 2021.
- _____. An intersection-method based current controller for switched reluctance machines with robust tracking performance. **IEEE Transactions on Transportation Electrification**, p. 1–1, 2021.
- _____. Time-efficient torque shaping for switched reluctance machines from linear space. **IEEE Transactions on Power Electronics**, v. 36, n. 8, p. 9361–9371, 2021.
- FILHO, C. J. V. et al. Observers for high-speed sensorless pmsm drives: Design methods, tuning challenges and future trends. **IEEE Access**, v. 9, p. 56397–56415, 2021.
- FISCH, J. H. et al. Pareto-optimal firing angles for switched reluctance motor control. In: **Second International Conference On Genetic Algorithms In Engineering Systems: Innovations And Applications**. [S.l.: s.n.], 1997. p. 90–96.
- FRANCIS, B. A.; WONHAM, W. M. The internal model principle of control theory. **Automatica**, v. 12, n. 5, p. 457–465, September 1976.
- GAN, C. et al. A position sensorless torque control strategy for switched reluctance machines with fewer current sensors. **IEEE/ASME Transactions on Mechatronics**, v. 26, n. 2, p. 1118–1128, 2021.
- GAO, H.; SALMASI, F. R.; EHSANI, M. Inductance model-based sensorless control of the switched reluctance motor drive at low speed. **IEEE Transactions on Power Electronics**, v. 19, n. 6, p. 1568–1573, Nov 2004. ISSN 0885-8993.
- GBENGA, D. E.; RAMLAN, E. I. Understanding the limitations of particle swarm algorithm for dynamic optimization tasks: A survey towards the singularity of pso for swarm robotic applications. **ACM Comput. Surv.**, Association for Computing Machinery, New York, NY, USA, v. 49, n. 1, jul. 2016. ISSN 0360-0300.
- GIERAS, J. F. Design of permanent magnet brushless motors for high speed applications. In: **2014 17th International Conference on Electrical Machines and Systems (ICEMS)**. [S.l.: s.n.], 2014. p. 1–16.
- GOBBI, R.; SAHOO, N. C.; VEJIAN, R. The measurement of mechanical parameters of a switched reluctance motor drive system. **Measurement Science and Technology**, IOP Publishing, v. 18, n. 11, p. 3636–3644, oct 2007.

- GONZALEZ, T.; MORENO, J. A.; FRIDMAN, L. Variable gain super-twisting sliding mode control. **IEEE Transactions on Automatic Control**, v. 57, n. 8, p. 2100–2105, 2012.
- HANNOUN, H.; HILAIRET, M.; MARCHAND, C. Gain-scheduling pi current controller for a switched reluctance motor. In: **2007 IEEE International Symposium on Industrial Electronics**. [S.l.: s.n.], 2007. p. 1177–1182.
- HU, K.; GUO, L.; YE, J. Model predictive current control of mutually coupled switched reluctance machines using a three-phase voltage source converter. In: **2020 IEEE Applied Power Electronics Conference and Exposition (APEC)**. [S.l.: s.n.], 2020. p. 704–710.
- HU, K.; YE, J.; VELNI, J. M. Sliding mode current control of mutually coupled switched reluctance machines using a three-phase voltage source converter. In: **2019 IEEE Energy Conversion Congress and Exposition (ECCE)**. [S.l.: s.n.], 2019. p. 1776–1781.
- HU, K. et al. A fixed-switching-frequency sliding mode current controller for mutually coupled switched reluctance machines using asymmetric bridge converter. In: **2019 IEEE Transportation Electrification Conference and Expo (ITEC)**. [S.l.: s.n.], 2019. p. 1–6.
- HUANG, H. et al. A current control scheme with back emf cancellation and tracking error adapted commutation shift for switched-reluctance motor drive. **IEEE Transactions on Industrial Electronics**, v. 63, n. 12, p. 7381–7392, 2016.
- HUSAIN, I.; EHSANI, M. Torque ripple minimization in switched reluctance motor drives by pwm current control. **IEEE Transactions on Power Electronics**, v. 11, n. 1, p. 83–88, 1996.
- IEEE. Ieee guide for test procedures for synchronous machines part i?acceptance and performance testing part ii?test procedures and parameter determination for dynamic analysis. **IEEE Std 115-2009 (Revision of IEEE Std 115-1995)**, p. 1–219, 2010.
- ILIC'-SPONG, M. et al. Feedback linearizing control of switched reluctance motors. **IEEE Transactions on Automatic Control**, v. 32, n. 5, p. 371–379, 1987.
- ILIC-SPONG, M. et al. Instantaneous torque control of electric motor drives. **IEEE Transactions on Power Electronics**, PE-2, n. 1, p. 55–61, 1987.
- JACK, A. G.; MECROW, B. C.; HAYLOCK, J. A. A comparative study of permanent magnet and switched reluctance motors for high-performance fault-tolerant applications. **IEEE Transactions on Industry Applications**, v. 32, n. 4, p. 889–895, July 1996. ISSN 0093-9994.
- KENNEDY, J.; EBERHART, R. Particle swarm optimization. In: **Proceedings of ICNN'95 - International Conference on Neural Networks**. [S.l.: s.n.], 1995. v. 4, p. 1942–1948 vol.4.

- KIANI, M. Model predictive control of stator currents in switched reluctance generators. In: **2014 IEEE 23rd International Symposium on Industrial Electronics (ISIE)**. [S.l.: s.n.], 2014. p. 842–846.
- KIM, H. et al. Discrete-time current regulator design for ac machine drives. **IEEE Transactions on Industry Applications**, v. 46, n. 4, p. 1425–1435, 2010.
- KIOSKERIDIS, I.; MADEMLIS, C. Maximum efficiency in single-pulse controlled switched reluctance motor drives. **IEEE Transactions on Energy Conversion**, v. 20, n. 4, p. 809–817, 2005.
- _____. A unified approach for four-quadrant optimal controlled switched reluctance machine drives with smooth transition between control operations. **IEEE Transactions on Power Electronics**, v. 24, n. 1, p. 301–306, 2009.
- KIYOTA, K.; CHIBA, A. Design of switched reluctance motor competitive to 60-kw ipmsm in third-generation hybrid electric vehicle. **IEEE Transactions on Industry Applications**, v. 48, n. 6, p. 2303–2309, 2012.
- KOCH, G. G. et al. Robust \mathcal{H}_∞ state feedback controllers based on linear matrix inequalities applied to grid-connected converters. **IEEE Transactions on Industrial Electronics**, v. 66, n. 8, p. 6021–6031, Aug 2019. ISSN 1557-9948.
- KOCH, S.; REICHHARTINGER, M. Discrete-time equivalents of the super-twisting algorithm. **Automatica**, v. 107, p. 190 – 199, 2019. ISSN 0005-1098.
- KRISHNAMURTHY, M. et al. Making the case for applications of switched reluctance motor technology in automotive products. **IEEE Transactions on Power Electronics**, v. 21, n. 3, p. 659–675, 2006.
- KRISHNAN, R. **Switched Reluctance Motor Drives: Modeling, Simulation, Analysis, Design, and Applications**. [S.l.]: CRC Press, 2001. (Industrial Electronics). ISBN 9781420041644.
- LAI, C. et al. Investigation and analysis of iterative learning-based current control algorithm for switched reluctance motor applications. In: **2014 International Conference on Electrical Machines (ICEM)**. [S.l.: s.n.], 2014. p. 796–802.
- LEE, D.-H. et al. Modified tsf for the high speed switched reluctance motor. In: **2011 IEEE International Symposium on Industrial Electronics**. [S.l.: s.n.], 2011. p. 655–660.
- _____. A simple nonlinear logical torque sharing function for low-torque ripple sr drive. **IEEE Transactions on Industrial Electronics**, v. 56, n. 8, p. 3021–3028, 2009.
- LEVANT, A. Sliding order and sliding accuracy in sliding mode control. **International Journal of Control**, Taylor & Francis, v. 58, n. 6, p. 1247–1263, 1993.

LI, H. **Torque Ripple Minimization in Switched Reluctance Machines**. Tese (Doutorado) — McMaster University, 2017.

LI, H.; BILGIN, B.; EMADI, A. An improved torque sharing function for torque ripple reduction in switched reluctance machines. **IEEE Transactions on Power Electronics**, v. 34, n. 2, p. 1635–1644, 2019.

LI, S. et al. Modeling, design optimization, and applications of switched reluctance machines: A review. **IEEE Transactions on Industry Applications**, v. 55, n. 3, p. 2660–2681, 2019.

LI, X.; SHAMSI, P. Adaptive model predictive current control for dssrm drives. In: **2014 IEEE Transportation Electrification Conference and Expo (ITEC)**. [S.l.: s.n.], 2014. p. 1–5.

_____. Inductance surface learning for model predictive current control of switched reluctance motors. **IEEE Transactions on Transportation Electrification**, v. 1, n. 3, p. 287–297, 2015.

_____. Model predictive current control of switched reluctance motors with inductance auto-calibration. **IEEE Transactions on Industrial Electronics**, v. 63, n. 6, p. 3934–3941, 2016.

LIN, Z. et al. High-performance current control for switched reluctance motors based on on-line estimated parameters. **IET Electric Power Applications**, v. 4, n. 1, p. 67–74, 2010.

_____. Torque ripple reduction in switched reluctance motor drives using b-spline neural networks. **IEEE Transactions on Industry Applications**, v. 42, n. 6, p. 1445–1453, 2006.

LIU, Z.-H. et al. Global identification of electrical and mechanical parameters in pmsm drive based on dynamic self-learning pso. **IEEE Transactions on Power Electronics**, v. 33, n. 12, p. 10858–10871, 2018.

_____. Parameter estimation for vsi-fed pmsm based on a dynamic PSO with learning strategies. **IEEE Transactions on Power Electronics**, v. 32, n. 4, p. 3154–3165, 2017.

LOVATT, H.; STEPHENSON, J. Computer-optimised smooth-torque current waveforms for switched-reluctance motors. **IEE Proceedings - Electric Power Applications**, v. 144, p. 310–316(6), September 1997.

MA, M. et al. A switched reluctance motor torque ripple reduction strategy with deadbeat current control. In: **2019 14th IEEE Conference on Industrial Electronics and Applications (ICIEA)**. [S.l.: s.n.], 2019. p. 25–30.

MACCARI JR., L. A. et al. LMI-based control for grid-connected converters with LCL filters under uncertain parameters. **IEEE Transactions on Power Electronics**, v. 29, n. 7, p. 3776–3785, July 2014. ISSN 0885-8993.

- MADEMLIS, C.; KIOSKERIDIS, I. Performance optimization in switched reluctance motor drives with online commutation angle control. **IEEE Transactions on Energy Conversion**, v. 18, n. 3, p. 448–457, 2003.
- _____. Optimizing performance in current-controlled switched reluctance generators. **IEEE Transactions on Energy Conversion**, v. 20, n. 3, p. 556–565, 2005.
- MANOLAS, I.; PAPAFOOTI, G.; MANIAS, S. N. Sliding mode pwm for effective current control in switched reluctance machine drives. In: **2014 International Power Electronics Conference (IPEC-Hiroshima 2014 - ECCE ASIA)**. [S.l.: s.n.], 2014. p. 1606–1612.
- MANOLAS, I. S.; KALETSANOS, A. X.; MANIAS, S. N. Nonlinear current control technique for high performance switched reluctance machine drives. In: **2008 IEEE Power Electronics Specialists Conference**. [S.l.: s.n.], 2008. p. 1229–1234.
- MEHTA, S.; HUSAIN, I.; PRAMOD, P. Predictive current control of mutually coupled switched reluctance motors using net flux method. In: **2019 IEEE Energy Conversion Congress and Exposition (ECCE)**. [S.l.: s.n.], 2019. p. 4918–4922.
- MEHTA, S.; KABIR, M. A.; HUSAIN, I. Extended speed current profiling algorithm for low torque ripple srm using model predictive control. In: **2018 IEEE Energy Conversion Congress and Exposition (ECCE)**. [S.l.: s.n.], 2018. p. 4558–4563.
- MIKAIL, R. et al. A fixed switching frequency predictive current control method for switched reluctance machines. In: **2012 IEEE Energy Conversion Congress and Exposition (ECCE)**. [S.l.: s.n.], 2012. p. 843–847.
- _____. _____. **IEEE Transactions on Industry Applications**, v. 50, n. 6, p. 3717–3726, 2014.
- MILASI, R. M.; MOALLEM, M. A novel multi-loop self-tuning adaptive pi control scheme for switched reluctance motors. In: **IECON 2014 - 40th Annual Conference of the IEEE Industrial Electronics Society**. [S.l.: s.n.], 2014. p. 337–342.
- MILLER, J. M. **Electric Motor R&D**. 2013. <https://www.energy.gov/sites/prod/files/2014/03/f13/ape051_miller_2013_o.pdf>. (Accessed on 03/09/2020).
- MILLER, T. (Ed.). **Electronic Control of Switched Reluctance Machines**. Oxford, UK: Newnes Publishers, 2001.
- MILLER, T. J. E. Optimal design of switched reluctance motors. **IEEE Transactions on Industrial Electronics**, v. 49, n. 1, p. 15–27, Feb 2002. ISSN 0278-0046.
- MYNAR, Z.; VESELY, L.; VACLAVEK, P. Pmsm model predictive control with field-weakening implementation. **IEEE Transactions on Industrial Electronics**, v. 63, n. 8, p. 5156–5166, 2016.

- NAITOH, H.; ISHIKAWA, H. A current controller for a switched reluctance motor based on model reference adaptive control. In: **SPEEDAM 2010**. [S.l.: s.n.], 2010. p. 1270–1275.
- NETO, P. J. d. S. et al. Design of computational experiment for performance optimization of a switched reluctance generator in wind systems. **IEEE Transactions on Energy Conversion**, v. 33, n. 1, p. 406–419, 2018.
- OKAMOTO, Y. et al. Improvement of torque characteristics for a synchronous reluctance motor using mma-based topology optimization method. **IEEE Transactions on Magnetism**, v. 54, n. 3, p. 1–4, 2018.
- OLALLA, C. et al. Robust LQR control for PWM converters: An LMI approach. **IEEE Transactions on Industrial Electronics**, v. 56, n. 7, p. 2548–2558, July 2009.
- OSÓRIO, C. R. D. **Contribuição ao Estudo de Técnicas de Acionamento e Controle Aplicadas ao Gerador de Relutância Variável**. Dissertação (Mestrado) — Universidade Federal de Santa Maria, 2017.
- OSÓRIO, C. R. D. et al. Robust current control of grid-tied inverters affected by LCL filter soft-saturation. **IEEE Transactions on Industrial Electronics**, p. 1–1, 2019. ISSN 1557-9948.
- _____. Comparative analysis of predictive current control techniques applied to single-phase grid-connected inverters. In: **2017 Brazilian Power Electronics Conference (COBEP)**. [S.l.: s.n.], 2017. p. 1–6.
- OUDDAH, N. et al. Robust lpv current control of switched reluctance motors. In: **22nd Mediterranean Conference on Control and Automation**. [S.l.: s.n.], 2014. p. 218–223.
- PAULA, M. V. de et al. A dahlin cruise control design method for switched reluctance motors with minimum torque ripple point tracking applied in electric vehicles. **IEEE Transactions on Transportation Electrification**, p. 1–1, 2020.
- PENG, F.; EMADI, A. A digital pwm current controller for switched reluctance motor drives. In: **2014 IEEE Transportation Electrification Conference and Expo (ITEC)**. [S.l.: s.n.], 2014. p. 1–6.
- PENG, F.; YE, J.; EMADI, A. A digital pwm current controller for switched reluctance motor drives. **IEEE Transactions on Power Electronics**, v. 31, n. 10, p. 7087–7098, 2016.
- PILLAY, P.; KRISHNAN, R. Modeling, simulation, and analysis of permanent-magnet motor drives. i. the permanent-magnet synchronous motor drive. **IEEE Transactions on Industry Applications**, v. 25, n. 2, p. 265–273, March 1989. ISSN 0093-9994.

- POZNYAK, A. **Advanced Mathematical Tools for Control Engineers: Volume 1: Deterministic Systems**. [S.l.]: Elsevier, 2010. ISBN 9780080556109.
- PREINDL, M.; BOLOGNANI, S. Model predictive direct torque control with finite control set for pmsm drive systems, part 2: Field weakening operation. **IEEE Transactions on Industrial Informatics**, v. 9, n. 2, p. 648–657, 2013.
- RAFAQ, M. S.; JUNG, J. A comprehensive review of state-of-the-art parameter estimation techniques for permanent magnet synchronous motors in wide speed range. **IEEE Transactions on Industrial Informatics**, v. 16, n. 7, p. 4747–4758, 2020.
- RAIN, X.; HILAIRET, M.; TALJ, R. Second order sliding mode current controller for the switched reluctance machine. In: **IECON 2010 - 36th Annual Conference on IEEE Industrial Electronics Society**. [S.l.: s.n.], 2010. p. 3301–3306.
- RAO, S. S. **Engineering Optimization - Theory and Practice**. 4. ed. [S.l.]: Wiley, 2009. ISBN 9780470183526,0470183527.
- RODRIGUEZ, J. et al. State of the art of finite control set model predictive control in power electronics. **IEEE Transactions on Industrial Informatics**, v. 9, n. 2, p. 1003–1016, 2013.
- ROHAK-SEUNG et al. Torque ripple minimization scheme using torque sharing function based fuzzy logic control for a switched reluctance motor. **Journal of Electrical Engineering and Technology**, v. 10, n. 1, p. 118–127, 2015.
- RUIWEI, Z. et al. An adaptive sliding mode current control for switched reluctance motor. In: **2014 IEEE Conference and Expo Transportation Electrification Asia-Pacific (ITEC Asia-Pacific)**. [S.l.: s.n.], 2014. p. 1–6.
- SAHOO, N.; XU, J.; PANDA, S. Determination of current waveforms for torque ripple minimisation in switched reluctance motors using iterative learning: an investigation. **IEE Proceedings - Electric Power Applications**, v. 146, p. 369–377(8), July 1999.
- SAHOO, N. C.; XU, J. X.; PANDA, S. K. Low torque ripple control of switched reluctance motors using iterative learning. **IEEE Transactions on Energy Conversion**, v. 16, n. 4, p. 318–326, 2001.
- SAHOO, S. K.; PANDA, S. K.; XU, J. X. Iterative learning-based high-performance current controller for switched reluctance motors. **IEEE Transactions on Energy Conversion**, v. 19, n. 3, p. 491–498, 2004.
- SAHOO, S. K.; PANDA, S. K.; XU, J.-X. Indirect torque control of switched reluctance motors using iterative learning control. **IEEE Transactions on Power Electronics**, v. 20, n. 1, p. 200–208, 2005.
- SALEM, F. B. et al. A second-order sliding mode control of switched reluctance motor. **Electric Power Components and Systems**, v. 48, n. 6-7, p. 640–651, 2020.

- SALGADO, I. et al. Discrete-time non-linear state observer based on a super twisting-like algorithm. **IET Control Theory Applications**, v. 8, n. 10, p. 803–812, 2014.
- SALMASI, F. R.; FAHIMI, B. Modeling switched-reluctance machines by decomposition of double magnetic saliencies. **IEEE Transactions on Magnetics**, v. 40, n. 3, p. 1556–1561, May 2004. ISSN 0018-9464.
- SANKARDOSS, V.; GEETHANJALI, P. Pmdc motor parameter estimation using bio-inspired optimization algorithms. **IEEE Access**, v. 5, p. 11244–11254, 2017.
- SAYED, E. et al. Review of electric machines in more/hybrid/turbo electric aircraft. **IEEE Transactions on Transportation Electrification**, p. 1–1, 2021.
- SCALCON, F. P. et al. Robust control of synchronous reluctance motors by means of linear matrix inequalities. **IEEE Transactions on Energy Conversion**, v. 36, n. 2, p. 779–788, 2021.
- SCALCON, F. S. **Contribuições ao Acionamento e Controle dos Motores de Relutância Variável e Síncrono de Relutância**. Dissertação (Mestrado) — Universidade Federal de Santa Maria, 2019.
- SCHRAMM, D. S.; WILLIAMS, B. W.; GREEN, T. C. Torque ripple reduction of switched reluctance motors by phase current optimal profiling. In: **PESC '92 Record. 23rd Annual IEEE Power Electronics Specialists Conference**. [S.l.: s.n.], 1992. p. 857–860 vol.2.
- SCHRODER, G.; BEKIESCH, J. Adaptive current control for the srm. In: **Proceedings of the IEEE International Symposium on Industrial Electronics, 2005. ISIE 2005**. [S.l.: s.n.], 2005. v. 1, p. 69–74.
- SCHULZ, S. E.; RAHMAN, K. M. High-performance digital pi current regulator for ev switched reluctance motor drives. **IEEE Transactions on Industry Applications**, v. 39, n. 4, p. 1118–1126, 2003.
- SHI, Y.; EBERHART, R. C. Parameter selection in particle swarm optimization. In: PORTO, V. W. et al. (Ed.). **Evolutionary Programming VII**. Berlin, Heidelberg: Springer Berlin Heidelberg, 1998. p. 591–600.
- SONG, J.; SONG, S.; QU, B. Application of an adaptive pi controller for a switched reluctance motor drive. In: **2016 IEEE 2nd Annual Southern Power Electronics Conference (SPEC)**. [S.l.: s.n.], 2016. p. 1–5.
- STATON, D. A.; MILLER, T. J. E.; WOOD, S. E. Maximising the saliency ratio of the synchronous reluctance motor. **IEE Proceedings B - Electric Power Applications**, v. 140, n. 4, p. 249–259, July 1993. ISSN 0143-7038.
- ÜSTÜN, O.; ÖNDER, M.; SEFA, I. Identification of mechanical parameters for the switched reluctance motor. In: **2018 2nd International Symposium on Multidisciplinary Studies and Innovative Technologies (ISMSIT)**. [S.l.: s.n.], 2018. p. 1–7.

- SUN, Q. et al. OCTSF for torque ripple minimisation in srms. **IET Power Electronics**, v. 9, p. 2741–2750(9), November 2016.
- SUN, X. et al. Multiobjective and multiphysics design optimization of a switched reluctance motor for electric vehicle applications. **IEEE Transactions on Energy Conversion**, p. 1–1, 2021.
- TAYLOR, J. et al. Comparison of current control strategies for low- and high-power switched reluctance motor drives. In: **2020 IEEE Transportation Electrification Conference Expo (ITEC)**. [S.l.: s.n.], 2020. p. 198–203.
- TORREY, D. A. Switched reluctance generators and their control. **IEEE Transactions on Industrial Electronics**, v. 49, n. 1, p. 3–14, 2002.
- TSENG, K.; CAO, S. A srm variable speed drive with torque ripple minimization control. In: **APEC 2001. Sixteenth Annual IEEE Applied Power Electronics Conference and Exposition (Cat. No.01CH37181)**. [S.l.: s.n.], 2001. v. 2, p. 1083–1089 vol.2.
- UNITED STATES GEOLOGICAL SURVEY. **Rare Earths Statistics and Information**. 2020. <<https://www.usgs.gov/centers/nmic/rare-earths-statistics-and-information>>. (Accessed on 03/09/2020).
- UTKIN, V.; LEE, H. Chattering problem in sliding mode control systems. In: **International Workshop on Variable Structure Systems, 2006. VSS'06**. [S.l.: s.n.], 2006. p. 346–350.
- VALENCIA, D. F. et al. Virtual-flux finite control set model predictive control of switched reluctance motor drives. In: **IECON 2019 - 45th Annual Conference of the IEEE Industrial Electronics Society**. [S.l.: s.n.], 2019. v. 1, p. 1465–1470.
- VUJICIC, V. P. Minimization of torque ripple and copper losses in switched reluctance drive. **IEEE Transactions on Power Electronics**, v. 27, n. 1, p. 388–399, 2012.
- WANG, H. et al. Precise discrete-time steering control for robotic fish based on data-assisted technique and super-twisting-like algorithm. **IEEE Transactions on Industrial Electronics**, p. 1–1, 2020.
- WANG, X.; LAI, J.-S. Small-signal modeling and control for pwm control of switched reluctance motor drives. In: **2002 IEEE 33rd Annual IEEE Power Electronics Specialists Conference. Proceedings (Cat. No.02CH37289)**. [S.l.: s.n.], 2002. v. 2, p. 546–551 vol.2.
- WANG, Z. et al. Challenges faced by electric vehicle motors and their solutions. **IEEE Access**, v. 9, p. 5228–5249, 2021.
- WATTHEWADUGE, G. et al. Electromagnetic modeling techniques for switched reluctance machines: State-of-the-art review. **IEEE Open Journal of the Industrial Electronics Society**, v. 1, p. 218–234, 2020.

- WORLD BANK. **World Bank Open Data | Data**. 2020. <<https://data.worldbank.org/>>. (Accessed on 03/07/2020).
- XIA, Z. et al. A new torque sharing function method for switched reluctance machines with lower current tracking error. **IEEE Transactions on Industrial Electronics**, v. 68, n. 11, p. 10612–10622, 2021.
- XUE, X. D.; CHENG, K. W. E.; HO, S. L. Optimization and evaluation of torque-sharing functions for torque ripple minimization in switched reluctance motor drives. **IEEE Transactions on Power Electronics**, v. 24, n. 9, p. 2076–2090, 2009.
- XUE, X. D. et al. Optimal control method of motoring operation for srm drives in electric vehicles. **IEEE Transactions on Vehicular Technology**, v. 59, n. 3, p. 1191–1204, 2010.
- YANG, C. et al. Online parallel estimation of mechanical parameters for pmsm drives via a network of interconnected extended sliding-mode observers. **IEEE Transactions on Power Electronics**, p. 1–1, 2021.
- YANG, Y.; ZHANG, Y. Sliding mode-pi control of switched reluctance motor drives for ev. In: **2005 International Conference on Electrical Machines and Systems**. [S.l.: s.n.], 2005. v. 1, p. 603–607 Vol. 1.
- YAO, X. et al. High-performance torque control for switched reluctance motor based on online fuzzy neural network modeling. In: **2010 International Conference on Intelligent System Design and Engineering Application**. [S.l.: s.n.], 2010. v. 1, p. 817–822.
- YE, J.; BILGIN, B.; EMADI, A. Elimination of mutual flux effect on rotor position estimation of switched reluctance motor drives considering magnetic saturation. **IEEE Transactions on Power Electronics**, v. 30, n. 2, p. 532–536, Feb 2015. ISSN 0885-8993.
- _____. An extended-speed low-ripple torque control of switched reluctance motor drives. **IEEE Transactions on Power Electronics**, v. 30, n. 3, p. 1457–1470, 2015.
- _____. An offline torque sharing function for torque ripple reduction in switched reluctance motor drives. **IEEE Transactions on Energy Conversion**, v. 30, n. 2, p. 726–735, 2015.
- YE, J.; MALYSZ, P.; EMADI, A. A fixed-switching-frequency integral sliding mode current controller for switched reluctance motor drives. **IEEE Journal of Emerging and Selected Topics in Power Electronics**, v. 3, n. 2, p. 381–394, 2015.
- YI, Z. et al. An optimal torque controller based on iterative learning control for switched reluctance motors for electric vehicles. In: **2010 International Conference on Optoelectronics and Image Processing**. [S.l.: s.n.], 2010. v. 1, p. 230–233.

ZHANG, X.; LI, Z. Sliding-mode observer-based mechanical parameter estimation for permanent magnet synchronous motor. **IEEE Transactions on Power Electronics**, v. 31, n. 8, p. 5732–5745, 2016.

ZHANG, X. et al. A switched reluctance motor torque ripple reduction strategy with deadbeat current control and active thermal management. **IEEE Transactions on Vehicular Technology**, v. 69, n. 1, p. 317–327, 2020.

ZHENG, Y. et al. A current control method of switched reluctance motors based on iterative learning control considering the mutual inductance. In: **2008 International Conference on Electrical Machines and Systems**. [S.l.: s.n.], 2008. p. 3401–3404.

APPENDICES

Appendix A – Fast Estimation of Mechanical Parameters for Switched Reluctance Motors Drives Based on PSO Algorithm

A.1 INTRODUCTION

Due to the highly nonlinear electrical behavior of SRMs, significant work has been carried out regarding the electromagnetic characterization and modeling of the machine (LI et al., 2019; WATTHEWADUGE et al., 2020). However, the problem of estimation and measurement of mechanical parameters has not been deeply investigated. In order to obtain a high performance SRM drive, knowledge of the moment of inertia and viscous friction coefficient of the machine is required, nonetheless, most manufacturers do not provide these values. Moreover, these parameters may change over time due to wear and lack of maintenance, for instance. Lastly, the knowledge of the machine parameters individually is not very useful, since coupling to a load imposes additional inertia and mechanical losses (GOBBI; SAHOO; VEJIAN, 2007). Thus, it is of interest to obtain the mechanical parameters of the coupled system.

IEEE Standard 115–1995 (IEEE, 2010) presents guidelines for the mechanical parameter testing procedures. The friction coefficient is associated with the windage and friction losses, being often determined through a deceleration test. This approach presents a challenge in the case of SRMs, as it requires the machine to be accelerated. SRMs are known for not being able to operate in an open loop scenario, such as induction motors, thus, requiring a controller to be designed beforehand. The moment of inertia, according to (IEEE, 2010), can be determined by a few different methods. However, most of them are not suitable to SRMs, such as methods 3 and 4 (refer to (IEEE, 2010)), which require access to field and armature windings.

Thus, alternative mechanical parameter estimation techniques have been investigated over the years (GOBBI; SAHOO; VEJIAN, 2007; ÜSTÜN; ÖNDER; SEFA, 2018; RAFAQ; JUNG, 2020; ZHANG; LI, 2016; YANG et al., 2021). Some strategies have been developed based on the classic mechanical model (GOBBI; SAHOO; VEJIAN, 2007; ÜSTÜN; ÖNDER; SEFA, 2018). In (GOBBI; SAHOO; VEJIAN, 2007) a mechanical measurement procedure is proposed, making use of speed-time curves to compute these parameters offline. The results are speed dependent, leading to a time variant model. A new real-time identification method, derived from the classic viscous plus Coulomb friction model, is described in (ÜSTÜN; ÖNDER; SEFA, 2018). Another viable approach for parameter estimation is through the use of observers (RAFAQ; JUNG, 2020). In (ZHANG; LI, 2016) and (YANG et al., 2021), for example, sliding mode observers are developed as a means to estimate the mechanical parameters of permanent magnet synchronous motors. However, note that few observer strategies have been directed at SRMs with this intent, mostly due to the machine’s complexity.

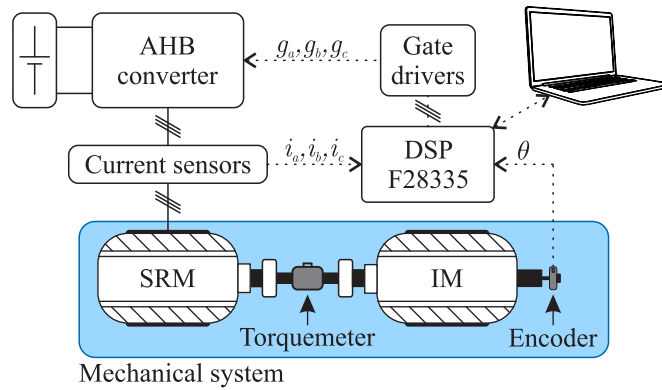
As an alternative, the use of optimization algorithms to estimate the mechanical parameter values can be a viable solution. A simple optimization strategy is achieved through a fine grid technique, also known as a brute force approach. The results from such technique, however, are dependent on the precision used to inspect the search space, leading to higher computational effort and, depending on the size of the search space, making the approach impractical. In this context, efficient optimization algorithms, such as the particle swarm optimization (PSO) (KENNEDY; EBERHART, 1995), become a useful tool (SANKARDOSS; GEETHANJALI, 2017; BHOWMICK; MANNA; CHOWDHURY, 2018; LIU et al., 2017; LIU et al., 2018; CALVINI et al., 2015). In (LIU et al., 2017) and (LIU et al., 2018), the PSO algorithm is used along with learning strategies as a means to estimate the electrical and mechanical parameters of PMSMs. A PSO-based self-commissioning approach for PMSMs is proposed in (CALVINI et al., 2015), where the model-based identification procedure is followed by a controller tuning optimization. Nevertheless, note that no optimization-based strategies have been proposed for SRMs. Thus, opportunities for deeper investigations using metaheuristics for the estimation of mechanical parameters are observed, especially when considering experimental validation.

In this context, this appendix presents as a contribution a systematic PSO-based procedure for the fast estimation of mechanical parameters of SRMs. The proposal aims to avoid cumbersome and time-consuming tests, requiring only the measurement of rotor speed, position and phase currents. The measured experimental data is uploaded to Matlab/Simulink and, using the known electromagnetic characteristics of the SRM, a series of simulations is performed, allowing the mechanical parameters to be estimated, based on a minimum squared error metric. The procedure enables a fast offline estimation of the parameters while only requiring a current step response, circumventing the need to design additional controllers or the use of sophisticated observers, for example. Experimental results are provided, showing that the estimated parameters lead to suitable simulation responses that match the measured data. In addition, the proposal presents flexibility, being easily modifiable for application in other electric machine drives.

A.2 PROBLEM DESCRIPTION

This appendix focuses on the mechanical system of a typical SRM drive. A block diagram of the entire drive is presented in Figure A.1. The drive is composed of a DC voltage source, an AHB converter and control hardware, such as sensors and a DSP. Lastly, the mechanical system is comprised of the SRM, and induction machine, couplings and the measuring hardware, in this case an absolute encoder.

Figure A.1 – Block diagram of an SRM drive, highlighting the mechanical system.



Source: Author.

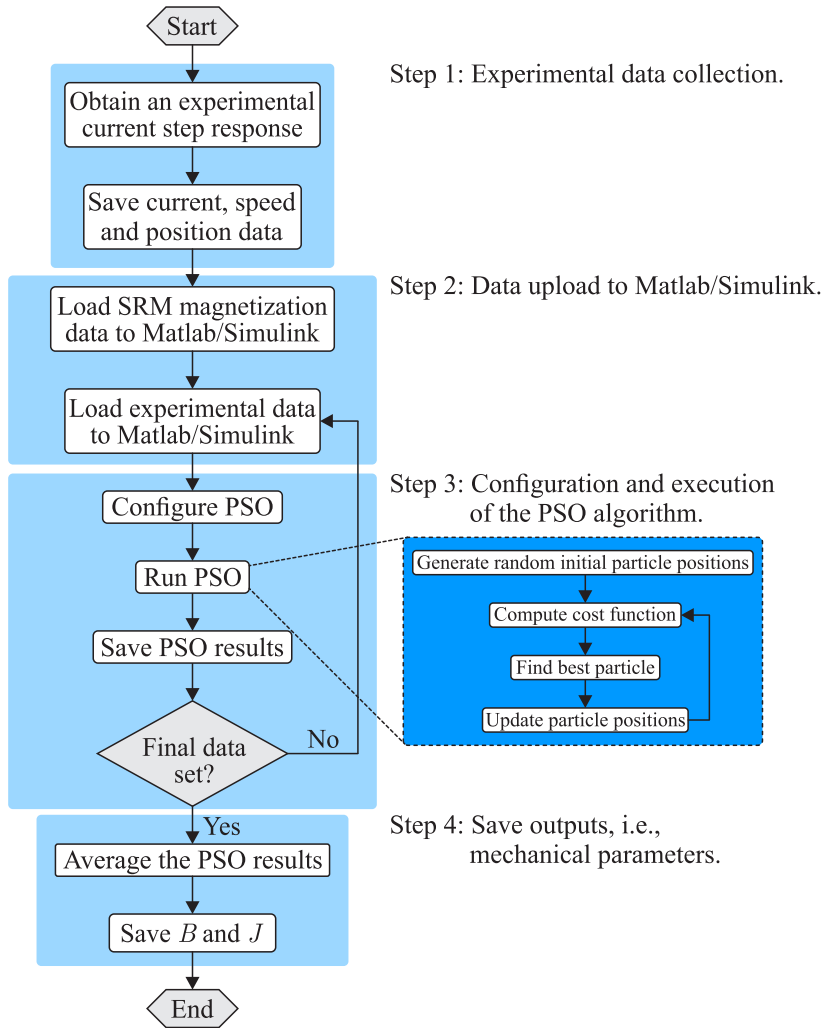
In the topic of high performance SRM drives, closed loop speed control strategies are often employed, where the mechanical parameters are considered for the controller design stage. If the values of the moment of inertia and viscous friction coefficient are significantly inaccurate, this can lead to poor control performance. Moreover, considering the difficulties associated to the estimation of the B and J parameters, in the following section a fast and effortless mechanical parameters estimation procedure for SRMs will be presented.

A.3 PSO-BASED ESTIMATION PROCEDURE

The proposed mechanical parameters estimation procedure is shown in the flowchart of Figure A.2.

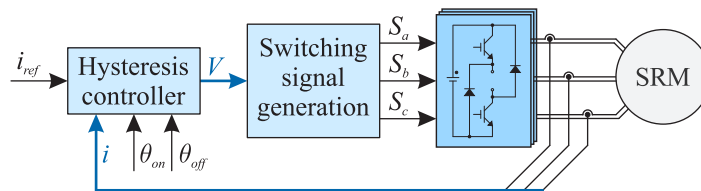
Initially, an experimental current step response is obtained, storing the speed, phase current and position waveforms. Since SRM current control is often performed using hysteresis controllers, this becomes a simple test, not requiring any prior knowledge of the machine parameters. The block diagram of the control strategy used for obtaining the measurements is presented in Figure A.3. For additional information regarding SRM simulation and control, please refer to Chapter 2.

Figure A.2 – Flowchart of the proposed estimation procedure.



Source: Author.

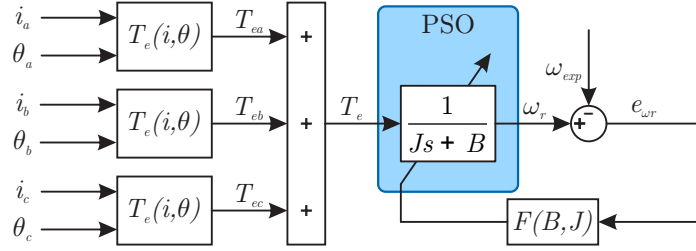
Figure A.3 – Block diagram of the current control strategy used for data acquisition.



Source: Author.

Then, the experimental data is loaded into Matlab/Simulink, along with the machine’s magnetization data, enabling the SRM simulation, as seen in Figure A.4. With the phase currents and relative positions, the electromagnetic torque can be determined using the torque lookup table, with the total torque being obtained by adding the torque produced by each phase.

Figure A.4 – Simulation of the SRM with experimental data as inputs.



Source: Author.

After that, the PSO configurations are loaded and the PSO algorithm is executed. The utilized cost function, $F(B, J)$, is given by

$$F(B, J) = \sum_1^n (\omega_{exp} - \omega_r)^2, \quad (A.1)$$

where ω_{exp} is the rotor speed measured experimentally, ω_r is the rotor speed obtained in simulation and n is the number of samples. Thus, by minimizing the sum of the quadratic error between the measured speed and the simulated speed, it is possible to estimate the mechanical parameters of the machine using the PSO algorithm.

The calculated electromagnetic torque is used to obtain the rotor speed, through the mechanical loop transfer function. The resulting parameters from the PSO algorithm, which minimize the cost function, are saved as the mechanical parameters. The procedure is repeated for the desired number of data sets. Lastly, the average of the resulting parameters is calculated, leading to the estimated mechanical moment of inertia and viscous friction coefficient. This is done as a way to avoid possible errors coming from a specific data set or from the metaheuristic nature of the PSO.

In the following section, a case study will be presented as an example, in order to illustrate the effectiveness of the proposal.

A.4 CASE STUDY

The main objective of this case study is to provide experimental validation of the estimated mechanical parameters by the proposed procedure.

The setup used to obtain the results (SRM 1) is comprised of an SRM, a three-phase asymmetric half-bridge converter and an induction machine, coupled to the SRM. The flux linkage and torque profiles of the studied SRM are presented in Chapter 2. The studied SRM is a 12/8, three-phase, 2 kW, 400 V machine. For digital control implementation, a DSP TMS320F28335 is utilized. A hard chopped hysteresis current controller was used, with a band of 100 mA and a sampling frequency of 30 kHz. The firing angles are set to

$\theta_{on} = 25^\circ$ and $\theta_{off} = 40^\circ$, where $\theta = 0^\circ$ represents the aligned position.

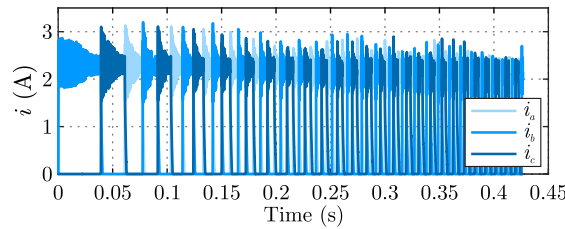
The proposed procedure was executed in Matlab/Simulink software, with the PSO configuration parameters presented in Table A.1. Figure A.5 shows an experimental data set for a 2.25 A current reference, containing phase currents, rotor speed and phase positions. Note that a fixed reference current is chosen in order to produce a positive torque value, leading to a speed increase in an unloaded SRM. The current reference is set to a large enough value so that the SRM accelerates close to base speed.

Table A.1 – Particle swarm optimization algorithm parameters.

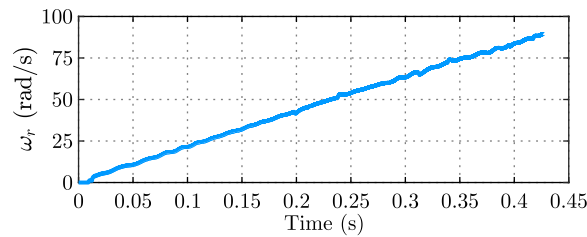
Parameter	Value
Number of particles (N)	25
Number of epochs (M)	75
Cognitive and Social coefficients (ψ_1, ψ_2)	0.5
B and J bounds	$[1 \times 10^{-5}, 0.5]$

Source: Author.

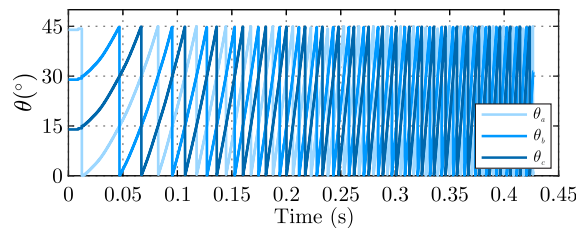
Figure A.5 – Experimental data for a 2.25 A reference. (a) Phase currents. (b) Rotor speed. (c) Phase positions.



(a)



(b)

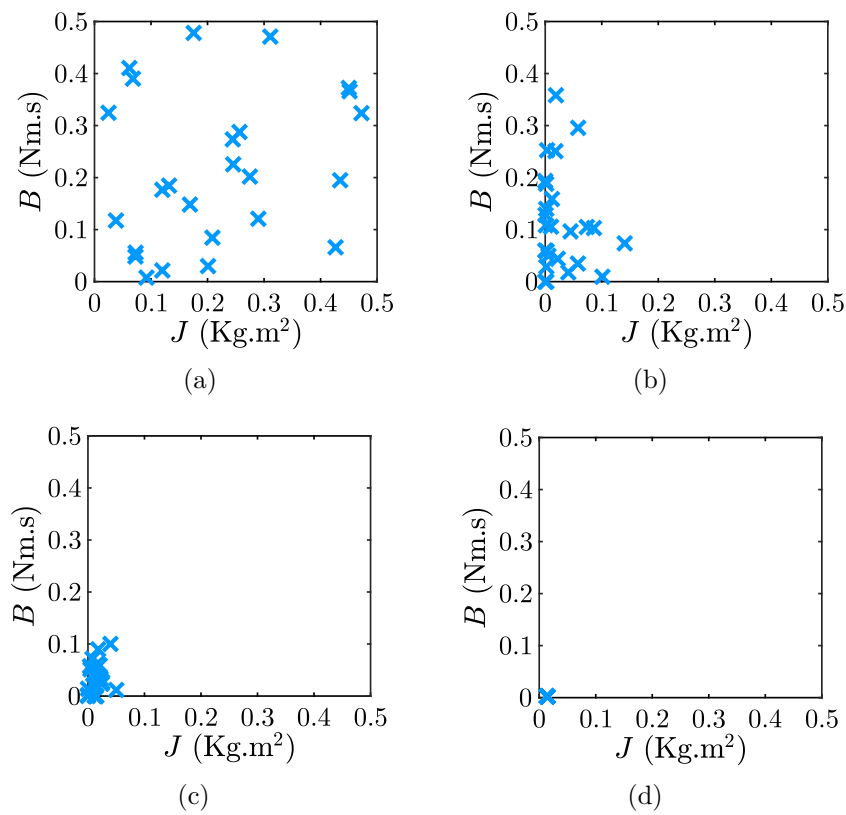


(c)

Source: Author.

Figure A.6 shows the results for the PSO algorithm throughout the epochs, for the data set presented previously. A random particle placement is observed in the first epoch. The movement and subsequent convergence of the particles within the search space can be seen, where the particles move towards values of B and J that minimize the cost function. Figure A.7 shows the fitness value for this data set, where it can be seen that the algorithm converges to the minimum value at the end of the execution, illustrating that 75 epochs are sufficient to guarantee convergence of the PSO.

Figure A.6 – Particle positions through the epochs. (a) Epoch 1. (b) Epoch 5. (c) Epoch 25. (d) Epoch 75.

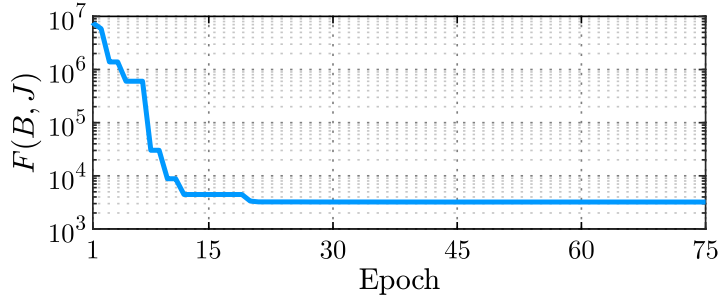


Source: Author.

The procedure is repeated for three sets of experimental data, yielding the results given in Table A.2. Then, the mechanical parameters are then calculated as the average of the values obtained in the 3 runs. The average simulation time is 1.81 minutes for each data set, showing the speed and simplicity of the procedure, with a total time of less than 6 minutes.¹

¹The parameters were computed using MATLAB/Simulink software, using a notebook with an Intel i7-8750H processor, 2.2 GHz and 8 GB of RAM.

Figure A.7 – Evolution of the best cost function value for each epoch.



Source: Author.

Table A.2 – Results for the three particle swarm optimization executions.

Data set	1	2	3
B	0.00155	0.00121	0.00375
J	0.01424	0.01483	0.01396

The values of the mechanical parameters, obtained by averaging the values presented in Table A.2, are:

$$\begin{aligned} B &= 0.002176 \text{ Nm.s/rad} \\ J &= 0.014343 \text{ Kg.m}^2 \end{aligned} \tag{A.2}$$

Due to the random nature of the PSO algorithm initialization, the obtained results may vary. Note that, however, with a sufficiently large number of particles and epochs, the convergence of the algorithm is achieved. In order to verify the dispersion of the PSO results, the procedure was performed 100 times for the same data set. From the obtained results, it is possible to calculate the coefficient of variation for the final values of the cost function and mechanical parameters according to

$$CV = \frac{\sigma}{\mu}, \tag{A.3}$$

where CV is the coefficient of variation, σ is the standard deviation and μ is the average. The results are shown in (A.4).

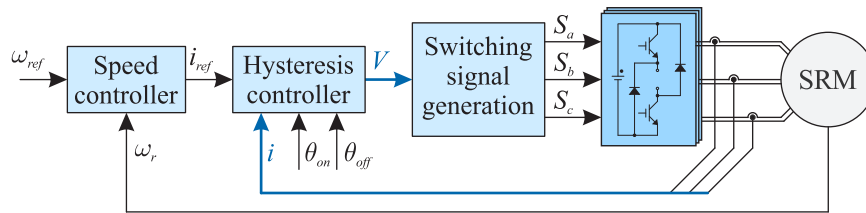
$$\begin{aligned} CV_B &= 12.11\% \\ CV_J &= 0.34\% \\ CV_{F(B,J)} &= 3.34\% \end{aligned} \tag{A.4}$$

A low dispersion is verified within the results, indicating good convergence and repeatability of the proposed procedure.

A.5 RESULTS VERIFICATION

In this section experimental results are presented in order to verify the effectiveness of the proposed procedure. The characteristics of the SRM drive as well as the control variables are the same as the ones described in Section A.4. Figure A.8 shows the block diagram of the closed-loop control structure. A speed controller designed as presented in (SCALCON et al., 2021) and making use of the parameters obtained in (A.2) is employed, while a hysteresis controller is employed in the current control loop.

Figure A.8 – Block diagram of the control strategy used in the experimental results.



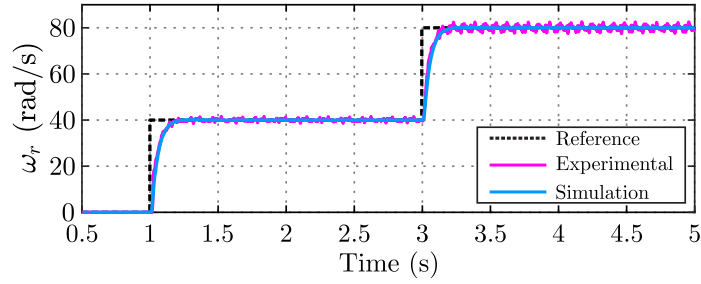
Source: Author.

A.5.1 Variable speed tests

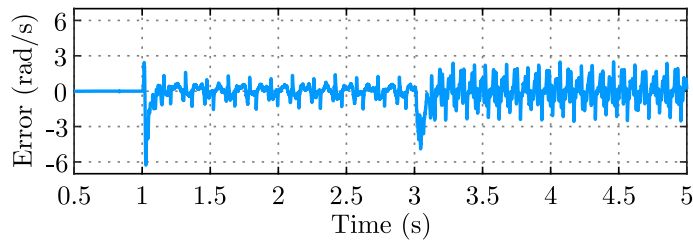
First, to evaluate the results of the PSO procedure, step variations are performed in the speed set point. At time $t = 1$ s the speed reference is increased from 0 to 40 rad/s and at time $t = 3$ s it is increased once more, to 80 rad/s. Figure A.9 (a) shows the experimental and simulation responses, from which can be verified that the estimated mechanical parameters yield simulation results with a very similar behavior to the experimental data. The relative error between the simulated and measured data is presented in Figure A.9 (b). It can be seen that virtually no error is present in the transient and steady state responses. A small error oscillation is present, however, note that is due to the noise from the experimental measurement.

Similarly, in Figure A.10 (a), two consecutive ramp variations are performed in the speed set point. Once more, good correspondence between the experimental and simulation data is observed. The relative error between the simulated and measured data, presented in Figure A.10 (b), is once more very small, attesting to the effectiveness of the estimation procedure.

Figure A.9 – Experimental results for reference speed step variations. (a) Simulation and experimental data comparison. (b) Error between simulation and experimental data.



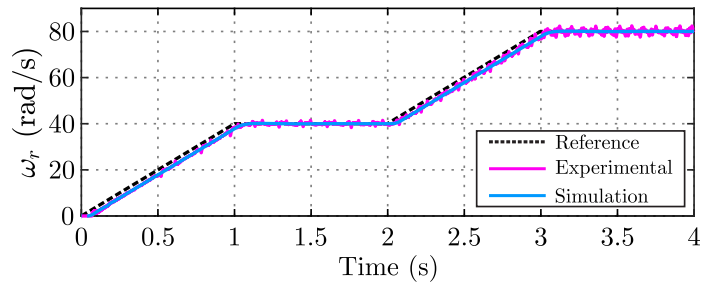
(a)



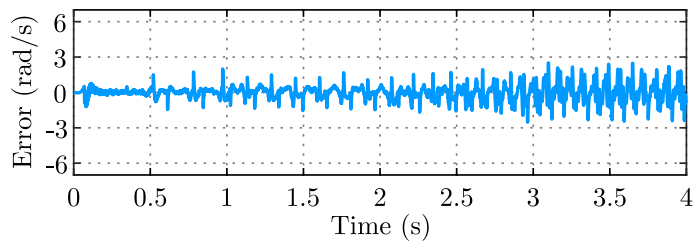
(b)

Source: Author.

Figure A.10 – Experimental results for reference speed ramp variations. (a) Simulation and experimental data comparison. (b) Error between simulation and experimental data.



(a)



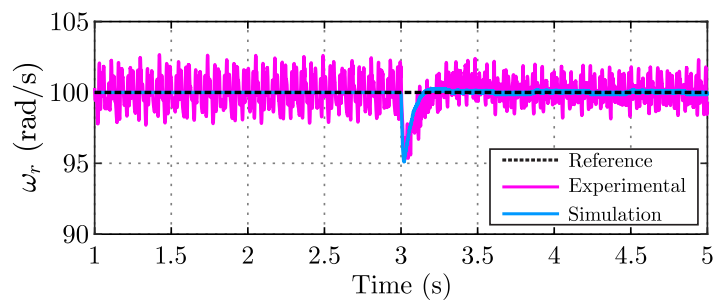
(b)

Source: Author.

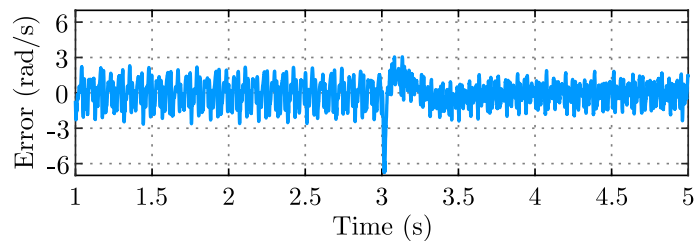
A.5.2 Variable load test

As a means to further evaluate the proposal, a dynamic load test is carried out. Figure A.11 shows the experimental and simulation responses for a load step variation. Initially, the SRM is controlled at a speed of 100 rad/s in an unloaded condition. Then, at time $t = 3$ s a mechanical load is added to the SRM. The load is imposed by means of the induction machine, operating as a self-excited induction generator, which is connected to a three-phase resistive load.

Figure A.11 – Experimental results for load step variations. (a) Simulation and experimental data comparison. (b) Error between simulation and experimental data.



(a)



(b)

Source: Author.

Similarly to the variable speed results, it can be observed that practically no error is present in the transient and steady state responses. Again, a small error oscillation is verified, however, note that is due to the noise from the experimental measurement.

A.6 CONCLUSION

This appendix provided a systematic procedure for the estimation of mechanical parameters for SRMs based on the PSO algorithm. The proposal is able to avoid cumbersome and complex tests, only requiring measurements commonly available in a SRM variable speed drive. Through a series of simulations, the PSO is able to determine the mechanical parameters that lead to the minimum squared error between simulated and measured speed data. The procedure allows a fast offline estimation of the parameters, while also circumventing the use of sophisticated observers or the need to design additional controllers, for instance. Experimental results show that the estimated parameters can be used for controller design. Moreover, experimental validation is provided, showing that the estimated parameters lead to suitable simulation responses that match the measured data. The proposed procedure is straightforward and can be adapted with minimal changes to be used for different electrical machine drives.

Appendix B – Robust speed control by means of linear matrix inequalities

In the context of high performance variable speed drives, control design is often done considering constant motor parameters, with effects such as magnetizing flux saturation being neglected. However, the control design for SRMs under these assumptions may lead to poor performance due to the presence of nonlinearities, disturbances and uncertainties. Regarding the speed control loop, the presence of disturbances and uncertainties affecting the motor also make the control design a more demanding task. Thus, appropriate models and control design, that take into account uncertain and possibly time-varying parameters, are of great importance.

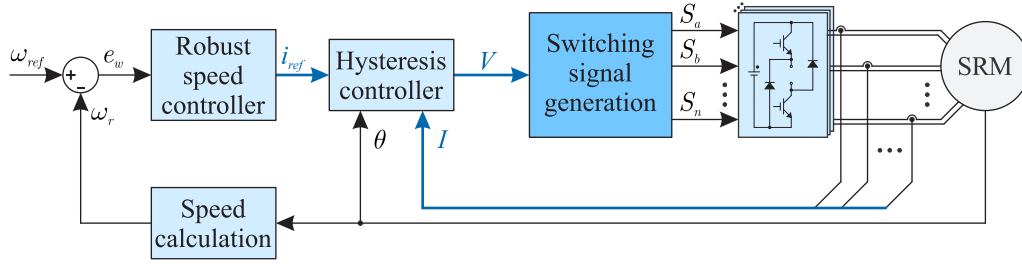
A computationally efficient tool for robust control design for systems affected by uncertain and time-varying parameters are the linear matrix inequalities (LMIs) (BOYD et al., 1994). This tool is very important in control theory and has been successfully applied in power electronics as, for instance, in (OLALLA et al., 2009; MACCARI JR. et al., 2014; KOCH et al., 2019), where one has guarantees of performance in terms of robust pole location and optimal rejection of disturbances for converters affected by uncertain parameters.

This Appendix presents a systematic robust control design procedure to cope with uncertain and time-varying parameters affecting speed control loops. The procedure is originally proposed in (SCALCON et al., 2021), where it is applied to the vector control of SynRMs. This procedure is based on a polytopic representation of SRMs that also takes into account the one step delay in the digital control implementation, not requiring complex nonlinear descriptions of the system. LMIs are then used to synthesize fixed control gains, which are rapidly computed offline and easily implemented, without relying, for instance, on lookup tables or adaptive strategies. In this context, the procedure can provide simple controllers useful for benchmarking purposes. Experimental results are provided, with suitable current and speed reference tracking, ensuring stability and performance for the entire domain of uncertain parameters.

B.1 PROBLEM DESCRIPTION

The problem to be addressed in this Appendix is the LMI-based design of robust controllers for the speed control loop, depicted in Figure B.1, in a systematic and straightforward way, leading to a set of fixed control gains capable of ensuring a prescribed performance in terms of regional pole location for each loop and also providing a theoretical certificate of stability under parametric variations and uncertainties.

Figure B.1 – Block diagram of the SRM control structure.



Source: Author.

First, the dynamic of the rotor speed presented in (2.25) can be rewritten as

$$\dot{\omega}_r = -\frac{B}{J}\omega_r + \frac{1}{J}T_m + \delta_\omega(\omega_r), \quad (\text{B.1})$$

where $\delta_\omega(\omega_r)$ represents a nonlinear term of bounded norm.

The nonlinear term $\delta_\omega(\omega_r)$ is assumed as an exogenous bounded disturbance, and the motor parameters are uncertain and can vary on time. Thus, this dynamic model can be written as a linear parameter-varying model

$$\dot{y} = a(t)y + b(t)u + c(t)\psi \quad (\text{B.2})$$

where y is the state variable, u is the control input and ψ is an exogenous disturbance.

For digital control implementation, the dynamic model is discretized, with a sufficiently small sampling period T_s , for all combinations of extreme values of the uncertain and time-varying parameters, leading to a polytopic representation with four vertices given by (see, for instance, (BOYD et al., 1994; ASTRÖM; WITTENMARK, 1997))

$$\underbrace{\begin{bmatrix} y(k+1) \\ \phi(k+1) \\ \sigma(k+1) \end{bmatrix}}_{\rho(k+1)} = \sum_{j=1}^4 \theta_j(k) \underbrace{\begin{bmatrix} \alpha_j & \beta_j & 0 \\ 0 & 0 & 0 \\ -1 & 0 & 1 \end{bmatrix}}_{A_j} \underbrace{\begin{bmatrix} y(k) \\ \phi(k) \\ \sigma(k) \end{bmatrix}}_{\rho(k)} + \underbrace{\begin{bmatrix} 0 \\ 1 \\ 0 \end{bmatrix}}_{B_u} u(k) + \underbrace{\begin{bmatrix} 0 \\ 0 \\ 1 \end{bmatrix}}_{B_r} ref(k) + \sum_{j=1}^4 \theta_j(k) \underbrace{\begin{bmatrix} \gamma_j \\ 0 \\ 0 \end{bmatrix}}_{B_{\psi_j}} \psi(k) \quad (\text{B.3})$$

with

$$\sum_{j=1}^4 \theta_j(k) = 1, \quad \theta_j(k) \geq 0, \quad j = 1, \dots, 4 \quad (\text{B.4})$$

For the speed control loop, y represents the speed ω_r , the control input u represents the mechanical torque T_m , the disturbance ψ represents the nonlinear term $\delta_\omega(\omega_r)$, and the vertices are obtained from the evaluation of matrices in (B.3) for: (B^-, J^-) , (B^-, J^+) , (B^+, J^-) and (B^+, J^+) . The superscripts $-$ and $+$ refer to the minimum and maximum values of the parameters, respectively.

The state ϕ is included to represent the digital control implementation delay and the state σ represents the integral of the tracking error.

It should be noted that, in the control theory literature, polytopic representations such as (B.3) are a recognized tool to deal with systems subject to uncertain and time-varying parameters (BOYD et al., 1994; OSÓRIO et al., 2019). The main reason for this fact is that stability analysis and control design conditions defined only for the combination of the extreme values of the parameters (called vertices of the polytope) allow to conclude about stability and performance for the entire domain of parameters.

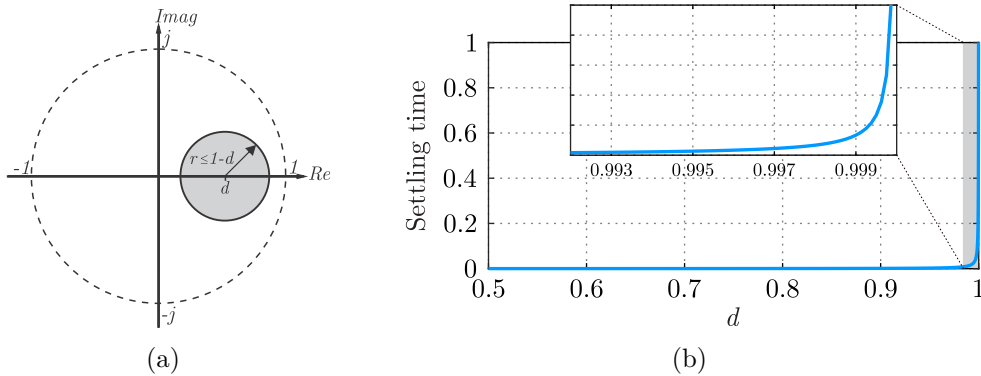
From (B.3), it is of interest the state feedback control law

$$u(k) = \mathbf{K}\boldsymbol{\rho}(k) = [K_y \ K_\phi \ K_\sigma] [y(k) \ \phi(k) \ \sigma(k)]' \quad (\text{B.5})$$

with a robust control gain vector \mathbf{K} designed for each control loop. Notice that the implementation of (B.5) does not demand additional sensors when compared, for instance, to conventional PI controllers.

Gains \mathbf{K} can be systematically designed by means of LMIs, in order to ensure a prescribed location for all closed-loop poles. For that, consider d and r as the control design parameters, defining a circular region inside the unit circle, where d is the center and r is the radius of the circle for the closed-loop poles location, as shown in Figure B.2 (a). These parameters can be related to the settling time of the closed-loop system responses. For instance, for the choice $d = 0$ and considering $T_s = 33.333 \mu\text{s}$, Figure B.2 (b) shows the relationship between r and the bound for the settling time.

Figure B.2 – (a) Circular region for pole location, inside the unit circle; (b) Relationship between parameter r and settling time, for the choice $d = 0$.



Source: Author.

It is important to point out that different circles for pole location can be chosen for each one of the control loops, based on the respective desired dynamic response. The proper choice of the parameters d and r allows, for instance, to avoid oscillatory behavior and to decouple the dynamics between the electrical and mechanical control loops, often observed in motor control applications.

Regarding the computation of the control gains by means of LMIs, in order to ensure that all closed-loop poles remain inside the unit circle, the following constraints apply: $|d| \leq 1$, $0 \leq r \leq 1$, and $|d| + r \leq 1$. Taking that into account, for given real scalars parameters d and r , if there exist symmetric positive definite matrices $\mathbf{S}_j \in \mathbb{R}^{3 \times 3}$, $j = 1, \dots, 4$ and slack matrix variables $\mathbf{G} \in \mathbb{R}^{3 \times 3}$ and $\mathbf{R} \in \mathbb{R}^{1 \times 3}$, such that

$$\begin{bmatrix} \mathbf{G} + \mathbf{G}' - \mathbf{S}_j & \mathbf{G}' \frac{A'_j - dI}{r} + \mathbf{R}' \frac{B'_u}{r} \\ \star & \mathbf{S}_l \end{bmatrix} > \mathbf{0} \quad (\text{B.6})$$

with $j = 1, \dots, 4$ and $l = 1, \dots, 4$, then the state feedback gain

$$\mathbf{K} = \mathbf{R}\mathbf{G}^{-1} \quad (\text{B.7})$$

ensures robust asymptotic stability of the system (B.3) under uncertain and time-varying parameters, bounded transient responses, and zero steady state error.

The zero steady state error is ensured for constant references due to the inclusion of the integral of the trajectory error (state σ), which can be confirmed based on the internal model principle (ASTRÖM; WITTENMARK, 1997; FRANCIS; WONHAM, 1976). The proof of the closed-loop system stability with gains (B.7) is detailed in the Appendix of (SCALCON et al., 2021), based on Lyapunov stability theory.

Remark 1: The control gains are obtained by means of the LMIs (B.6), which have multiple Lyapunov matrices (\mathbf{P}_j , $j = 1 \dots 4$) and slack matrix variables (\mathbf{R} and \mathbf{G}), which are used to recover fixed control gains. For the design, only two parameters (d and r) have to be chosen and, in order to encompass the uncertain and time-varying motor parameters, there is only the need to know their limits (i.e., the maximum and minimum values). This leads to a fast design stage, providing robust control gains that are easily implementable and able to ensure stability and performance for the entire range of parameters considered in the design.

Remark 2: The proposed design is capable to address systems with time-varying parameters, providing a theoretical certificate of stability based on a parameter-dependent Lyapunov function able to cope with arbitrary fast variations in a less conservative way than a single matrix Lyapunov function (quadratic stability).

Remark 3: It is important to note that more complex control strategies could be used, such as gain-scheduling and adaptive techniques, leading to high performance. On the other hand, based on simplified models and on less conservative LMIs, the proposed

procedure allows to obtain fixed robust state-feedback control gains in a systematic and straightforward way, leading to suitable results, as shown in the sequence.

B.2 CONTROL DESIGN EXAMPLE

The characteristics of the SRM used are presented in Chapter 2. The mechanical parameters values are shown in Table B.1. They are originally obtained in Appendix A and an interval of uncertainty is considered.

Table B.1 – SRM mechanical parameters.

Parameter	Value
Rotor inertia (J)	0.014343 kg.m $\pm 10\%$
Friction coefficient (B)	0.002176 Nm.s/rad ² $\pm 50\%$

Source: Author.

The test bench, described in Appendix C, is comprised by the SRM, a three-phase AHB converter, a DSP TMS320F28335 and an induction machine, coupled to the SRM to perform the load disturbances. The switching and sampling frequencies are set to 30 kHz.

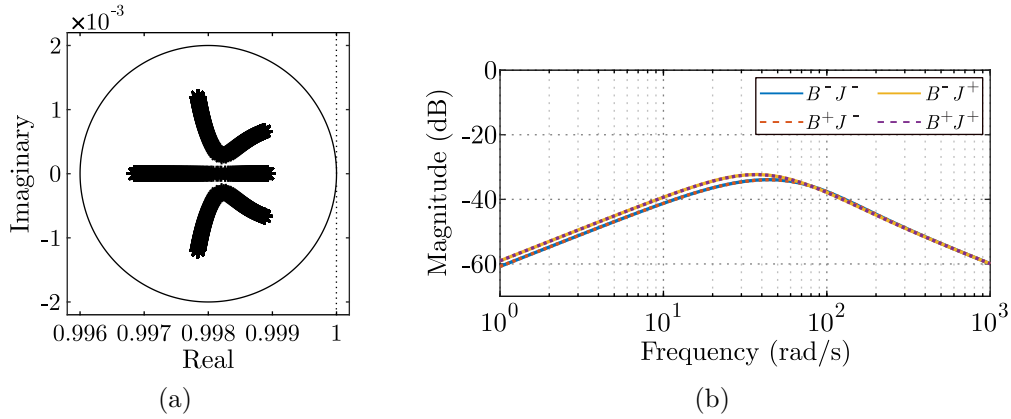
For the design of the speed controller, the control parameters are chosen as $d = 0.998$ and $r = 0.002$, in order to shift closed-loop poles to the right, avoiding oscillatory behavior and also leading to slower transient responses, as pointed in Figure B.2 (b), what allows to decouple the dynamics between the electrical and mechanical control loops. The control gains are given by¹

$$\mathbf{K}_w = [-0.004141942452047 \quad 0.994610319297382 \quad 0.000002534491732] \quad (\text{B.8})$$

After obtaining the gains, an analysis of the closed-loop poles for a sweep in the uncertain and time varying parameters is performed, confirming the pole location in the prescribed regions, and that the closed-loop system exhibits suitable dynamic responses. Moreover, a good disturbance rejection is also confirmed, indicating, for instance, that the controlled system can cope with the load variations. To demonstrate that, for example, consider the speed control loop with gains (B.8). Figure B.3(a) shows that all closed-loop poles are located inside the circle with $d = 0.998$ and $r = 0.002$, attesting the desired pole location. Figure B.3(b) shows the Bode diagrams from the input ψ to the output ω_r , attesting rejections of disturbances for the entire frequency range. Similar behaviors were verified for both current control loops, confirming suitability of the gains (B.8).

¹These gains were computed using the LMI control Toolbox from MATLAB, demanding about 0.3 seconds using a notebook with Core i7 processor, 2.5 GHz and 8 GB of RAM.

Figure B.3 – Analyses for the speed control loop with gains given in (B.8): (a) Closed-loop poles for a sweep in the parameters B and J ; (b) Bode diagrams of the closed-loop system (B.3), from the disturbance input ψ to the output ω_r .



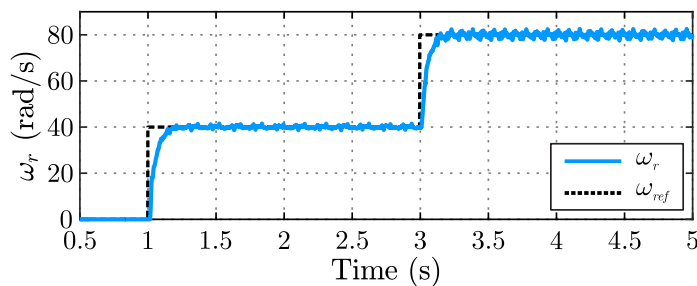
Source: Author.

B.3 EXPERIMENTAL RESULTS AND COMPARISONS

In this section, experimental tests are performed to confirm the viability of the proposed procedure.

To evaluate the performance of the speed control loop with the gains obtained based on the proposed procedure, consider the control law (B.5), with the control gains given in (B.8). For the results presented in this subsection, the current control-loop is implemented with the a hysteresis controller. The closed-loop response under sudden speed reference speed variations, in an unloaded condition, is shown in Figure B.4. It is possible to confirm that the proposed controller provides suitable transient responses, with a fast settling time. Note that the high frequency ripple is likely a result of encoder mechanical misalignment with the machine's shaft. Moreover, note that variable load results are presented in Chapter 3, attesting to the robustness of the controller.

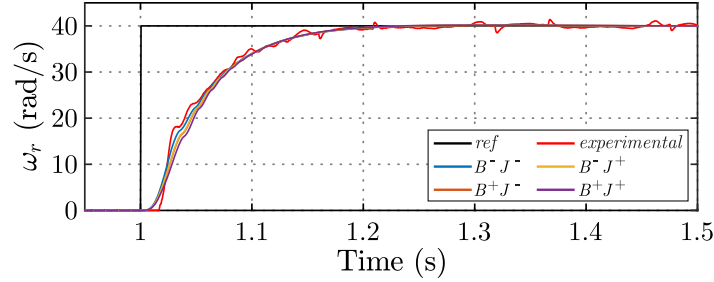
Figure B.4 – Experimental results to step reference variations with the proposed controller.



Source: Author.

Moreover, for the proposed controller, the good correspondence between the simulations using the model (B.3), for the vertices of the polytope, and the experimental result can be confirmed in Figure B.5.

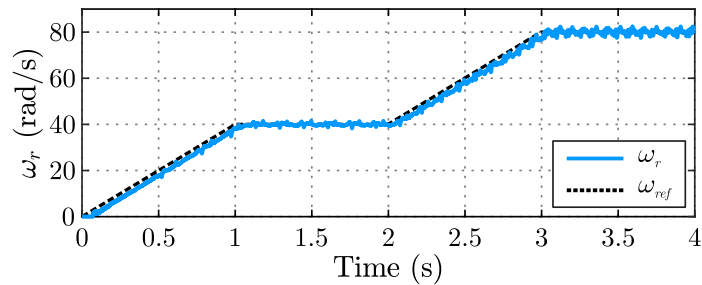
Figure B.5 – Comparison between simulation responses at the vertices and experimental result for the proposed controller.



Source: Author.

Lastly, an experimental result for a speed reference containing ramps and plateaus is presented in Figure B.6. As expected, the proposed controller ensures zero steady state error for constant references, but the tracking response for the ramp reference exhibits an error. It is important to notice that this error could be reduced by increasing the gain associated to the integral state. However, a trade-off between robustness and dynamic performance must be taken into account. Thus, since ramp references are used here only for the startup of the motor, the precise ramp tracking is not the main requirement of the closed-loop system response.

Figure B.6 – Experimental results to ramp reference variations with the proposed controller.



Source: Author.

For additional experimental results and information, such as the stability proof of the polytopic model (B.3), with control law (B.5) and gains given by (B.6)–(B.7), please refer to (SCALCON et al., 2021).

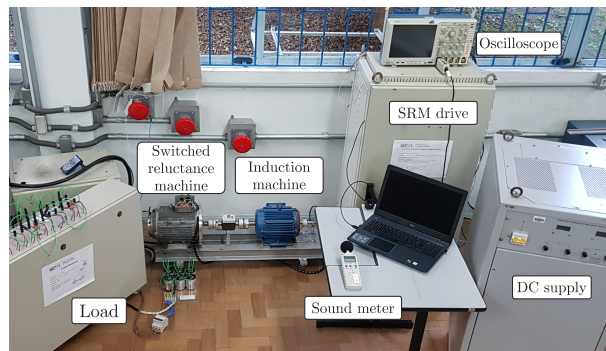
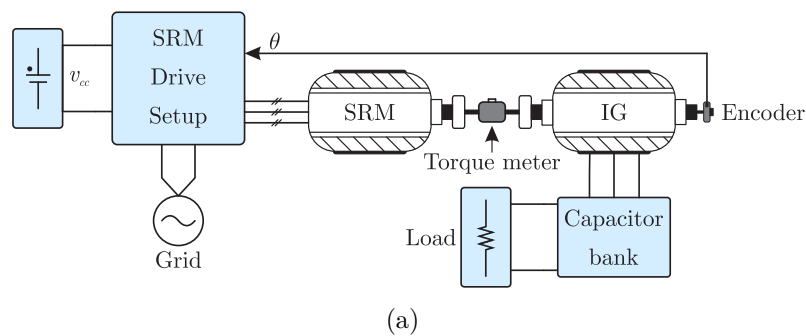
Appendix C – Experimental setup

During the development of this thesis, two experimental setups were used, referred to as SRM 1 and SRM 2. The first setup was originally developed by (OSÓRIO, 2017), and later studied by (SCALCON, 2019), being located at the Federal University of Santa Maria (UFSM). The second setup is located at McMaster Automotive Resource Centre (MARC), in Hamilton, Ontario, Canada. Each setup will be described below.

C.1 SRM 1 SETUP

Figure C.1 presents a simplified diagram and a picture of the testbench.

Figure C.1 – SRM drive setup. (a) Block diagram. (b) Picture.



Source: Author.

The setup is composed of a 12/8 switched reluctance machine, used as a motor, an induction machine, operating as a generator to provide mechanical load disturbances, and an AHB converter. A 10-bit absolute encoder is coupled to the shaft, allowing measurement of the rotor position. A torque transducer is coupled between both machines, allowing the measurement of mechanical torque. Lastly, a capacitor bank is connected to the induction machine terminals, allowing the machine to operate as a self-excited generator and to provide load disturbances.

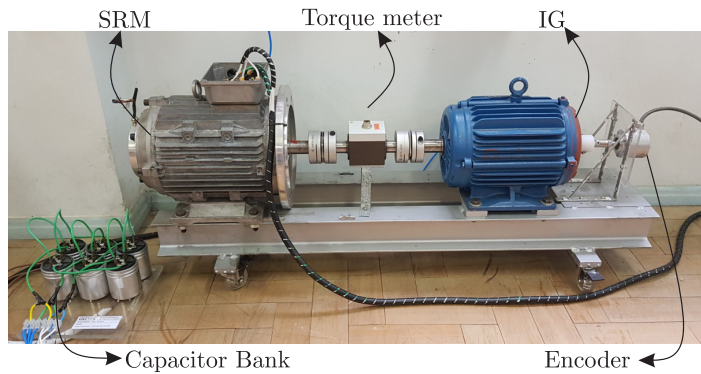
The main components present on the setup are shown in Table C.1. Figure C.2 shows the mechanical assembly of the machines, while Figure C.3 shows the control cabinet, equipped with the DSP, measuring hardware and the AHB converter.

Table C.1 – Main components of the experimental setup.

Component	Manufacturer	Specification
Switched reluctance machine	-	2 kW
Induction machine	WEG	3 CV - 4 pole - 220/380 V
Absolute encoder	Hengstler	AC58/0010AK.42SGB
Current sensors	LEM	LA 55-P
DC link capacitors	EPCOS	2x 4700 μ F, series connection

Source: Author.

Figure C.2 – Mechanical assembly of the switched reluctance and induction machines.



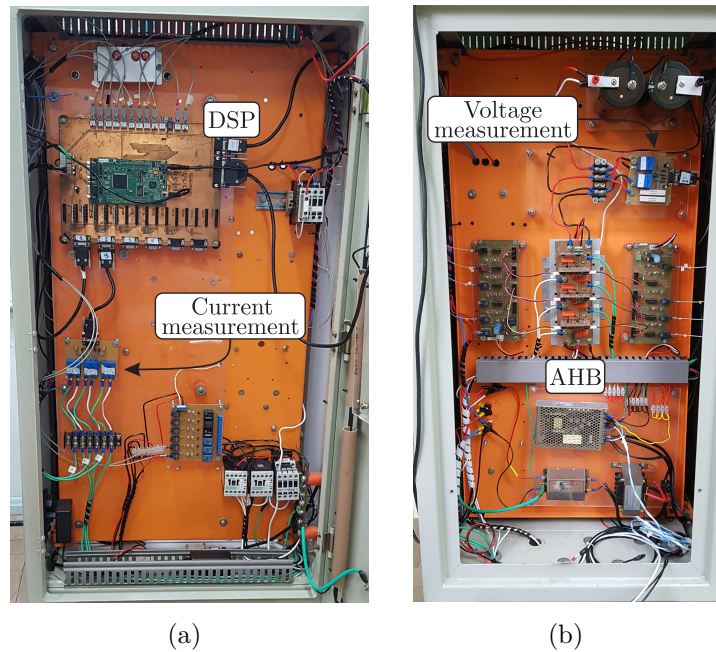
Source: Author.

C.1.1 Mechanical load and Power supply

This section describes the system used to drive the induction generator, which provides a load, and the SRM's DC power supply. Figure C.4 (a) shows the system employed to apply a load disturbance in detail, while Figure C.4 (b) shows a DC power supply, connected directly to the converter's DC link capacitors.

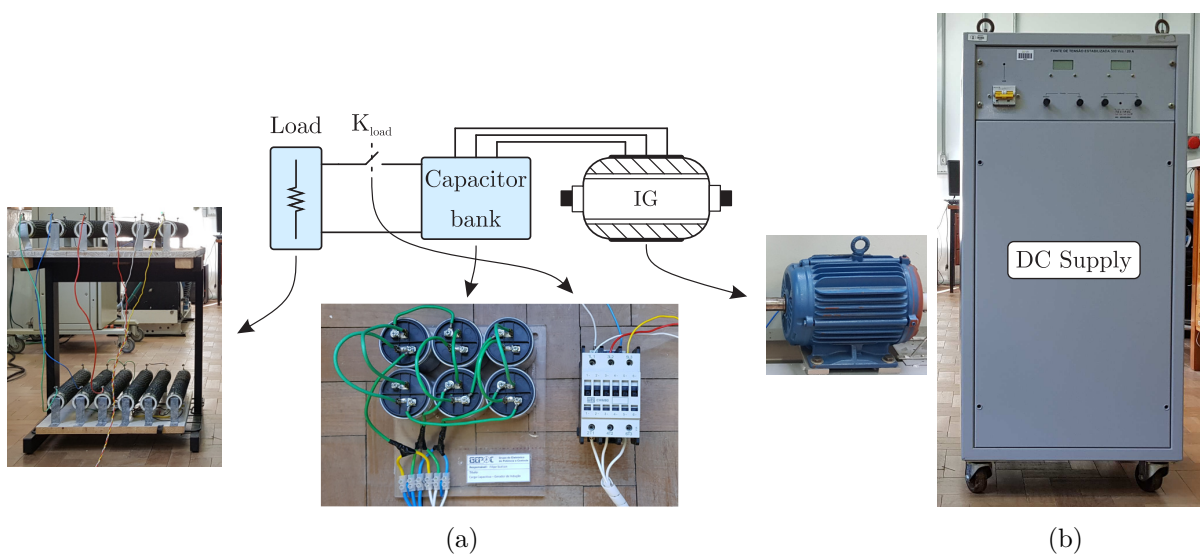
The load disturbance is applied through the use of a self-excited induction generator, which is mechanically connected to the SRM shaft. Its electrical terminals are connected to a three-phase capacitor bank, responsible for providing initial magnetization. In order to apply the load disturbance, the contactor K_{load} connects the terminals of the generator to a resistive load, composed of $9 \times 30 \Omega$ resistors, connected in series, three per phase. The individual components are listed in Table C.2.

Figure C.3 – Control cabinet with DSP, measurement hardware and AHB converter.
 (a) Front side. (b) Back side.



Source: Author.

Figure C.4 – (a) Diagram of the system used to apply the load disturbance. (b) DC power supply.



Source: Author.

Table C.2 – Individual components of the mechanical load.

Component	Manufacturer	Specification
Induction machine	WEG	3 CV - 4 pole - 220/380 V
Capacitors	EPCOS	30 μ F
Contactors	WEG	CWM80
Resistors	-	30 Ω - 100 W (each)

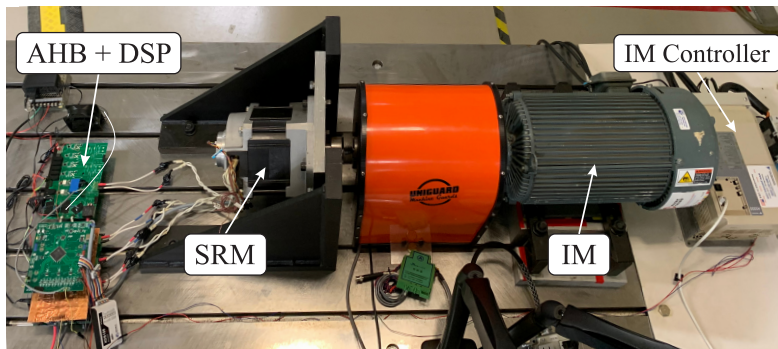
Source: Author.

C.2 SRM 2 SETUP

Figure C.1 presents a picture of the SRM 2 testbench. The setup is composed of a 8/6 switched reluctance machine, used as a motor, an induction machine, controlled by an IM drive in order to provide mechanical load disturbances, and an AHB converter. An resolver is coupled to the shaft, allowing measurement of the rotor position. A torque transducer is available, coupled between both machines.

The main components present on the setup are shown in Table C.3.

Figure C.5 – Experimental test bench encompassing the drive, the SRM and an IM, used to provide a mechanical load.



Source: Author.

Table C.3 – Main components of the experimental setup.

Component	Manufacturer	Specification
Switched reluctance machine	-	5.1 kW
Induction machine	U.S. Motors (Nidec)	15 HP - 2 pole - 230/460 V

Source: Author.